UNIVERSITY OF CALIFORNIA
RIVERSIDE

Charge and Spin Transport in Topologically Non-trivial Solid States

A Dissertation submitted in partial satisfaction
of the requirements for the degree of

Doctor of Philosophy

in

Electrical Engineering

by

Gen Yin

December 2015

Dissertation Committee:

Dr. Roger K. Lake, Chairperson
Dr. Jing Shi
Dr. Alexander Khitun

The Dissertation of Gen Yin is approved:

Committee Chairperson

University of California, Riverside

Acknowledgments

I would like to express my sincere appreciation to my advisor Prof. Roger K. Lake for the guidance, the assistance and the encourangement through my journey to the degree. I would also like to thank my lab-mates, especially Dr. K. M. Masum Habib, Dr. Darshana Wickramaratne, Dr. Yafis Barlas and Dr. Mahesh Neupane for their help in my research projects. Sincere appreciation goes to my collaborators including Prof. Jiadong Zang, Prof. Jing Shi, Dr. Xiao-ding Cai and Dr. Kwaku Eason for their important contributions to my research projects and kind guidance for my career. Special thanks to my friends for their company and support.

The text of this dissertation, in part or in full, is a reprint of the material as it appears in the following journals and/or proceedings:

- Journal of Applied Physics [1]. Reprinted with permission from [1]. © [2013] American Institute of Physics.
- Applied Physics Review [2]. Reprinted with permission from [2]. © [2014] American Institute of Physics.
- Electromagnetic Compatibility, IEEE Transactions on [3]. Reprinted with permission from [3]. © [2015] IEEE
- Physical Review B [4]. Reprinted with permission from [4]. © [2015] American Physical Society (APS).

The co-author Roger K. Lake, listed in the above publications directed and supervised the research which forms the basis for this dissertation. The remaining co-authors listed provided technical expertise and support as collaborators. This work is supported in part by FAME, one of the six centers of STARnet, a Semiconductor Research Corporation program sponsored by MARCO and DARPA, US NSF (Grant No. ECCS-1408168, ECCS-1128304 and ECCS-1124733). The micromagentic part of this work is supported by Energy

Frontier Research Center funded by the US Department of Energy, Office of Science, Basic Energy Sciences under Award No. DE-SC0012670.

To my family and friends.

ABSTRACT OF THE DISSERTATION

Charge and Spin Transport in Topologically Non-trivial Solid States

by

Gen Yin

Doctor of Philosophy, Graduate Program in Electrical Engineering
University of California, Riverside, December 2015
Dr. Roger K. Lake, Chairperson

Interfacial coupling between the top and the bottom surface states in thin-film 3-dimensional (3D) topological insulators (TIs) destroys the momentum-spin (k-s) locking chirality, and thus prohibits the good transport properties of TI surface states. Our theoretical investigations in 3D TI thin films show that this effect only occurs near the band gaps due to the spin mismatch between the opposing surfaces. By tuning the position of the Fermi level, interfacial tunneling and in-plane semi-classical transport present unique signatures due to this mismatch. These results indicate the possibility to restore the bulk transport properties of 3D TIs in the case of thin films.

As a real-space non-trivial topological order in solid states, the skyrmion phase in B20 compounds or heavy metal interfaces is considered as a strong candidate to implement next generation storage units or spintronic devices. Using coherent transport modeling, we demonstrate that a 'topological spin Hall effect' (TSHE) can be achieved in some circumstances due to individual magnetic skyrmions. In order to evaluate the device application possibilities, a topological charge analysis is carried out to identify and quantify the topological protection in each skyrmion. Based on this analysis, an on-wafer solution to individually create magnetic skyrmions is proposed. The feasibility and stability of the proposal is numerically evaluated by solving Landau-Lifshitz-Gilbert (LLG) equation.

Besides the physics that governs the operations in electronic or spintronic devices, the requirement of signal integrity gives rise to another fundamental limit to enhance the performance of next-generation devices. System designers have proposed many solutions to overcome this limit, such as differential signaling or multi-port passive networks. Characterization of these designs calls for reliable algorithms to remove the effects of access structures: the de-embedding techniques. Taking impedance mismatch as a perturbation quantity, we establish a simplified model of uniform multi-conductor transmission lines. A novel multi-port de-embedding technique is proposed theoretically and tested experimentally.

Contents

List of Figures

List of Tables

Chapter 1

Introduction

In the past decade, one of the most exciting developments in solid state physics is the recognition of topologically non-trivial phenomena. In early 1980s, the study of quantum Hall (QH) effects revealed that the exceptionally accurate integer values of QH conductivity are induced by the topological order of quantum Hall states [5]. Roughly 30 years later, physicists began to realize that spin-orbit coupling in solid states could intrinsically introduce a similar effect to the Bloch states of electron bands [6–10]. This intrinsic topological order can introduce QH states without external magnetic fields [11]. In magnetic materials where the time-reversal symmetry is broken, this leads to quantum anomalous Hall (QAH) effect [12]. In non-magnetic materials where the time-reversal symmetry is preserved, the quantum spin Hall (QSH) effect becomes possible [6, 8].

The intrinsic topological order in solid states is described by a Chern number, an integer introduced by Shiing-Shen Chern in the 1940s [13]. In a QH state, this integer counts how many times the directional solid angle of k-space Bloch states wrap a unit sphere in Hilbert space. Due to a band inversion induced by strong spin-orbit couplings, the Chern number of each type of spin can be an integer, which leads to a QSH effect [6]. The QSH state is a metallic surface state around a gapped, insulating bulk. Materials supporting these QSH states are thus referred to as 'topological insulators' (TIs) [14].

TIs are of particular interest not only in terms of fundamental physics, but also in device applications. Due to the protection of the topological order, the surface state in a TI is robust against small perturbations such as surface disorders or impurities. The structure of 3D TIs is a stack of 2D atomic layers, coupling to each other primarily through the van der Waals force [15]. This makes it possible to produce smooth surfaces with large areas, such that heterostructures with ultra-high quality is accessible. The dispersion of the surface state is a Dirac cone, in which the group velocity is roughly one percent of the speed of light [16]. The spin polarization and the momentum of a surface state are intrinsicly locked: any transport of charge automatically carries a spin current [17, 18]. These good properties have raised significant research interests to develop low dissipative electronic and spintronics devices. In Chapter 2 and 3, quantum and semi-classical carrier transport in thin-film TIs are investigated systematically.

Other than the k-space topological order observed in TIs, similar topological order also exists in real-space: magnetic skyrmions. A magnetic skyrmion is a circular, bubble-like spin texture, in which the central spin is anti-parallel to the spins outside, and the spins in between rotate smoothly from the outside to the center [19]. In spin space, this texture follows the model of a topological soliton, which was originally introduced by Tony Skyrme as a hypothetical particle in nuclear physics [20, 21]. Magnetic skyrmions are stabilized by an asymmetric exchange coupling, the Dzyaloshinskii-Moriya (DM) interaction [22]. This interaction exists when inversion symmetry is broken by the lattice structure (usually B20 compounds) [19] or interfacing with materials of strong spin-orbit couplings [23]. Competing with the symmetric Heisenberg exchange, the asymmetric DM interaction rotates the local spins away from their neighbors, leading to a helical ground state. When an external magnetic field is applied, the increase in the Zeeman coupling breaks the strips in a helical phase, leading to a collective phase change to a skyrmion lattice, in which the bubble-like skyrmions form a 2-dimensional dense packing lattice [24].

The topological order in a magnetic skyrmion can also be described by Chern number. The manifold of the real-space spin is homotopy equivalent to a unit sphere

in spin space, which introduces a topological charge of 1 or -1 to each skyrmion. Due to this topological order, when spin polarized carriers pass through the texture, they capture a Berry phase, which can be considerred as an emergent magnetic field of a flux quantum. This leads to a topological Hall (TH) effect [25], which has been experimentally demonstrated in many materials [26–31]. The topological order also protects the texture from pinning impurities, making skyrmions several orders of magnitudes more mobile than topologically trivial magnetic textures [32,33]. The topological charge provides extra stability to the spin texture, making it possible to implement skyrmion data bits of several nanometers [34]. Due to these good properties, the technology to precisely and effectively manipulate each individual skyrmion has become a hot research topic in spintronics, which is the focus of Chapter 4 and 5 in this dissertation.

The difficulty to enhance device performances in the framework of current technology is not only induced by the device physics that fundamentally governs the operation mechanisms, but also lies in the operation frequency. Although modern developments in solid state physics, especially the discovery of the non-trivial topological order, have provided many strong candidates for device applications beyond Moore's law, another issue, signal integrity, fundamentally limits the performance of electronic devices at the system level [35]. In high-speed systems, signals beyond 10 GHz radiate electromagnetic waves to the environment, which can cause severe cross-talk and amplitude loss issues [36]. Many techniques have been developed to enhance the RF performance for high-speed systems such as differential signaling and multi-conductor transceiver solutions [37]. In these developments, accurate experimental characterization of multi-port system is important. The effects of access structures such as vias or contact pads should be removed, or de-embedded, from the measurement results [38,39]. Although the procedure to achieve this is rather standard in two-port device measurements, the on-wafer de-embedding technique for multi-port devices is not [40, 41]. In Chapter 6, a new way to de-embed passive multi-port devices is introduced. This method is established based on an impedance perturbation theory of multi-conductor transmission lines.

Chapter 2

Tunneling spectroscopy of chiral states in ultra-thin topological insulators

2.1 Introduction

Topological insulators (TIs) constitute a new class of quantum materials with bulk insulating band gaps and gap-less Dirac-cone edge or surface states. The surface states are protected against time-reversal-invariant perturbations such as non-magnetic impurities, defects, and reconstruction [8, 9]. Unlike the regular quantum Hall effect, electrons in a TI form topologically protected helical surface states due to the effective magnetic field generated by strong spin-orbit coupling, rather than external magnetic fields [6]. The unique spin environment in this material introduces the possibility of observing exotic quasi-particles such as magnetic monopoles [17,42] and Majorana fermions [43,44]. In a low-energy surface state, each momentum state, $\mathbf{k}$, is uniquely coupled to a spin, $\mathbf{s}$. Thus, charge transport along the surface yields a polarized spin current, i.e. states with opposite spin counter-propagate at a given surface. This has led to an interest in spintronic applications

of surface transport in TIs [17,18,45,46]. Recent angle-resolved photoemission spectroscopy (ARPES), scanning tunneling spectroscopy (STS) and theoretical studies indicate that the surface states of the three dimensional (3D) TIs such as Bi_2Se_3 , Bi_2Te_3 and Sb_2Te_3 exhibit a single Dirac cone dispersion [16, 47–51].

One of the challenges to observe the surface transport in the topologically protected states is to reduce the bulk contribution to the total conductivity. This has been demonstrated through the use of complex materials [52, 53] or surface/bulk doping [53–55]. An effective method to increase the surface contribution is to synthesize TI thin films [56–58] or nanoribbons [59] that have a greater surface-to-volume ratio. Recent experimental transport studies successfully demonstrate a significant contribution of the surface conductivity on 3D TI thin films [60, 61].

Surface states of 3D TIs have been demonstrated to have a depth of $\sim 3\,\mathrm{nm}$ [15,62]. As a result, hybridization of the surface states occurs when the film thickness is on the order of ~ 6 nm. For such thin films, surface carriers can tunnel through the bulk bandgap to the opposite surface of the thin film [63, 64]. However, the top and the bottom surface states of a TI have opposite **k**-**s** chiralities, which severely restricts the inter-surface tunneling probability. The tunneling is governed by the usual rules of energy, momentum, and spin conservation. As a result, the surface-to-surface tunneling can only be between states at the same energy ϵ with the same momentum $\mathbf{k}$ and spin $\mathbf{s}$. These selection rules combined with the momentum-spin locking of opposite chiralities on opposite surfaces give rise to unique temperature and Fermi-level dependencies of the tunneling conductivity and a unique tunneling-current response to a bias applied between the two surfaces. Thus, tunneling spectroscopy provides several unique signatures of the opposite chiralities of opposing surface states of topological insulators. In this chapter, we theoretically demonstrate and analyse the above dependencies.

2.2 Method and Calculation Details

To observe tunneling between opposite surface states, the surface states should not be perturbed in the vicinity of the tunneling region. One way to accomplish this is to physically separate the contact regions from the tunneling region as shown schematically in Fig. 2.1a. Electrons injected into a mixture of bulk and surface states in the vicinity of the contacts will adiabatically decay into a surface state in the vicinity of the tunneling region. In practice, the films of topological insulators are terraced with thicker and thinner regions [65]. The actual placement and geometry of the contacts may vary and depend on the particular film. The structure shown in Fig. 2.1a could have mirror symmetry with injection from both the left and the right, or it could have a wrap-around top contact or a wrap-around tunneling region as shown in Fig. 1b. The back-side contact could also be physically removed from the tunneling region, not necessarily underneath the top contact, or the back contact could be the entire bottom surface of the film that is weakly coupled to the vacuum chuck of the probe station. The large area could compensate for the low specific contact resistivity. The calculations of transmission and current in this chapter assume a symmetric structure such as Fig. 2.1a with mirror symmetry or Fig. 2.1b such that the tunneling transmission of a $|\mathbf{k}\rangle$ state is independent of the angle.

Surface states propagate across both the surfaces and the edges of a topological insulator slab which leads to two current channels, (a) inter-surface tunneling and (b) surface current flowing across the perpendicular edges. To observe the inter-surface tunneling current, channel (b) should be removed by gapping the surface state away form the contact and tunneling region. This can be achieved by magnetic doping that breaks the local time reversal symmetry [66]. A single magnetic impurity opens a local band gap up to ~ 60 meV within a range of ~ 8 nm around the impurity. This local band gap suppresses channel (b), allowing the tunneling current of channel (a) to be observed.

To analyze the surface-to-surface tunneling, we focus on the dynamics governing the inter-surface tunneling that are independent of the particular arrangement of the con-

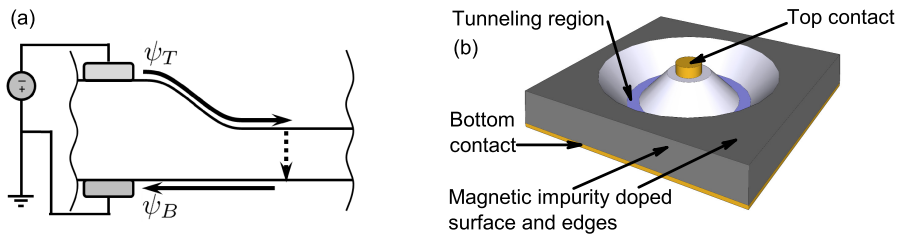

Figure 2.1:
(Color online) (a) Schematic illustrating the separation of the top contact and the tunneling region to avoid perturbing the surface state in the tunneling region. The structure in (a) could have mirror symmetry or it could have a wrap-around contact or a wrap-around tunnel region as shown in (b). (b) Symmetric implementation of (a) with a wrap-around tunnel region. Magnetic doping of the surface and edges prevents leakage around the edges from the top surface to the bottom surface. The bottom contact could be the vacuum chuck of the probe station. The high specific contact resistance of the weakly coupled back-side contact could be compensated by its large area.

tacts. The 4×4 $k \cdot p$ Hamiltonian for 3D TIs [16] serves as the starting point for the model. To include the effects of finite thickness and a spatially dependent potential drop between the top and bottom surfaces, the $k \cdot p$ Hamiltonian is discretized along the z-axis with a grid spacing of 3Å using a finite difference technique [67]. A potential difference between the two surfaces is modeled by adding an extra term, $U(z_i)$, to the diagonal elements of the discretized Hamiltonian where z_i indicates the points of the discretization grid.

Fig. 2.2a and the white lines in Fig. 2.2c show the band structure resulting from the discretized $k \cdot p$ Hamiltonian for a 6 nm thin film at equal potential. A Dirac cone is formed at Γ, representing the dispersion of the degenerate top and bottom surface states. The bulk states have a band gap of ~ 0.4 eV, and they split into several sub-bands due to quantum confinement. The inter-surface coupling opens a band gap of ~ 3.5 meV at the tip of the Dirac cones. A linear potential drop between the two surfaces generates a Rashba-like splitting in the band structure (Fig. 2.2b and Fig. 2.2d), which is consistent with recent simulation results and ARPES experiments [45, 54, 56].

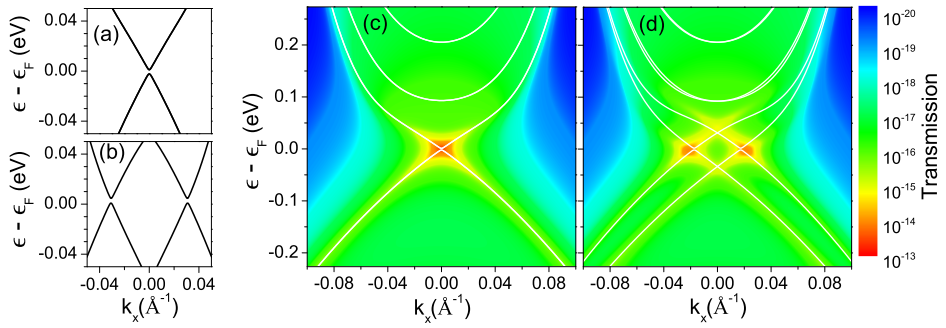

Figure 2.2:
(Color online) Dispersion of a 6 nm TI thin film and the corresponding inter-surface transmission spectrum plotted on a logarithmic scale. (a) Dispersion close to the Dirac point when the surfaces are at equal potential ($U = 0$) such that the top and bottom Dirac cones align. (b) Dispersion close to the Dirac point with an inter-surface potential difference of $U = 80$ meV giving an effective Rashba-like splitting. For both cases, a small 3.5 meV band gap is opened due to the surface-surface coupling. (c) Transmission spectrum for the equal-potential case. The white lines indicate the corresponding band structure. (d) Transmission spectrum and the corresponding Rashba-like split dispersion when $U = 80$ meV

The surface-surface tunneling is modeled with a NEGF approach [68]. A symmetric bias V_a is applied to the top and the bottom electrodes, and it drops linearly through the bulk. The bias V_a splits the top (T) and the bottom (B) electrochemical potentials such that $\mu_{T,B} = \epsilon_F \pm \frac{eV_a}{2}$, where ϵ_F is the Fermi level at equilibrium. There can also exist a built-in potential U_{bi} due to different environments of the top and bottom surfaces. Thus, the total surface-surface potential difference is $U = U_{bi} - qV_a$. Carrier injection from surface eigenstates is modeled with self-energy terms obtained from two semi-infinite surface Green's functions. The self-energies provide a finite lifetime of $\tau = 0.2$ ps that gives an energy broadening of 3.0 meV. This broadening is equal to the energy splitting of the top and bottom surface states resulting from the finite coupling through the bulk. Details of the model and numerical implementation are provided in the appendices.

2.3 Results and Discussions

2.3.1 Tunneling Selection Rule

The transmission coefficient $T(\epsilon, \mathbf{k})$ describes the probability of an electron in state $|\mathbf{k}\rangle$ on the top surface tunneling to state $|\mathbf{k}\rangle$ on the bottom surface. In the absence of a finite lifetime, the tunneling of state $|\mathbf{k}\rangle$ would occur at a discrete energy ϵ. In the presence of a finite lifetime, the tunneling of a state $|\mathbf{k}\rangle$ occurs over a range of energies Γ_0 corresponding to the energy broadening.

A logarithmic plot of the transmission of a 6 nm slab at $k_y = 0$ is illustrated in Fig. 2.2c and Fig. 2.2d for two different cases of applied bias. Fig. 2.2c shows the transmission when the slab is at equal potential ($U = 0$) such that the Dirac cones of the top and bottom surfaces are aligned. The maximum transmission in Fig. 2.2c occurs at Γ, while the transmission along the other points on the dispersion are significantly suppressed by a factor of $\sim 10^3$ to $\sim 10^4$. We will see that the total, integrated, surface-surface tunneling when the bands are perfectly aligned is a minimum rather than a maximum. Fig. 2.2d shows the transmission with a potential difference of $U = 80$ meV, which creates a Rashba-like splitting. The Rashba-like splitting results in maximum transmission at the intersection of the two Dirac cones. The maximum transmission coefficient is larger than the other points along the dispersion by a factor of $\sim 10^3$.

The suppression of the transmission away from Γ in Fig. 2.2c originates from the opposite spin-momentum locking of the top and bottom surfaces. 3D TI thin films have 180° rotational symmetry, so the spin-momentum locked chiralities of the top and the bottom surfaces are opposite to each other. For a given $\mathbf{k}$ at the same energy, the two opposite surface states have opposite spins. For the equal-potential condition when the potential is uniform across the slab, the dispersion of the top (Fig. 2.3a) and the bottom (Fig. 2.3b) surfaces align perfectly with each other (Fig. 2.3c). Therefore, energy and momentum can be conserved in a tunneling event for every state of the top and bottom surfaces. However,

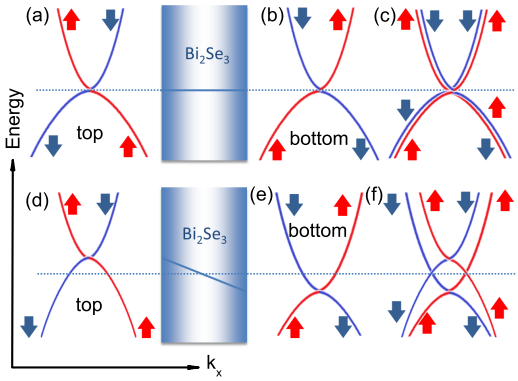

Figure 2.3:
(Color online) Schematic of band alignments illustrating the quantum number selection rules. The blue bands with the down arrows indicate negative spin states, while the red bands with the up arrows correspond to positive spin states. The gray region in between represents the bulk material. (a) and (b) illustrate the alignment of the surface Dirac cones when the two surfaces are at the same potential, $U = 0$. (c) Overlay of the top and bottom surface bands when $U = 0$. The cones are slightly offset to demonstrate the mismatch of spin for each $\mathbf{k}$ and ϵ except at $\mathbf{k} = 0$. Energy, momentum, and spin can only be conserved at $\mathbf{k} = 0$. (d) and (e) show the shifted top and bottom surface states when the surface-surface potential is nonzero. (f) Overlay of (d) and (e) in which the intersection of the Dirac cones is indicated by the dashed line. The intersection of the two Dirac cones forms a circle in the $k_x - k_y$ plane. Energy, momentum, and spin are only conserved on this circle. The small bandgap of a few meV resulting from the intersurface coupling is not shown.

the spin for each ϵ, $\mathbf{k}$ state of the top surface is antiparallel to the spin of the same state on the bottom surface. Energy, momentum, and spin can only be conserved at Γ. Thus, when the two surfaces are at equal potential, the antiparallel spins resulting from the opposite chiralities of the top and bottom surfaces suppress tunneling except at Γ.

When a potential difference exists across the slab, the top and bottom surface bands are offset from each other as shown in Fig. 2.3d and Fig. 2.3e. The hole dispersion of the top surface intersects with the electron dispersion of the bottom surface. The intersection between the two dispersions moves away from Γ, as illustrated in Fig. 2.3f. Thus, the transmission spectrum in Fig. 2.2d shows two bright spots corresponding to the points of intersection. In the k_x-k_y plane, the band intersection forms a circle. At every point on the circle, the spins of the top (hole) and bottom (electron) states align. At these points of intersection, the bands from the top and bottom surfaces couple and split resulting in a small gap in the spectrum. The circle of intersection is then split into two circles at the top and bottom edges of the small band gap. For thinner films, this spitting causes the energy splitting of the transmission peaks seen in Fig. 2.4.

2.3.2 Tunneling Transmission Spectrum

The conservation rules governing the inter-surface tunneling result in a total integrated transmission spectrum $T(\epsilon)$ that is energy selective. To understand the behavior of the tunneling current, we calculate $T(\epsilon)$ by integrating $T(\epsilon, \mathbf{k})$ over the 2D Brillouin zone. Fig. 2.4a shows the plot of $T(\epsilon)$ at the equal potential condition ($U = 0$) for different film thicknesses. The reference energy is chosen at the surface valence band edge, ϵ_V, of the 6.0 nm thin film. The peaks in $T(\epsilon)$ illustrated in Fig. 2.4a are due to the matching $\mathbf{k}$ and $\mathbf{s}$ which occur only at the band edges. The peak-to-peak distance is the surface band gap opened by the inter-surface coupling. Since the band gap decreases with a decrease of the coupling, the two peaks in $T(\epsilon)$ move towards each other as the film thickness increases.

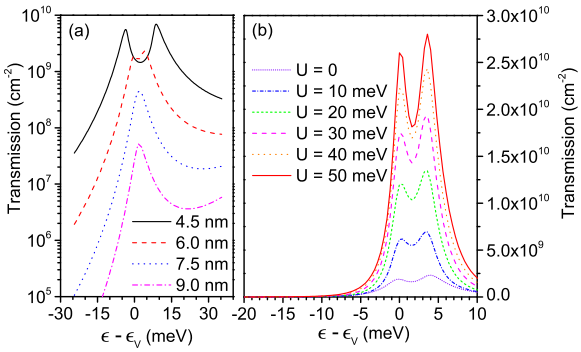

Figure 2.4:
Total, integrated transmission spectrum $T(\epsilon)$. (a) Thickness dependence of $T(\epsilon)$ on a logarithmic scale in the absence of bias ($U = 0$). The energy reference is set at the band edge (ϵ_V) of the 6.0 nm thin film. (b) The effect of bias on the transmission of the 6.0 nm film. The potential of the top surface is raised by $U/2$ and the potential of the bottom surface is lowered by $U/2$.

Due to the broadening caused by the self-energy terms, the two transmission peaks merge together for the two thicknesses greater than 6.0 nm.

In the Rashba-like split case, the peak height of the total transmission spectrum is determined by surface-surface potential difference U. Fig. 2.4b shows the transmission change in response to the surface-surface potential for the 6.0 nm thin film. In this plot, a modification in U from 0 to 50 meV increases the transmission peak height by a factor of ~ 10. As discussed above, the tunneling conservation rules generate transmission maxima at the band edges of the intersecting Dirac cones. The circumference of the intersecting circles formed at the band edges determine the transmission peak height in the integration over $\mathbf{k}$. An increase in U enlarges the circumference of the intersecting circles, which leads to the increase in the transmission peak height. According to Fig. 2.2b, although the surface-surface coupling opens a finite band gap, the low-energy dispersion of the Dirac cones away from the band edges is not significantly altered. Thus, for small U, the circumference of the intersecting circle increases almost linearly with an increase in U, which explains the linear-like relation between the peak height in $T(\epsilon)$ and the potential difference U.

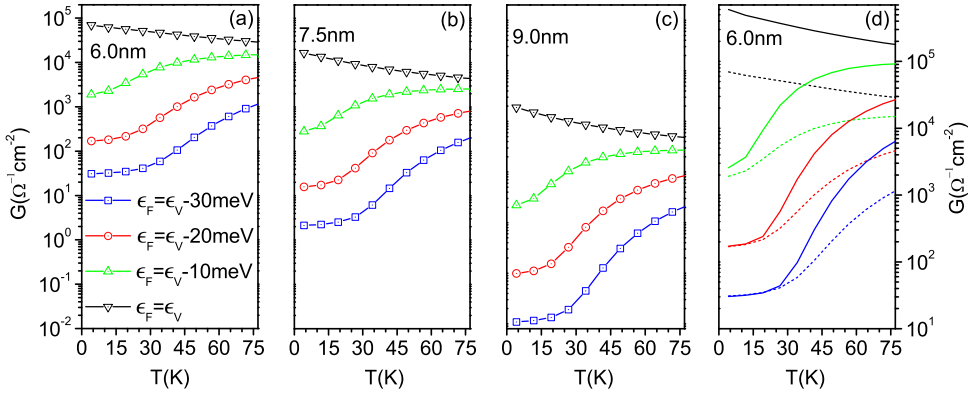

Figure 2.5:
(Color online) Temperature response from 1.8 K to 77 K of the tunneling conductance for different alignments of ϵ_F as shown in the legend of (a) for three film thicknesses of (a) 6.0 nm, (b) 7.5 nm, and (c) 9.0 nm. (d) The effect of a surface-surface potential difference of $U = 30$ meV on the temperature dependence of the tunneling conductance is compared with the $U = 0$ case for the 6.0 nm film. The dotted curves are the same as in (a) with $U = 0$. The solid curves are with $U = 30$ meV.

2.3.3 Temperature and Fermi-Level Dependence of the Tunneling Conductance

Since the surface-surface tunneling transmission spectrum is strongly peaked in energy due to the selection rules, the tunneling conductance G can be significantly modified by the position of the Fermi level and the temperature. First, the equal potential case is considered. Figs. 2.5a-c illustrate the thermal response of the tunneling conductance for different positions of the Fermi level, ϵ_F, for three different film thicknesses.

At low temperature, a 30 meV downward shift of ϵ_F from ϵ_V into the valence band moves the thermal window away from the transmission peaks. Thus, the tunneling conductance is reduced by $\sim 10^4$ due to this ϵ_F modification. When ϵ_F is away from ϵ_V, an increase in temperature populates more states around ϵ_F to contribute to the total conductance. As the thermal broadening starts to include the peaks in the transmission spectrum, a considerable conductance increase occurs. As a result, as demonstrated in Fig.

2.5, a larger shift of ϵ_F requires higher temperature to turn 'on' this conductance increase. Overall, when the Fermi level is away from the band edge, the temperature dependence of the tunneling conductance is positive. On the other hand, when the Fermi level is at the band edge, $\epsilon_F = \epsilon_V$, the transmission peak is always at the center of the thermal broadening. Thus, a higher temperature broadens the Fermi function occupying more states away from the band edges that are not allowed to tunnel and reducing the occupation of states at the band edges that are allowed to tunnel. Thus, the temperature dependence of the tunneling conductance is negative. As a result, for a TI thin film, scanning ϵ_F through the Dirac point flips the sign of the temperature dependence of the tunneling conductance. Modifying the thickness of the thin film simply reduces the magnitude of the tunneling conductance, leaving the trends of the temperature and Fermi-level dependencies unchanged. This unique thermal/Fermi-level response is a signature of the chiralities of the topological surface states and the rotational symmetry of the thin film.

The unique trends of the thermal response of the tunneling conductance are not significantly affected by a Rashba-like splitting generated by a non-zero surface-surface potential difference U. Fig. 2.5d compares the thermal response for the two cases of $U = 0$ and $U = 30\,\text{meV}$ in a $6.0\,\text{nm}$ TI thin film. As shown in Fig. 2.4b, an increase in U enlarges the intersecting circles of the top and bottom Dirac cones, leading to an increase in the transmission peaks. Thus, the tunneling conductance is increased by the increase in U when the transmission peaks start to be included in the thermal window. As a result, in the case of $\epsilon_F \neq \epsilon_V$, the increase in U leads to a faster increase in conductance with temperature as illustrated in Fig. 2.5d. When $\epsilon_F = \epsilon_V$, the transmission peaks are always included in the thermal window. Thus, the increase in conductance resulting from $U = 30\,\text{meV}$ appears as a vertical shift of the $U = 0$ thermal response curve. Comparing the solid lines and the dashed lines in Fig. 2.5d, although the Rashba-like splitting modifies the absolute value of the tunneling conductance, the unique trend of the thermal response does not change with the increase in U. Hence the trends in the temperature and Fermi-level dependencies of the tunneling are robust to asymmetries in the surface-surface potential.

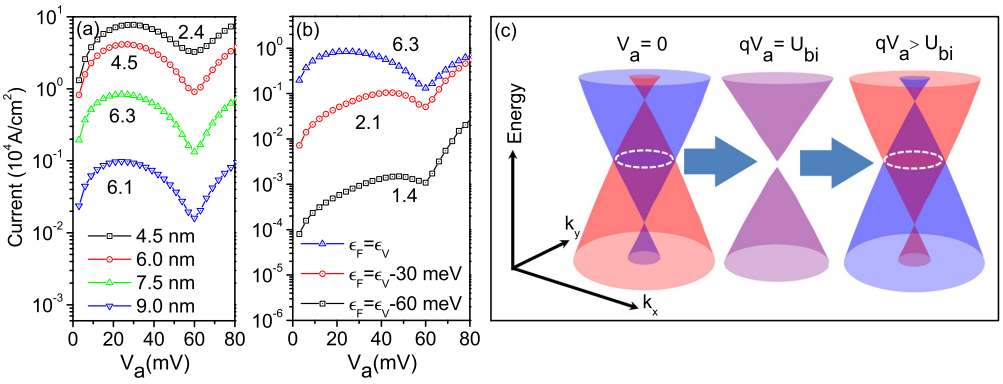

Figure 2.6:
(Color online) Current voltage response of the tunneling current at 77 K with a built-in, inter-surface potential difference of $U_{bi} = 60$ meV. The number beside each I-V curve indicates the peak-to-valley current ratio. (a) Current-voltage response when the equilibrium Fermi level is aligned at the valence band edge, $\epsilon_F = \epsilon_V$, for 4 different film thicknesses as shown in the legend. (b) Current-voltage response of the 6.0 nm thin film for three different alignments of the equilibrium Fermi levels, ϵ_F, as shown in the legend. (c) An illustration of the Dirac cone alignments for three different biases: $V_a = 0$, $qV_a = U_{bi}$, and $qV_a > U_{bi}$. The top Dirac cone is denoted by the red color, while the bottom one is denoted by blue.

2.3.4 Nonlinear Current Response

The tunneling-current response to a finite bias applied between the two surfaces also shows unique signatures of the chiral nature of the two surface states. When a built-in potential difference exists between the two surfaces such that one surface is n-type and the other one is p-type, the slab can then be viewed as a p-n heterojunction with a tunneling barrier in between the p and the n regions. Aligning the Fermi level at the valence band edge, $\epsilon_F = \epsilon_V$, a forward bias V_a results in a tunneling current. Fig. 2.6a illustrates the current-voltage (I-V) response for different film thicknesses when $U_{bi} = 60$ meV.

With an increase in the applied bias, the absolute value of the surface-surface potential difference is first reduced from U_{bi} to zero, and then starts to increase. During this process, there are two factors that determine the total current: (a) the opening of the bias window between the top and bottom surface Fermi levels, $\Delta\epsilon_F = qV_a$, and (b) the change

in the transmission peak height. At small bias, the increase in V_a reduces U, which almost linearly reduces the transmission peak height as shown in Fig. 2.4b. Initially, the current response is dominated by $\Delta\epsilon_F = qV_a$, so that the current turns 'on' and increases as the applied bias increases up to about 30 mV. After that point the decreasing transmission driven by the applied bias dominates the current response, the current decreases, and negative differential resistance (NDR) is observed. When $qV_a = U_{bi}$ so that the top and bottom surface states are at the same potential, the tunneling current reaches a minimum due to the anti-parallel spins of the top and bottom surface Dirac cones. From this minimum state, a further increase in V_a increases the absolute surface-surface potential difference which increases the transmission peak height and increases the current. Fig. 2.6c illustrates the Dirac cone alignment at $V_a = 0$, $qV_a = U_{bi}$, and $qV_a > U_{bi}$. The intersecting circle that occurs at the valence band edge is denoted by the white dashed line.

The peak-to-valley current ratio (PVCR) varies with the thickness of the thin film. The numbers underneath each current peak in Fig. 2.6a give the value of the PVCR for that film thicknes. At 77 K, the largest PVCR of 6.3 occurs in the 7.5 nm film. As the film thickness decreases, below 7.5 nm, the minimum current increases slightly faster than the maximum current resulting in decreasing PVCR. For the thinnest film of 4.5 nm, the bandgap is 14 meV. Initially, the Fermi levels are at the valence band edge. An applied bias symmetrically splits the Fermi levels such that at the peak current, one Fermi level is 15 meV below the valence band edge and the other Fermi level is 15 meV above the valence band edge, i.e. at the conduction band edge. Thus, the energy window between the two Fermi levels encompasses the bandgap. Furthermore, the majority of the conduction band transmission spectrum lies above the highest Fermi level. Thus, at peak current, as the film thickness decreases, the increasing bandgap takes up a larger fraction of the energy window between the two Fermi levels, and the conduction band is pushed above the highest Fermi level. This reduces the rate of increase of the peak current. At the current minimum, the Fermi levels are split by 60 meV and thus encompass the majority of the weight of the

transmission spectrum for all thicknesses considered, so that the valley current continues to increase as the total integrated weight of the transmission spectrum.

The reduction of the PVCR as the thickness is increased from 7.5 nm to 9 nm results from the closer proximity of the the surface Dirac point to the bulk conduction band edge. The bulk bands are shifted up in energy as a result of quantum confinement. The energy separation of the surface Dirac point (or surface valence band edge for the two thinnest films) and the bulk conduction band edge for film thicknesses of 4.5 nm, 6.0 nm, 7.5 nm, and 9.0 nm are 150 meV, 95 meV, 73 meV, and 63 meV, respectively. The transmission begins to rise about half way between the surface Dirac point and the bulk conduction band edge. This earlier 'turn-on' in the transmission, which is clearly seen for the 9 nm film in Fig. 2.4a, increases the valley current with respect to the peak current.

Since the transmission peaks occur only at the band edges, the overall tunneling current and the NDR feature are sensitive to the position of the Fermi level. Fig. 2.6b shows the change in the I-V response due to a p-type shift of ϵ_F in a 7.5 nm TI thin film. Shifting ϵ_F by 60 meV reduces the PVCR from 6.3 to 1.4. This shift of ϵ_F suppresses the tunneling current by $10^2 \sim 10^4$, and the corresponding NDR feature diminishes with it.

Chapter 3

Coulomb impurity scattering in topological insulator thin films

3.1 Introduction

Topological insulators (TI) form a new class of quantum materials with an insulating band gap in the bulk and Dirac-cone surface states. Unlike normal materials, the surface states of TI materials are robust against disorder, inhomogeneities and against time-reversal-invariant perturbations. [9,49,65,69] A combination of the high velocity of the Dirac-cone surface states and their topological protection against back-scattering make TI materials appealing from the perspective of charge transport. 3D TIs such as Bi_2Te_3 and Bi_2Se_3 have demonstrated surface state mobilities on the order of $\sim 10^4$ $cm^2V^{-1}s^{-1}$. [55,70] When the thickness of a 3D TI thin film is reduced to several quintuple layers (QLs), the high mobility is suppressed to $10^2 \sim 10^3\,cm^2V^{-1}s^{-1}$. [61, 71, 72] The suppression of the mobility in the low-temperature transport measurements has been attributed to the strong scattering from the the p-type dopants that are required to move the Fermi level (ϵ_F) close to the Dirac point [60, 72, 73] and charged surface adsorbates. [71] Prior theoretical studies focused on the effect of inhomogeneities on the transport of TI surface states on a single surface. [74, 75]

The surface states of 3D TI thin films couple and hybridize the opposite spins of the top and the bottom surface states. [1, 15, 62] A topological phase transition occurs, a surface band gap is opened as illustrated in Fig. 3.1(a), the surface band-edge group velocity decreases, and the original momentum-spin (**k**-**s**) relation that prohibits back-scattering of surface states is broken. [63] This last effect is illustrated in Fig. 3.1(c). These effects might further explain the reduction in the carrier mobility in TI thin films compared to the expected value of bulk surface states.

3.2 Boltzmann Transport Formalism

The question we seek to answer is to what extent the topological phase transition introduced by the inter-surface coupling affects the in-plane mobility of the TI surface states. To address this issue, we calculate the mobility of the coupled surface states on a TI thin film, and we explore the effects of several different externally controlled variables such as the Rashba-like splitting of the bands under interlayer bias illustrated in Fig. 3.1(b), temperature, and Fermi level.

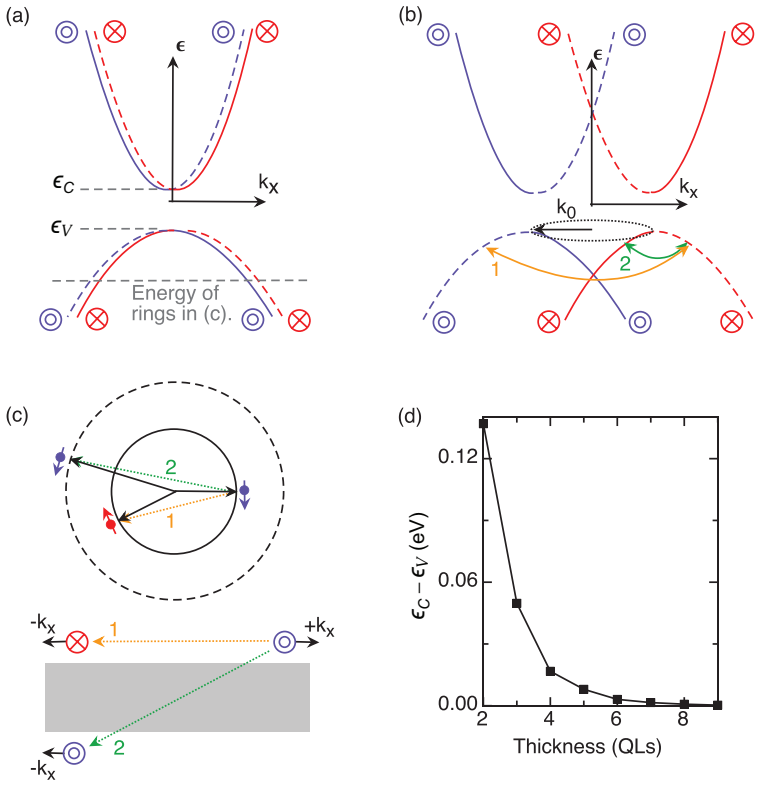

Figure 3.1:
(Color online) (a) A schematic plot of the $E-k_x$ dispersion of the degenerate gapped surface states with opposite **k-s** chiralities. Solid lines are from the top surface and dashed lines are from the bottom surface. In and out of the page spin is indicated by the arrows and color. ϵ_C and ϵ_V correspond to the conduction and valence band edges of the gapped cones. (b) The $\epsilon - k_x$ dispersion in the presence of a potential drop between the top and bottom surfaces. A Rashba-like splitting occurs. The linestyle and color scheme are the same as in (a). Processes '1' and '2' correspond to the intra-surface and inter-surface processes shown in (c). The band edges are now rings in k-space illustrated by the black dotted ring of diameter k_0. (c) The top and bottom equal-energy surface states in k-space and real space corresponding to (a). The k space iso-energy rings are offset for visualization. Intra-surface, back-scattering process '1' is prohibited by the opposite spins of the $\pm k_x$ states. Inter-surface, back-scattering process '2' is allowed since the spins of the $\pm k_x$ states are aligned. (d) Band gap of a Bi_2Se_3 given by the discretized $\mathbf{k}\cdot\mathbf{p}$ model at different quintuple layer thicknesses.

The low-energy band-structure can be described by a 4×4 $\mathbf{k}\cdot\mathbf{p}$ Hamiltonian with 4 basis states $|\chi_\alpha\rangle$ corresponding to the spin up and spin down Bi and Se p_z orbitals. [9]. We discretize in real space the k_z component of this Hamiltonian into N sites, so that each

on-site block is a 4×4 matrix. Eigenstates $|\mathbf{k}, p\rangle$ are linear combinations of the 4 basis orbitals on the N sites, $\langle \mathbf{r}|\mathbf{k}, p\rangle = \frac{e^{i\mathbf{k}\cdot\mathbf{r}}}{\sqrt{A}} \sum_{i=1}^{N} \sum_{\alpha=1}^{4} c^{p}_{\alpha,i}(\mathbf{k}) \langle \mathbf{r}|\chi_{\alpha,i}\rangle$ where α is the orbital index, i is the site index, and p is the band index. The band index runs over the 4 bands shown in Figs. 3.1(a,b) corresponding the top and bottom gapped Dirac cones of the top and bottom surfaces. Details of the discretization of this model can be found elsewhere. [1]

A typical band structure of a TI thin film is shown in Fig. 3.1(a). Hybridization of the top and bottom surface states generates a small band gap at the Dirac point. The gap decreases with increasing film thickness as shown in Fig. 3.1(d), and it is negligible beyond 6 quintuple layers.

In a thick film, opposite surfaces states have opposite **k**-**s** chiralities where **s** is the spin of state $|\mathbf{k}\rangle$. With decreasing film thickness, the opposite surface wave functions of the same momentum hybridize and mix their opposite spins, resulting in a non-zero s_z spin component. The magnitude of s_z is a measure of the strength of the inter-surface coupling which is shown in Fig. 3.2(a) as a function of energy. The maximum inter-surface coupling occurs at the gapped Dirac point, and it decreases for energies away from the band edges. This trend agrees with prior results given by both *ab inito* calculations [45] and analytical models. [62, 63]

To quantitatively determine the mobility in TI thin films, a four-band semi-classical calculation is carried out. For a screened Coulomb scattering center at layer j, the Hamiltonian matrix element between states $|\mathbf{k}, p\rangle$ and $|\mathbf{k}', \mathbf{p}'\rangle$ is written as

$$H^{j}_{\mathbf{k}',p',\mathbf{k},p} = \frac{1}{A} \sum_{i}^{N} \sum_{\alpha=1}^{4} c^{p'*}_{i,\alpha}(\mathbf{k}') c^{p}_{i,\alpha}(\mathbf{k}) \frac{q_e^2}{2\kappa} \frac{e^{-\sqrt{q_0^2+\beta^2}|z|}}{\sqrt{q_0^2+\beta^2}}, \tag{3.1}$$

where q_e is the single-electron charge, $\kappa = 100\epsilon_0$ is the static dielectric constant [76], $\beta = |\mathbf{k} - \mathbf{k}'|$, and $z = |i-j|\Delta$ is the vertical distance between site i and the layer of the Coulomb scattering center j. The discretization length $\Delta = 0.3$ nm. Eq. (3.1) results from the 2D Fourier transform of the screened Coulomb potential $\frac{q^2 e^{-q_0 r}}{4\pi\kappa r}$. The inverse screening length

q_0 is given by $q_0 = \frac{2\pi q_e^2}{\kappa}\frac{d\rho}{d\epsilon_F}$, where ρ is the 2-dimensional (2D) charge density, and ϵ_F is the Fermi energy. [77]

The group-velocity scattering rate due to each impurity on layer j is

$$S_{\mathbf{k}',p',\mathbf{k},p} = \frac{2\pi}{\hbar}|H^j_{\mathbf{k}',p',\mathbf{k},p}|^2 \cdot \left|1 - \frac{\mathbf{v}^{p'}(\mathbf{k}') \cdot \mathbf{v}^p(\mathbf{k})}{[v^p(\mathbf{k})]^2}\right| \delta(\epsilon' - \epsilon), \tag{3.2}$$

where $\mathbf{v}^p(\mathbf{k})$ and $\mathbf{v}^{p'}(\mathbf{k}')$ are the initial and final 2D group velocities. The corresponding group-velocity relaxation time is given by summing over the impurities and the final states to obtain $\frac{1}{\tau^p(\mathbf{k})} = \sum_j AN_j \sum_{\mathbf{k}',p'} S_{\mathbf{k}',p',\mathbf{k},p}$ where N_j denotes the impurity density on layer j. Following the estimates given by previous experimental investigations, [71, 72] we fix the Coulomb impurity density at $10^{13}\,\mathrm{cm}^{-2}$. To calculate the carrier mobility, an ensemble average of the group velocity driven by an external electric field is calculated at finite temperature, $\langle v_x \rangle = \frac{\sum_{\mathbf{k},\alpha} v_x^p(\mathbf{k}) f_A^p(\mathbf{k})}{\sum_{\mathbf{k},i} f_0^p(\mathbf{k})}$, where $f_A^p(\mathbf{k})$ is the asymmetric component of the non-equilibrium distribution function for band p. From a relaxation time approximation, $f_A^p(\mathbf{k}) = -\tau_i(\mathbf{k})\frac{q_e \mathcal{E}_x}{\hbar}\frac{\partial f_0^p(\mathbf{k})}{\partial k}\cos\theta$ where $\mathcal{E}_x$ is the electric field along the transport direction and θ denotes the direction of $\mathbf{k}$ with respect to the k_x axis. The mobility is defined as $\mu = \langle v_x \rangle / \mathcal{E}_x$.

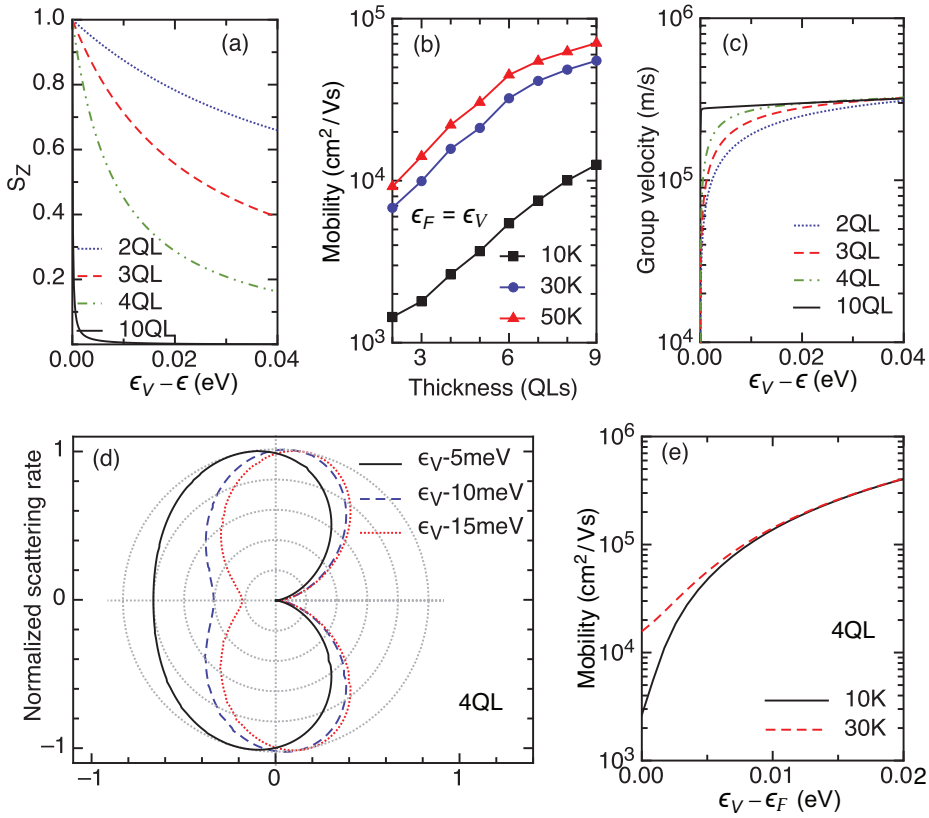

Figure 3.2:
(Color online) (a) The s_z component of a surface state as a function of energy for different film thicknesses. (b) Mobility as a function of film thickness at different temperatures with $\epsilon_F = \epsilon_V$. (c) Group velocity as a function of energy for different film thicknesses. (d) Normalized, angle resolved scattering rate for an initial state with velocity in the x direction. The film thickness is 4QL. (e) The increase in mobility due to the shift of ϵ_F into the valence band at different temperatures.

3.3 Results and Discussions

The mobilities calculated for different film thicknesses are shown in Fig. 3.2(b) for three different temperatures. The Fermi level ϵ_F is aligned with the valence band edge, ϵ_V. The mobility decreases by an order of magnitude as the film thickness decreases from 9 quintuple layers (QLs) to 2 QLs.

The inter-surface hybridization resulting from the inter-surface coupling reduces the mobility for many reasons. Once a band gap is formed, the near band-edge group

velocity decreases as shown in Fig. 3.2(c). Another factor that decreases the mobility is the increased s_z component of the spin in the states $|\mathbf{k}, p\rangle$.

On the top surface of a thick TI, the surface state can be written as a plane-wave times a spinor. For a non-magnetic scattering mechanism, the matrix element squared of the scattering potential between two states in the same band is $|H_{\mathbf{k}',\mathbf{k}}|^2 = |\langle \mathbf{k}'|H|\mathbf{k}\rangle|^2 |\langle \mathbf{s}'|\mathbf{s}\rangle|^2 = |\langle \mathbf{k}'|H|\mathbf{k}\rangle|^2 \left(1 - \cos\theta_{\mathbf{k}',\mathbf{k}}\right)$ where $\theta_{\mathbf{k}',\mathbf{k}}$ is the angle between $\mathbf{k}'$ and $\mathbf{k}$. For a bulk surface state, elastic, intra-surface backscattering is prohibited by the matrix element of the spinors.

In the case of thin films, mixing of opposite surface states introduces an s_z component to the spin so that $|\langle \mathbf{s}'|\mathbf{s}\rangle|^2 \neq \left(1 - \cos\theta_{\mathbf{k}',\mathbf{k}}\right)$ and backscattering events are no longer prohibited. Fig. 3.2(d) demonstrates the normalized, angle-resolved scattering rate for an initial state along k_x in a 4 QL film. Backscattering is significant for states close to ϵ_V where the inter-surface coupling gives $s_z \approx 1$ as shown in Fig. 3.2(a).

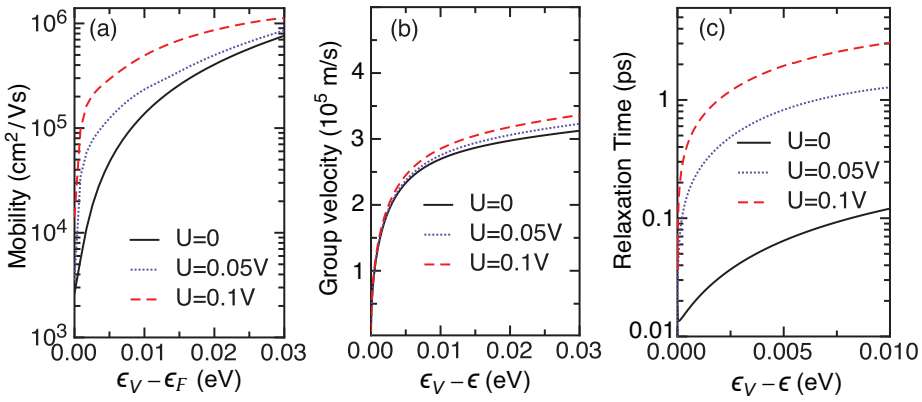

Figure 3.3:
(Color online) The effect of 3 different intersurface potentials in a 4 QL film at $T = 10$ K on (a) the mobility versus Fermi energy, (b) the group velocity versus energy, and (c) the relaxation time versus energy.

There are several ways to increase the mobility of the thin film. One way is to increase the temperature in the low-temperature transport regime where the Coulomb scattering dominates. The mobility increases by almost an order of magnitude when the temperature increases from 10 K to 50 K as shown in Fig. 3.2(b). A similar trend was observed in a transport measurement in a 6 nm Bi_2Se_3 thin film. [61] The increase in temperature

broadens the transport thermal window, so that higher energy states contribute to the carrier transport. Since inter-surface coupling decreases away from the gapped Dirac point, states away from the band edge have a higher group velocity and better back-scattering protection due to the smaller s_z component of the spin. As shown in Fig. 3.2(d), the back-scattering protection is almost restored for the states 15 meV away from ϵ_V in a 4QL thin film. For the same reasons, shifting ϵ_F away from the band edges increases the mobility as shown in Fig. 3.2(e).

Another reason for this mobility increase for energies away from the band edges is the nature of the Coulomb scattering mechanism. Since the carrier concentration of a 2D thin film is significantly smaller than that of the bulk, screening is weak. Using the bare Coulomb potential, the scattering rate given by Eq. 3.2 can be simplified to $\tilde{S}_{\mathbf{k}',\mathbf{k}} = \frac{2\pi}{\hbar}\frac{q_e^4}{4A^2\kappa^2\beta^2} I_{\mathbf{k}',\mathbf{k}} \left(1-\cos\theta\right)\delta\left(\epsilon-\epsilon'\right)$ where $I_{\mathbf{k}',\mathbf{k}} = |\sum_i^N \sum_{\alpha=1}^4 c_{i,\alpha}^{p'*}(\mathbf{k}')c_{i,\alpha}^{p}(\mathbf{k})|^2$ is the overlap integral. For states close to the band edge, the two degenerate bands from oppisite surfaces have large but opposite s_z components, and, as a result, the inter-band overlap integral is close to zero. Thus, inter-surface scattering processes are neglected. States close to the band edge on the same surface have large and aligned s_z components, so that $I_{k',k} \approx 1$. For low-energy, intra-surface scattering, the group-velocity relaxation time can be calculated analytically as $\frac{1}{\tilde{\tau}(\mathbf{k})} = AN\sum_{\mathbf{k}'}\tilde{S}_{\mathbf{k}',\mathbf{k}} = \frac{Nq_e^4}{8\hbar^2\kappa^2 kv}$ where N is the total surface density of the Coulomb scattering centers. The relaxation time is proportional to the group velocity, v, and the radius of the contour of equal energy, k. Thus, as ϵ_F moves away from the band edge, kv at the Fermi level increases, so that states with greater relaxation times are included in the transport thermal window. Since μ is proportional to τ, increasing the kv product increases the mobility at low temperatures.

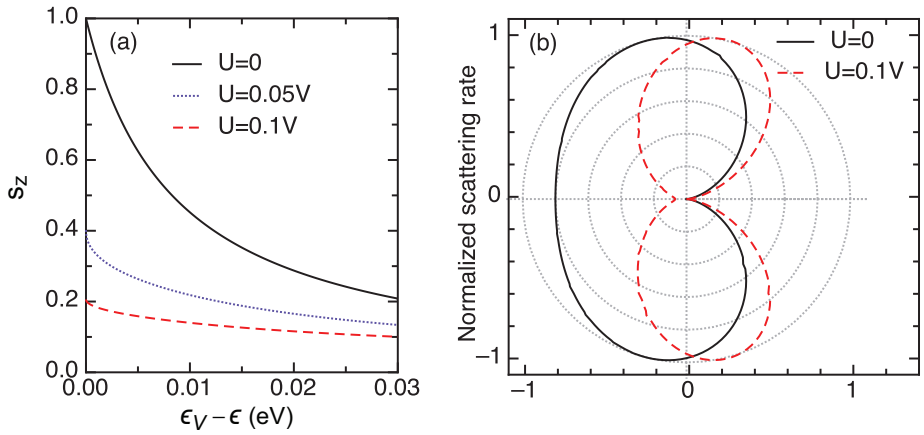

Figure 3.4:
(Color online) (a) The s_z component of a surface state as a function of energy for different interlayer potentials. (b) Normalized, angle resolved scattering rate for an initial state with velocity in the x direction for two different interlayer potentials. The film thickness is 4 QL, $\epsilon_F = \epsilon_V - 5$ meV, and $T = 10$ K.

The mobility is further enhanced by a vertical potential drop (U) through the thin film which creates a Rashba-like splitting of the bands as shown in Fig. 3.1(b). Experimentally, this can be achieved by creating different electrostatic environments on each surface such as applying a strongly coupled substrate or using gating mechanisms. [78] The vertical potential drop leads to a structural inversion asymmetry (SIA) that can restore the topologically nontrivial surface states in a TI thin film. [62–64] As demonstrated in Fig. 3.3(a), for a 4QL TI thin film, a vertical potential drop of 0.1 V enhances the mobility by up to an order of magnitude when ϵ_F is close to the valence band edge. The reduced inter-surface coupling is evident in the reduced s_z component of the spin close to the Rashba-split band edges shown in Fig. 3.4(a). The suppressed s_z component restores the back-scattering protection. As demonstrated in Fig. 3.4(b), back-scattering is suppressed for states 5 meV away from ϵ_V when a vertical potential drop of 0.1 V is applied.

Besides the reduced inter-surface coupling, another reason for the mobility increase given by the Rashba-like splitting is the change in the band structure. As illustrated in Fig. 3.1(b), the surface-to-surface potential drop creates a valence band edge that is a ring in

k-space. The band edge forms a circle of radius k_0 that increases with U. The increase in kv linearly increases the relaxation time. Although the band-edge group velocity is almost unchanged due to the Rashba-splitting as shown in Fig. 3.3(b), the relaxation time increases by almost an order of magnitude when the potential drop increases from 0 to 0.1 V as demonstrated in Fig. 3.3(c). The corresponding mobility is enhanced from $\sim 10^3\,\mathrm{cm^2V^{-1}s^{-1}}$ to $\sim 10^4\,\mathrm{cm^2V^{-1}s^{-1}}$.

Chapter 4

Topological spin Hall effect resulting from magnetic skyrmions

4.1 Introduction

Transverse spin accumulation in semiconductors due to extrinsic spin-orbit scattering was first predicted by Dyakonov and Perel [79, 80]. Strong spin-orbit coupling (SOC) of the disorder scatters different spins in opposite directions leading to a non-zero transverse spin current perpendicular to the charged current. Evidences of the predicted asymmetric scattering of different spins was later observed in optical [81] and photovoltaic [82] experiments. Hirsch named this phenomenon the 'spin Hall effect' (SHE) and proposed that the chargeless transverse spin current can be transferred back to a Hall voltage using an inverse SHE measurement [83]. Later theoretical studies predicted an intrinsic contribution to the SHE in the presence of SOC due to the topological property of the Bloch states at the Fermi surface [33, 84–86]. Direct observations of the SHE have been experimentally achieved in semiconductors using Kerr rotation microscopy [87, 88].

In magnetic materials due to SOC, extrinsic or intrinsic mechanisms can lead to a non-linear contribution to classical Hall signal [89–91]. The non-linearity which is proportional to the magnetization is a result of the transverse accumulation of itinerant

majority spins resulting in the anomalous Hall effect (AHE) [12]. Similar to the SHE, the AHE can result from an intrinsic or extrinsic mechanism. The intrinsic contribution to the AHE is related to the Berry curvature within the Fermi surface, which is determined by the topological nature of the Bloch bands [91, 92].

The momentum-space topological origin of the intrinsic AHE is the same to that of the intrinsic SHE. Similarly, the real-space topology of a magnetic system can also induce a Hall effect [93]. An electron hopping through magnetic sites with particular chiral textures acquires a Berry phase and thus experiences an emergent gauge field during transport [94]. The emergent gauge field generates a Hall voltage that does not originate from SOC, which is usually referred to as the 'topological Hall effect' (THE) [27]. Recently, a skyrmion lattice, a topologically non-trivial chiral spin texture, has been observed in helical magnets with a Dzyaloshinskii-Moriya (DM) interaction [31, 95, 96]. These materials provide robust samples where the THE has been detected, and the measured Hall signal is a signature of the skyrmion phase in many B20 magnetic compounds [26, 30, 97, 98].

In the adiabatic limit, each electron spin passing through a single skyrmion has its spin aligned with the direction of spatial magnetization of the skyrmion which generates an emergent gauge field of up to one flux quantum [96]. This flux quantum confined in the area of a single skyrmion gives a gigantic effective field, that makes the THE a possible detection method for skyrmions. Moreover, the direction of the local magnetic field generated by this emergent gauge field is opposite for parallel and antiparallel spin, which deflects them in opposite directions. This might separate the spin current from the charge current, generating an unconventional topological spin Hall effect (TSHE) which does not originate from band topology. Motivated by these possibilities, in this chapter we theoretically investigate the THE and the TSHE resulting from a single magnetic skyrmion. The TSHE phenomenon discovered here can be explained in terms of a general physical picture that would apply equally well to a skyrmion lattice.

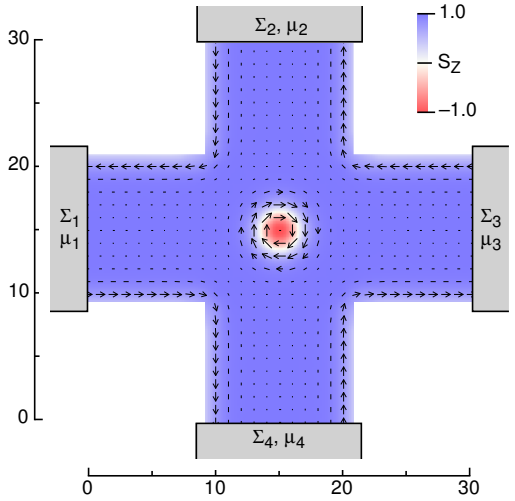

Figure 4.1:
(color online) The geometry of a 31×31 tight-binding cross bar. The arrows denote the in-plane component of the magnetization texture of a single skyrmion. The color plot demonstrates the S_z component. The four terminals are numbered clock-wise.

4.2 Methods

Due to the lack of periodicity, we apply the non-equilibrium Green's function method (NEGF) to simulate the coherent transport of itinerant spins traversing a single magnetic skyrmion [99]. The tight-binding electron Hamiltonian we employ is,

$$\mathbf{H}_{\mathrm{e}} = -J_{\mathrm{H}} \sum_{i} c_i^{\dagger} \boldsymbol{\sigma}_i c_i \cdot \mathbf{S}_i - t \sum_{\langle i,j \rangle} \left(c_i^{\dagger} c_j + \mathrm{h.c.} \right), \tag{4.1}$$

where $\boldsymbol{\sigma}_i$ is the spin of itinerant electrons, J_{H} is the Hunds' rule coupling, t is the nearest neighbor hopping, and $\mathbf{S}_i$ is the local magnetization. It has been previously discussed that the external magnetic field does not contribute much to the Hall effect, therefore we neglect its effect on the electron by taking the hopping parameter to be real [12]. Thus, the Hall signal observed in the following calculations is purely from the emergent gauge field of the skyrmion. The spin texture $\{\mathbf{S}_i\}$ contains a single skyrmion located at the center of a 4-terminal cross bar (as shown in Fig. 4.1). This texture is fully damped

using the Landau-Lifshitz-Gilbert (LLG) equation with the magnetic Hamiltonian $H_{\rm S} = -J\sum_{\langle i,j\rangle}\mathbf{S}_i\cdot\mathbf{S}_j - D\sum_{\langle i,j\rangle}\hat{\mathbf{r}}_{i,j}\cdot\mathbf{S}_i\times\mathbf{S}_j - \sum_i \mathbf{h}_0\cdot\mathbf{S}_i$. Here J is the nearest neighbor exchange coupling, D is the DM interaction and $\mathbf{h}_0$ is the external magnetic field perpendicular to the cross-bar plane. For simplicity we choose $D = J = h_0^z$. Periodic magnetic boundaries are applied at the terminals in order to mimic the semi-infinite ferromagnetic leads. Other boundaries along the cross bar are taken as magnetic open boundaries, which gives large in-plane magnetization components at the edges. These boundary conditions have been applied to simulate helimagnetic ribbons [32]. The skyrmion at the center is generated by manually creating a unity topological charge and then relaxing the spin texture until the magnetic energy is stable. Details of the magnetic dynamical simulations can be found in Ref. [100].

For the electron transport calculation, semi-infinite boundary conditions for electron states are applied to the four terminals of the cross bar. Each terminal is assumed to be a thermal bath of carriers with chemical potential μ_m. The semi-infinite electrodes are included by adding self-energy terms, $\mathbf{\Sigma}_m = \mathbf{t}^\dagger\mathbf{g}_m^R\mathbf{t}$, to the terminal blocks of $\mathbf{H}_{\rm e}$, where $\mathbf{g}_m^R$ is the surface Green's function of terminal m. The retarded Green's function of the device region bounded by the terminals is given by $\mathbf{G}^R = [\epsilon\mathbf{I} - \mathbf{H}_{\rm e} - \sum_m \mathbf{\Sigma}_m]^{-1}$. In the linear response limit, the zero-temperature terminal currents, I_m, are given by $I_m = (e/h)\sum_n T_{m,n}\delta\mu_n$. $\delta\mu_n$ denotes the chemical potential shift due to an applied bias in terminal n, ($\delta\mu_n = \mu_n - \epsilon_F$). $T_{m,n} = {\rm Tr}\left[\mathbf{\Gamma}_m\boldsymbol{G}_{mn}^R\mathbf{\Gamma}_n\boldsymbol{G}_{mn}^A\right]$ ($m \neq n$) is the transmission coefficient between terminal m and n, where $\mathbf{G}_{mn}^A = \mathbf{G}_{mn}^{R\dagger}$, and $\mathbf{\Gamma}_m = i\left(\mathbf{\Sigma}_m - \mathbf{\Sigma}_m^\dagger\right)$. At steady state, the charge current is conserved such that $T_{mm} = -\sum_{n\neq m} T_{mn}$. A Symmetric bias is applied between terminals 1 and 3, $\delta\mu_1 = -\delta\mu_3 = \delta\mu = 0.1J_{\rm H}$. Enforcing $I_2 = I_4 = 0$ in the Hall effect measurement, the transverse Hall voltage can be solved as

$\delta\mu_2 = \delta\mu\,(P-Q)\,/\,(P+Q)$ and $\delta\mu_4 = \delta\mu\,(R-S)\,/\,(R+S)$, where

$$\begin{cases} P = T_{21}T_{41} + T_{21}T_{42} + T_{21}T_{43} + T_{24}T_{41} \\ Q = T_{23}T_{41} + T_{23}T_{42} + T_{23}T_{43} + T_{24}T_{43} \\ R = T_{42}T_{21} + T_{21}T_{41} + T_{23}T_{41} + T_{24}T_{41} \\ S = T_{42}T_{23} + T_{21}T_{43} + T_{23}T_{43} + T_{24}T_{43} \end{cases} . \tag{4.2}$$

Thus, the topological Hall angle can be evaluated as $\tan\theta_{\mathrm{TH}} = E_H/E_x = (\mu_2-\mu_4)/(\mu_1-\mu_3)$.

Once $\delta\mu_m$ and I_m are obtained, then the total terminal spin current, $I_m^{S_\alpha}(\alpha = x, y, z)$, is evaluated from $I_m^{S_\alpha} = \frac{\hbar}{2}\mathrm{Tr}\left[\boldsymbol{\sigma}_\alpha \mathbf{I}_m^{\mathrm{neq}}\right]$, where $\boldsymbol{\sigma}_\alpha = \mathcal{I}\otimes\sigma_\alpha$ is the extended Pauli matrix and $\mathbf{I}_m^{\mathrm{neq}}$ is the terminal current operator $\mathbf{I}_m^{\mathrm{neq}} = \frac{i}{2\pi\hbar}\left[\delta\mathbf{G}_m^n\boldsymbol{\Sigma}_m^\dagger - \boldsymbol{\Sigma}_m\delta\mathbf{G}_m^n + \mathbf{G}_m^R\delta\boldsymbol{\Sigma}_m^{\mathrm{in}} - \delta\boldsymbol{\Sigma}_m^{\mathrm{in}}\mathbf{G}_m^A\right]$, $\delta\mathbf{G}_m^n = \sum_n \mathbf{G}_{m,n}^R\boldsymbol{\Gamma}_{n,n}\mathbf{G}_{n,m}^A\delta\mu_n$, and $\delta\boldsymbol{\Sigma}_m^{\mathrm{in}} = \boldsymbol{\Gamma}_m\left(\epsilon_F\right)\delta\mu_m$. The intensity of the TSHE is described by the spin Hall angle, a renormalized ratio between the transverse spin current and the longitudinal charged current

$$\theta_{\mathrm{TSH}} = \left(\frac{2e}{\hbar}\right)\frac{\sigma_{xy}^{S_z}}{\sigma_{xx}} = \left(\frac{2e}{\hbar}\right)\frac{I_{42}^{s_z}}{I_{13}}, \tag{4.3}$$

where $I_{13} = I_1 - I_3$, and $I_{42}^{S_z} = I_4^{S_z} - I_2^{S_z}$.

4.3 Results and Discussions

First, we study the THE and TSHE for the case of pure spin injection. By setting $t = 0.2J_{\mathrm{H}}$, the tight-binding band-width is smaller than the spin splitting given by J_{H}. Therefore no matter where the the Fermi level lies, the electron injection does not mix different spins. The θ_{TH} and θ_{TSH} for different positions of ϵ_F are shown in Fig. 4.2(a) and (b), respectively. The corresponding surface density of states (DOS) that determines the type of current injection at terminal 1 is shown in Fig. 4.2(c). When the surface DOS is zero, the Fermi surface lies in the spin gap, and injection is absent, so that both θ_{TH} and

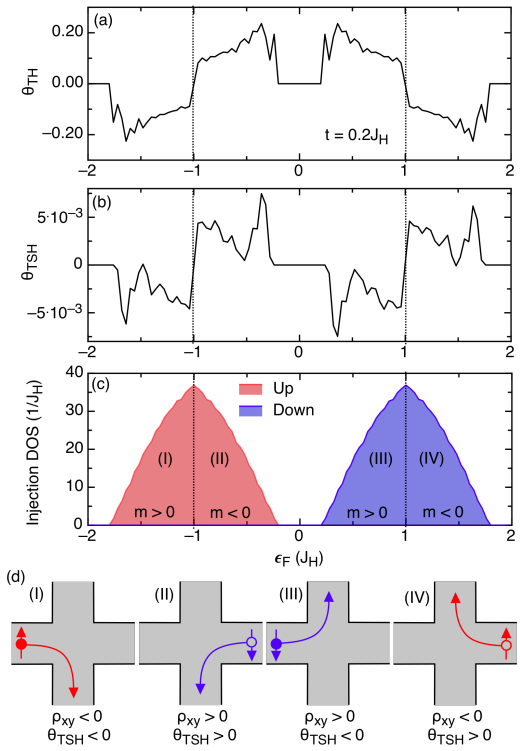

Figure 4.2:
(color online) THE and TSHE for the case of pure spin injection ($t = 0.2J_{\mathrm{H}}$). The (a) Hall angle θ_{TH} and the (b) spin Hall angle θ_{TSH} are shown as a function of ϵ_F. The surface density of states at terminal 1 is shown in (c). The four scenarios of different carrier-type and spin compositions are illustrated in (d).

θ_{TSH} are suppressed to zero. As ϵ_F passes through the bands, pure spin injection gives a Hall angle up to ± 0.2 indicating the expected THE. The corresponding value of θ_{TSH} is within ± 0.005. At $\epsilon_F = \pm J_{\mathrm{H}}$, both θ_{TH} and θ_{TSH} change sign.

The sign change of the Hall angles can be explained by the spin and carrier-type composition of the injection from the ferromagnetic contacts. For each transport channel, a one-dimensional tight-binding chain gives a negative cosine electron band dispersion, which has a sign change of the effective mass at the band center. The effective mass (m^*) is positive at the bottom band-edge, and becomes negative at the top. When an up-spin electron with positive m^* is injected from terminal 1, it is scattered to the "right" due to the effect of the emergent gauge field generated by the skyrmion. This is denoted as scenario (I) in Fig. 4.2(d). Alternately when $m^* < 0$, an up-spin electron injected from terminal 1 is equivalent to a down-spin hole injected from terminal 3. Since the spin scattering due to the skyrmion is anti-symmetric, the down-spin hole is scattered to its "left" as denoted by scenario (II). In a multi-channel scenario due to the transverse confinement, the tight-binding band splits into several sub-bands. Thus, the number of the electron bands and the hole bands crossing the Fermi level changes at different positions of ϵ_F. As ϵ_F moves from the bottom band-edge to the band-center, the number of electron bands crossing ϵ_F decreases, while the number of hole bands increases as depicted in Fig. 4.2(c). Right at the band-center, the electrons and holes are equal, indicating an equal contribution from both scenarios (I) and (II), which leads to a cancellation of both θ_{TH} and θ_{TSH}. Further increasing ϵ_F, scenario (II) starts to dominate such that θ_{TH} and θ_{TSH} change sign. Similar arguments can be applied to scenario (III) and (IV) for the down-spin case (see Fig. 4.2(d)).

Semiclassically, the relative strength of THE to the TSHE can understood as a cancellation of the transverse electric field due to charge accumulation at contacts (2) and (4) with the gauge field of the skyrmion. In all these pure-spin injection scenarios, the spin current is carried by charge which leads to a transverse accumulation of charge resulting in a Hall voltage and hence a THE. Since the transverse electric field cancels the Lorentz force given by the emergent gauge field of the skyrmion, a continuous spin current is suppressed at

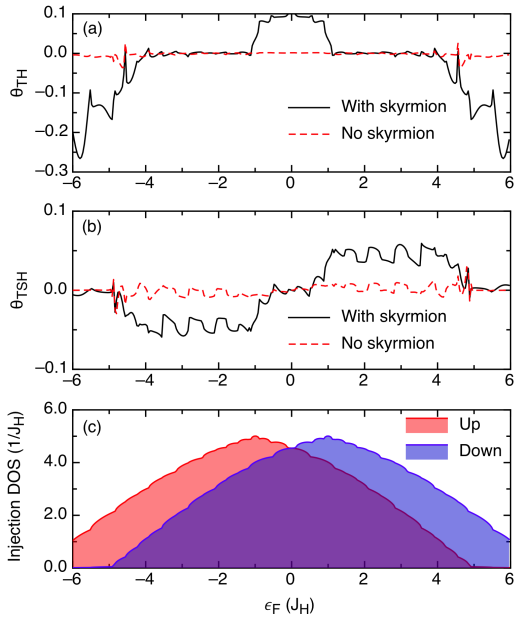

Figure 4.3:
(color online) THE and TSHE in the case of mixed spin injection ($t = 1.5J_{\mathrm{H}}$). (a) and (b) demonstrate the values of θ_{TH} and θ_{TSH} for different positions of ϵ_F. The red dashed lines correspond to the case where the central skyrmion is removed. (c) is a plot of the surface DOS at terminal 1.

the steady state, making the TSHE insignificant. However, an order-of-magnitude increase in θ_{TSH} can be achieved in the case of mixed spin injection which we discuss next.

To simulate mixed spin injection, the hopping term is increased to $t = 1.5J_{\mathrm{H}}$ such that the injection band-widths of each spin are enlarged and overlap in some range of ϵ_F. The calculated values of the θ_{TH} and θ_{TSH} are shown in Fig. 4.3, along with the corresponding results in the absence of a skyrmion for comparison. For energies in the range of $-4.5J_{\mathrm{H}} < \epsilon_F < -J_{\mathrm{H}}$ and $J_{\mathrm{H}} < \epsilon_F < 4.5J_{\mathrm{H}}$, θ_{TH} vanishes to ~ 0, whereas θ_{TSH} increases by approximately an order of magnitude compared to the case of pure-spin injection. Additionally, in the energy range $-J_{\mathrm{H}} < \epsilon_F < J_{\mathrm{H}}$, the Hall angle corresponding to the THE θ_{H} is finite and roughly same order as that in the case of pure-spin injection.

To explain the presence of the TSHE, we again refer to the four scenarios shown in Fig. 4.2(d). Within $-4.5J_{\mathrm{H}} < \epsilon_F < -J_{\mathrm{H}}$, the transport is dominated by scenario (I)+(III)

as shown in Fig. 4.3(c). In this case, both the spin-up and spin-down electrons are injected from terminal 1. Due to the presence of a skyrmion there exists a topological Hall effect which produces a transverse electrical field, E_{TH}. At steady state, the zero-current condition at terminals 2 and 4 requires $eE_{\mathrm{TH}} = -F\uparrow$ and $eE_{\mathrm{TH}} = -F\downarrow$ satisfied simultaneously. Due to the chirality of the skyrmion, the emergent field experienced by the up spin is opposite to that experienced by the down spin, which generates opposite emergent Lorentz forces on the two types of spins ($F\uparrow = -F\downarrow$). Therefore, the zero-current condition in the transverse direction cannot be satisfied unless $E_{\mathrm{TH}} = 0$. Although imbalanced spin injection occurs due to the ferromagnetic electrodes, the THE must be suppressed in steady state as long as the transport is dominated by the same type of carrier. Since there is no electrostatic field to balance the emergent Lorentz force, a continuous chargeless spin current is established. Similar explanations [(II)+(IV)] can be applied for $J_{\mathrm{H}} < \epsilon_F < 4.5J_{\mathrm{H}}$.

When the transport is dominated by two different types of carriers with the same spin, the TSHE is suppressed, and the THE voltage becomes finite. In our calculations, this occurs when ϵ_F is within $[-J_{\mathrm{H}}, J_{\mathrm{H}}]$, and the transport is dominated by the scenarios (II)+(III). In this case the down-spin electrons and holes are injected from terminals 1 and 3, respectively. The electrons and holes are scattered in opposite directions and then accumulate at terminals 2 and 4, respectively. Since the same spin is assigned to opposite charges, a non-zero E_{TH} develops at terminals (2) and (4) resulting in a finite THE with a vanishing TSHE.

To further demonstrate the differences between the THE and the TSHE, we show the vector map of the spin current density $\mathbf{J}_{S_z}(\mathbf{r})$ and the corresponding color map of the charge accumulation in Fig. 4.4. The spin texture and the terminal numbering are the same as in Fig. 4.1. For the THE case shown in Fig. 4.4(a), $\epsilon_F = -0.05J_{\mathrm{H}}$ and the transport is dominated by scenario (II)+(III). There is a net drop in the transverse chemical potential between leads 2 and 4. The $\mathbf{J}_{S_z}$ vectors circulate symmetrically on either side of the skyrmion, generating no significant total transverse spin current. This corresponds to the case where $\theta_{\mathrm{TH}} \approx -0.2$ and $\theta_{\mathrm{TSH}} \approx 0$. For the TSHE case shown in [Fig. 4.4(b)], the

transport is dominated by scenario (I)+(III). The equal-potential contour of $\delta\mu\,(\mathbf{r}) = 0$ cuts all the way across the vertical bar indicating little charge imbalance between leads 2 and 4. In transverse leads 2 and 4 there is a net spin current directed from lead 2 to lead 4 giving a negative $\theta_{\mathrm{TSH}} \approx -0.05$.

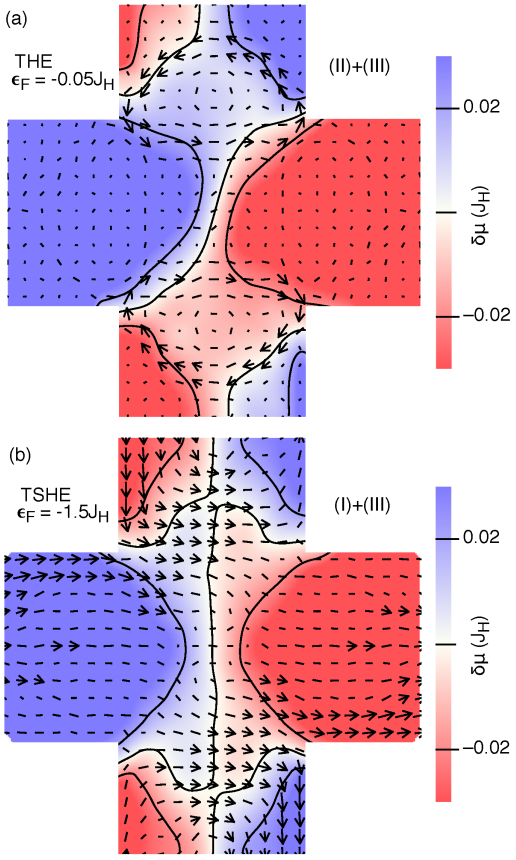

Figure 4.4:
(color online) Vector map of $\vec{J}_{S_z}$ (arrow plot) and the effective chemical potential distribution (color map) for (a) the THE and (b) the TSHE. A longitudinal applied bias of $\delta\mu_1 = -\delta\mu_3 = 0.1J_{\mathrm{H}}$ is applied. For the THE (a), the spin current symmetrically circulates on either side of the the skyrmion resulting in no net transverse spin current. The electron and hole accumulation induces an imbalanced transverse potential distribution. For the TSHE (b), the transverse chemical potential distribution is symmetric, and a charge-less spin current is established in the transverse direction.

The TSHE discussed here is of similar magnitude as the SHE in broadly used Pt thin films [101]. However, the physical mechanism giving rise to the TSHE is fundamentally

different from the one leading to the spin Hall effect in strong spin orbit coupled systems. In such systems, the spin Hall effect results from the topological property of the Bloch bands in momentum space. In contrast the TSHE results from the topological property of the skyrmion spin texture in real space. The real-space topology exerts opposite emergent Lorentz forces on different spins, which can induce the TSHE.

Chapter 5

Topological charge analysis of ultra-fast skyrmion creation due to spin transfer torques (STTs)

5.1 Introduction

Magnetic skyrmions are topologically protected spin textures in which the local moments on a two dimensional lattice point in all directions with a topologically nontrivial mapping to the unit sphere [19, 102]. Physically, each skyrmion is a circular spin texture in which the spins on the periphery are polarized vertically, the central spin is polarized in the opposite direction, and, in between, the spins smoothly transition between the two opposite polarizations. A swirling transition, which is effectively a circle of double Bloch-type domain wall, gives a Bloch-type skyrmion. This type of skyrmion was first discovered in the temperature-magnetic field (T-H) phase diagram of B20 magnets [24,31,95]. In these materials, the atomic structure of the lattice breaks the inversion symmetry, inducing an asymmetric Dzyaloshinsky-Moriya (DM) exchange interaction [22, 103]. The competition between the DM exchange and the symmetric Heisenberg exchange stabilizes the skyrmion

phase in these materials. A Neel-type skyrmion, on the other hand, is a wrapped double Neel-wall. Such a skyrmion is stabilized by an interfacial DM interaction, which is originated from the broken interfacial inversion symmetry. This type of DM interaction is usually observed at the interface between a magnetic thin film and a layer of heavy metal with strong spin-orbit coupling (SOC). For both types of skyrmions, the radius, ranging from about 3 nm to 100 nm [24, 31, 95, 104], is determined by the ratio of the strengths of the DM interaction and the Heisenberg interaction [105].

Skyrmion lattices and isolated skyrmions in both bulk and thin films have been observed by neutron scattering [95, 106], Lorentz transmission electron microscopy [24, 30, 31, 107, 108], and spin-resolved scanning tunneling microscopy (STM) [109]. Current can drive skyrmion spin textures with a current density 4-5 orders of magnitude lower than that required to move conventional magnetic domain walls [25, 96, 108, 110]. This suggests promising spintronic applications exploiting the topological spin texture as the state variable [23, 32, 111].

A two-dimensional skyrmion lattice may be formed under a uniform magnetic field [31, 95], however, the switching of isolated, individual skyrmions is far more challenging. The single skyrmion switching was first experimentally demonstrated by injecting spin-polarized current from an STM tip into ultra-thin Pd/Fe/Ir(111) films at 4.2 K [112]. Other schemes of single skyrmion switchings, such as using a sharp notch [32], a circulating current [113], thermal excitations [114] and spin-orbit torques (SOTs) [111] have been proposed. Spintronic applications call for on-wafer solutions to precisely control the position and the time of skyrmion switchings with good reliability. This is rather difficult because each switching event corresponds to a topological transition, which has to break the protection given by the topological order. This process has to overcome the topological protection barrier, which is both energetically unfavorable and difficult to manipulate. In this chapter, we theoretically investigate the topological transition of the microscopic spin texture during a dynamical skyrmion creation process. This picture provides insight into the critical condition to create isolated skyrmions and a quantitative understanding in the

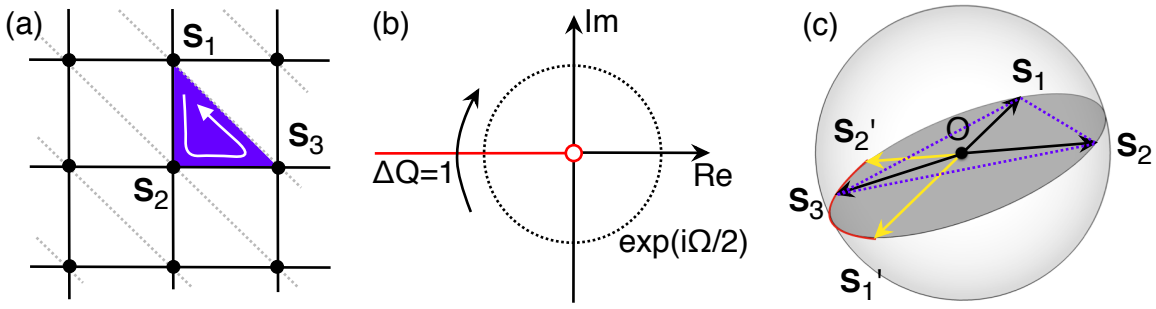

Figure 5.1:
(color online) The critical condition of a topological transition. (a), Triangulated square lattice. $\mathbf{S}_1$, $\mathbf{S}_2$ and $\mathbf{S}_3$ follow a counter-clockwise order on each triangle grid. (b), $\exp\left(\frac{i\Omega}{2}\right)$ on the complex plane. The branch cut is denoted by the red line on the negative real axis. (c), A typical spin configuration at the moment of a topological transition. It only occurs when $\mathbf{S}_3$ crosses the geodesic $\mathbf{S}_1'\mathbf{S}_2'$ (red arc). $\mathbf{S}_1'$ and $\mathbf{S}_2'$ are the point reflection images of $\mathbf{S}_1$ and $\mathbf{S}_2$ about the sphere center.

topological barrier. Based on this picture, we propose that controlled skyrmion creation can be realized by the spin transfer torques (STTs) induced from a magnetic electrode. Such a geometry and creation mechanism is applicable to both of the Bloch-type and the Neel-type skyrmions, and is potentially compatible with the standard metal process used in silicon integrated circuits.

5.2 Topological transition analysis

The critical condition of the topological transition is determined by the topological charge evolution during a spin dynamical process. A skyrmion is distinguished from a ferromagnet or other trivial state by the topological charge Q, which is a non-vanishing integer [21, 115]. Each skyrmion contributes ± 1 to the total topological charge. Usually $Q = \frac{1}{4\pi}\int d^2r\mathbf{S}\cdot(\partial_x\mathbf{S}\times\partial_y\mathbf{S})$ is employed, but it is well defined only in the continuum limit where all the spins are almost parallel to their neighbors [115]. In this limit, magnetic dynamical processes can only distort the geometry of the spin texture, but cannot change

the wrapping number in the spin space. Thus, the topological charge above is conserved, and can not capture the precise time evolution of the topological transition.

Here we employ the lattice version of the topological charge that provides a microscopic picture of the spin evolution and reveals the microscopic criteria for a topological transition to occur during any dynamical process. This version of Q was first introduced by Berg *et al.* [116], which is defined on a square lattice mesh illustrated in Fig. 5.1 (a). The calculation of Q starts by triangulating the entire lattice and then counting the solid angles $\Omega_{\triangle}$ for each triangle $\triangle(\mathbf{S}_1, \mathbf{S}_2, \mathbf{S}_3)$ determined by

$$\exp(i\frac{\Omega_{\triangle}}{2}) = \rho^{-1}[1 + \mathbf{S}_1 \cdot \mathbf{S}_2 + \mathbf{S}_2 \cdot \mathbf{S}_3 + \mathbf{S}_3 \cdot \mathbf{S}_1 + i\mathbf{S}_1 \cdot (\mathbf{S}_2 \times \mathbf{S}_3)], \tag{5.1}$$

where $-2\pi < \Omega < 2\pi$ and $\rho = [2(1+\mathbf{S}_1 \cdot \mathbf{S}_2)(1+\mathbf{S}_2 \cdot \mathbf{S}_3)(1+\mathbf{S}_3 \cdot \mathbf{S}_1)]^{1/2}$ is the normalization factor [116]. The lattice version of the topological charge Q is then given by summing over all of the triangles.

$$Q = \frac{1}{4\pi} \sum_{\triangle} \Omega_{\triangle} \tag{5.2}$$

From this definition, the directional solid angle $\Omega_{\triangle}$ ranges from -2π to 2π so that the negative real axis of the complex plane in Eq. (5.1) is a branch cut. The exponential $e^{i\Omega_{\triangle}/2}$ lies on the branch cut in the complex plane when $\mathbf{S}_1 \cdot (\mathbf{S}_2 \times \mathbf{S}_3) = 0$, and $1 + \mathbf{S}_1 \cdot \mathbf{S}_2 + \mathbf{S}_2 \cdot \mathbf{S}_3 + \mathbf{S}_3 \cdot \mathbf{S}_1 < 0$. $\Omega_{\triangle}$ is 2π immediately above, and -2π immediately below, the branch cut. Any dynamical process causing $e^{i\Omega_{\triangle}/2}$ to cross the branch cut is accompanied by a change in the topological charge of ± 1 as shown in Fig. 5.1 (b). To trigger an event crossing the branch cut, the dynamical process must drive three spins $\mathbf{S}_1$, $\mathbf{S}_2$, $\mathbf{S}_3$ in one particular triangle coplanar from the condition $\mathbf{S}_1 \cdot (\mathbf{S}_2 \times \mathbf{S}_3) = 0$. The other condition $1 + \mathbf{S}_1 \cdot \mathbf{S}_2 + \mathbf{S}_2 \cdot \mathbf{S}_3 + \mathbf{S}_3 \cdot \mathbf{S}_1 < 0$ leads to the inequality $(\mathbf{S}_1 - \mathbf{S}_2) \cdot (\mathbf{S}_3 - \mathbf{S}_2) > 0$, so that $\angle \mathbf{S}_1\mathbf{S}_2\mathbf{S}_3$ is an acute angle, and the same holds true for permutations of the three indices 1, 2, and 3. Consequently, three spins must point 'away' from each other at the branch cut.

For fixed $\mathbf{S}_1$ and $\mathbf{S}_2$, $\mathbf{S}_3$ must lie on the arc $\mathbf{S}_{1'}\mathbf{S}_{2'}$ as shown in Fig. 5.1 (c). This coplanar but highly non-collinear critical state must be achieved during skyrmion switching events.

Based on this switching criteria, the energy barrier protecting the topological charge is identified, and can thus be quantified. The full spin Hamiltonian of a magnetic helix is given by

$$H = \sum_{\langle i,j \rangle} [-J\mathbf{S}_i \cdot \mathbf{S}_j + H_{i,j}^{\mathrm{DM}}] - \mu_0 \sum \mathbf{S}_i \cdot \mathbf{B}_{\mathrm{Ost}}, \tag{5.3}$$

where

$$\begin{cases} H_{i,j}^{\mathrm{DM}} = D\hat{\mathbf{r}}_{ij} \cdot (\mathbf{S} \times \mathbf{S}_j) & \text{(Bloch type)} \\ H_{i,j}^{DM} = D\left(\hat{\mathbf{z}} \times \hat{\mathbf{r}}_{ij}\right) \cdot (\mathbf{S}_i \times \mathbf{S}_j) & \text{(Neel type)} \end{cases}.$$

The two terms in the square bracket are the Heisenberg and DM interactions, respectively, and the last term is the Zeeman coupling. In the case of the co-planner configuration, the DM interaction of either type does not contribute to the total energy. Thus, at the moment of switching, the energy density given by the three spins involved in the topological transition is

$$\begin{aligned} \Delta\epsilon &= J\left(1 - \frac{\mathbf{S}_1 \cdot \mathbf{S}_2}{2} - \frac{\mathbf{S}_2 \cdot \mathbf{S}_3}{2}\right) && (5.4) \\ &\quad + \mathbf{B}_{\mathrm{Ost}} \cdot \left(\frac{1}{2} - \frac{\mathbf{S}_1 + \mathbf{S}_2 + \mathbf{S}_3}{6}\right). && (5.5) \end{aligned}$$

Since the spins at the transition are highly non-collinear, the Zeeman coupling is much weaker compared to the exchange contribution, and the second term in Eq.5.4 is thus neglected. From the topological transition requirement, $1 + \mathbf{S}_1 \cdot \mathbf{S}_2 + \mathbf{S}_2 \cdot \mathbf{S}_3 + \mathbf{S}_3 \cdot \mathbf{S}_1 < 0$, it can be obtained that $-J(\mathbf{S}_1 \cdot \mathbf{S}_2 + \mathbf{S}_2 \cdot \mathbf{S}_3) > J(1 + \mathbf{S}_3 \cdot \mathbf{S}_1) \geq 0$. Thus, $\Delta\epsilon > J$ has to be satisfied. The maximum value of $\Delta\epsilon$ occurs when $\mathbf{S}_2$ is anti-aligned with both $\mathbf{S}_1$ and $\mathbf{S}_3$, such that $J < \Delta\epsilon < 2J$. In different switching processes, the actual value of this barrier varies within this range, determined by the exact spin configurations at the moment of the transition. Since this criteria comes from the generic topological charge analysis, it applies for both the Bloch-type and the Neel-type skyrmions.

5.3 SST induced switching

Spin transfer torques (STT) induced by pure spin currents or spin polarized charged currents have been proposed to be a promising mechanism to switch nano-magnets in spintronic integrated circuits [117, 118]. Here we propose to switch skyrmions in 2D thin films using the STT induced by the spin polarized current from a magnetic electrode. The device setup is schematically shown in Fig. 5.2 (a). A charged current is injected vertically from a hard magnetic nanopillar, and the spin of the current is thus polarized along the magnetization. A spin-less copper layer is deposited between the helimagnetic layer and the magnetic electrode to decouple the inter-layer exchange. The sandwich structure is on the top of a back contact layer which serves as the drain of the electron current. In order to quantitatively evaluate the required condition and to estimate the feasibility of this switching mechanism, dynamical simulations of the spin system based on the Landau-Lifshitz-Gilbert (LLG) equation are performed. The equation of motion is given by

$$\dot{\mathbf{S}} = -\gamma \mathbf{S} \times \mathbf{H}_{\text{eff}} + \alpha \mathbf{S} \times \dot{\mathbf{S}} + \boldsymbol{\tau}_{\text{STT}} \tag{5.6}$$

where $\gamma = g/\hbar$ is the gyromagnetic ratio and α is the Gilbert damping coefficient. $\mathbf{H}_{\text{eff}}$ is the effective field given by $\mathbf{H}_{\text{eff}} = -\partial H/\partial \mathbf{S}$. A fourth order Runge-Kutta algorithm is employed to integrate this first order differential equation. In this simulation, material parameters of FeGe are applied, such that $J = aA_0$ and $D = a^2 D_0$, where $a = 2.3\,\text{nm}$ is the choice of the mesh grid size, $A_0 = 5.33\,\text{meVÅ}^{-1}$ is the exchange stiffness and $D_0 = 0.305\,\text{meVÅ}^{-2}$ is the DM interaction density. These parameters are chosen for a 50×50 mesh of square lattice, where the helical state period matches with the experimental observation $\lambda = 2\pi a/\arctan\left(D/\sqrt{2}J\right) = 70\,\text{nm}$. $M_s = 10^5\,\text{Am}^{-1}$ is the saturation magnetization, and t is the film thickness. The external Oersted field, B_{Ost}, includes the applied background field and the Oersted field given by the injected current. The STT term is written as

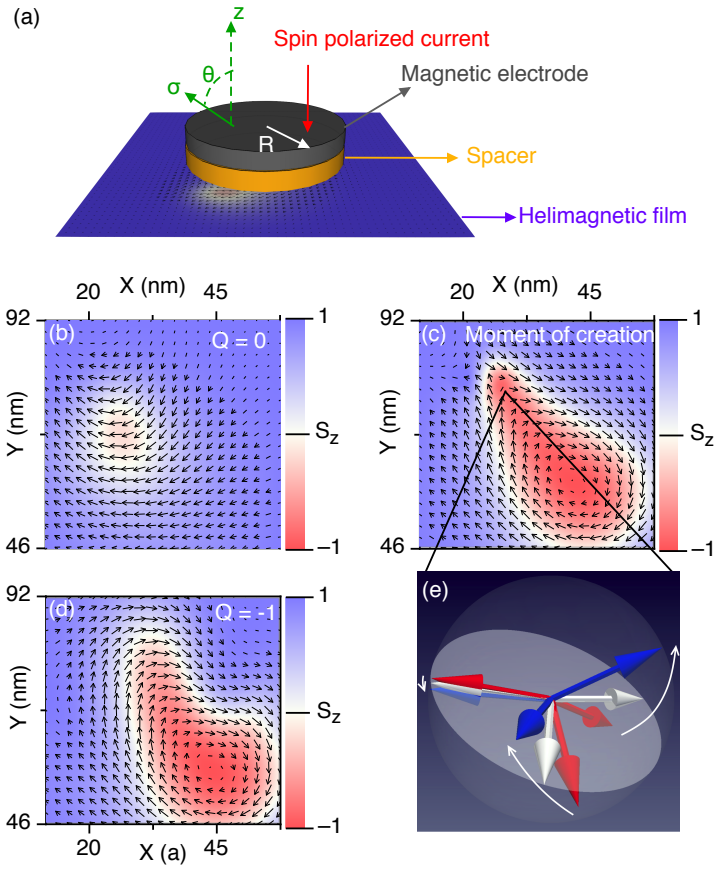

Figure 5.2:
(color online) (a) The sandwich structure of the proposed skyrmion creation scheme. θ is the angle between the injected spin, $\boldsymbol{\sigma}$, and the z axis. (b), (c) and (d) are the snap shots several picoseconds around the moment of the topological transition in a Bloch-type helimagnet thin film. (e) demonstrates the spin trajectories of the local topological transition. The red and blue arrows denote the configuration before and after the transition, respectively. A co-planner and non-collinear configuration is achieved exactly at the birth moment of the skyrmion (white arrows).

$\tau_{\mathrm{STT}} = -j\frac{\gamma\hbar p}{2eM_s t}[\mathbf{S}\times(\mathbf{S}\times\boldsymbol{\sigma})]$, where $p = 0.4$ is the polarization rate, j is the current density and $\boldsymbol{\sigma}$ is the injected spin orientation.

The LLG simulation demonstrates the possibility to create a skyrmion from a ferromagnetic (FM) state, using the STT induced spin dynamics. Starting from a ferromagnetic (FM) initial state, a DC vertical current is turned on at $t = 0$, and the topological charge evolution is monitored during the spin dynamical processes afterwards. A background field is applied along the $\hat{z}$ direction, perpendicular to the thin film, such that the energy of a FM state matches the energy of a single skyrmion. After the current is turned on, the STT and the Oersted field drive the spins into the x-y plane near the electrode, forming a pack of spin wave. Since spins at the boundary of this pack diviates from the outside FM configuration, the DM interaction starts to increase. This drives the spin texture to form a bubble-like domain, in which the center spins present negative z components, while the spins at the periphery give large in-plane components. The bubble-like domain then continues to enlarge, and start to wrap into a circular domain wall with a singularity. Around the singularity the spins gradually develop into an anti-parallel configuration, which then generate a quick, drastic dynamical process that creates a topological charge of -1. Snap shots of the spin texture several picoseconds around the transition critical moment are extracted from the simulation, as presented in Fig. 5.2. The spin trajectories corresponding to the local topological transition is shown in Fig. 5.2 (e), which follows the co-planner and non-collinear configuration discussed in the previous section.

The critical current density to trigger the skyrmion creation event is evaluated through a series of LLG simulations. Starting from a low enough current density, the initial excitations damp away very fast, such that no topological charge can be created. The creation of skyrmions occurs when the current density overcomes a critical value, j_C. The phase diagram of j_C as a function of the spin polarization angle, θ, and the electrode radius, R, is demonstrated in Fig. 5.2. R varies from 11.5 nm to 25.3 nm, while the polarization of the injected current is modified from $-\hat{z}$ to the x-y plane ($90^\circ < \theta < 180^\circ$). In this

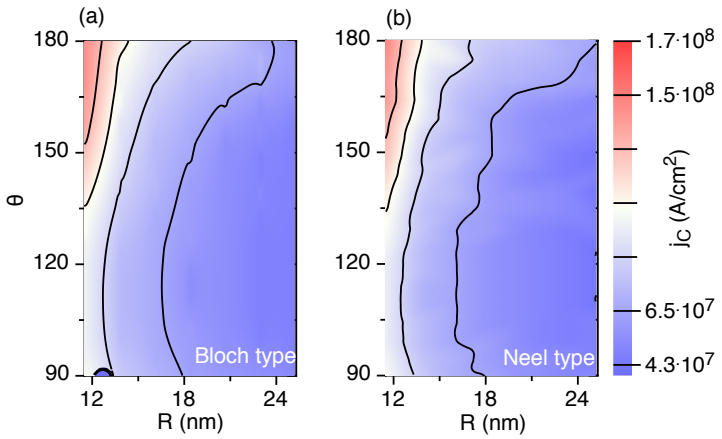

Figure 5.3:
The phase diagram of j_C for the Bloch-type (a) and the Neel-type (b) skyrmions.

calculation, both the Neel-type and the Bloch-type skyrmion creations are examined using the same set of parameters. Despite the differences in the spin dynamical details, the phase diagrams for the two types of skyrmions are quite similar. The minimum current density occurs at $\theta \sim 110°$, where the polarization is close to the in-plane case. For both skyrmion types, the j_C is roughly at the level of 10^8 A/cm^2, which is similar to the critical switching current density due to spin orbit torques estimated by previous numerical estimations. This value also matches the experimental observations in the Fe/Ir interface. Increasing the radius of the electrode can decrease the current density by several factors, but cannot bring orders-of-magnitude improvements. Although this level of current density is accessible in some cases in experiments, the j_C is two orders of magnitudes larger than the current density regularly applied in integrated circuits.

The difficulty of the skyrmion switching originates from the critical configuration required by the topological transition. The energy landscapes several picoseconds around the moment of the switching are demonstrated in Fig. 5.4 (a)-(c). Exactly at the transition moment, energy is highly concentrated at switching position, where the energy density overcomes the minimum topological energy barrier, J. For both the Neel-type and the Bloch-type skyrmion switching, the maximum energy density evolves through time, which

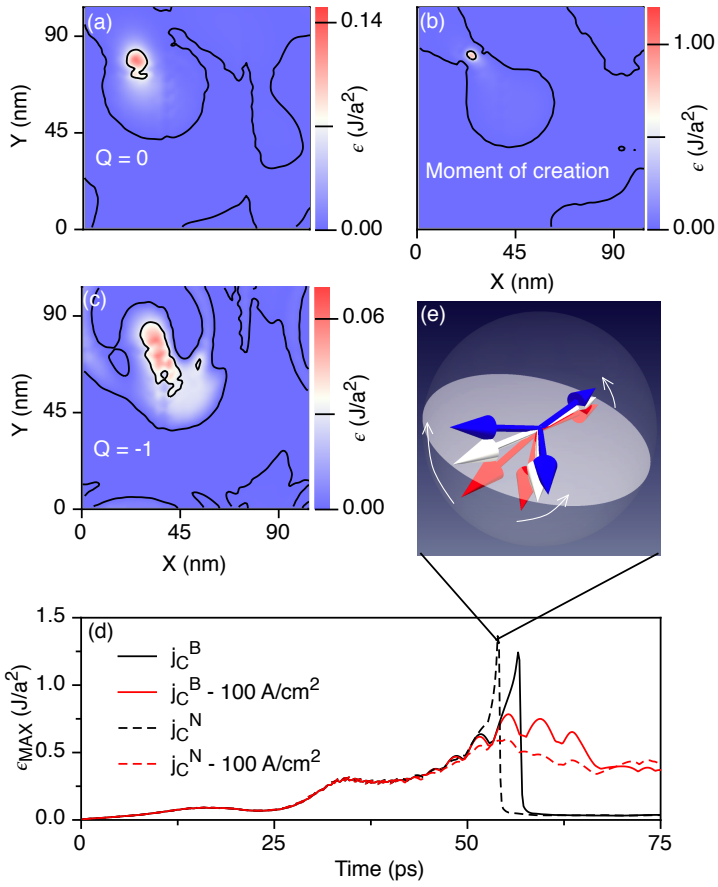

Figure 5.4:
The energy landscape of the topological transition. (a), (b) and (c) illustrate the energy density distribution of a Bloch-type skyrmion creation process. These plots correspond to the snap shots given in Fig. 5.2 (b), (c) and (d). (d) demonstrates the time evolution of the energy density maximum value for both types of skyrmions. (e) illustrates the critical configuration when a Neel-type skyrmion is created.

is illustrated in Fig. 5.4(d). When the injected current density is $100\,\mathrm{Acm}^{-2}$ below j_C, the energy density cannot overcome the topological barrier, such that no skyrmion can be created. Both of the two cases present similar line shapes of the energy evolution, despite the significant differences in the dynamical details. In both cases, fast skyrmion switching within $\sim 60\,\mathrm{ps}$ is achieved. The barrier height of the Neel type is a little larger than that of the Bloch type, which is determined by the exact switching configuration. As shown in Fig. 5.4(e), the spin alignment is more non-collinear compared to that given in Fig. 5.2 (e), contributing more exchange energy than that of the Bloch type. The difference in this configuration comes from the swirling Oersted field induced by the vertical current. For the Bloch-type skyrmions, the Oersted field helps the in-plane DM interaction form the co-planner texture, while it does not assist the out-of-plane DM interaction in the Neel-type skyrmions. As shown in the phase diagram, this difference in the barrier does not significantly affect the switching current density.

5.4 Feasibility and reliability analysis

Although single skyrmion switchings are difficult due to the topological protection, the required current density can be reduced by roughly an order of magnitude due to the easy-plane type uni-axial anisotropy. This anisotropy is written in the Hamiltonian as $H_{\mathrm{ansi}} = \sum_i KV\left(S_z^i\right)^2$ where K is the anisotropy energy density and V is the volume of each local spin. This term is physically induced by a combination of the strained structural effects at the interface and the demagnetization effects due to the aspect ratio. In a helimagnet, it has been proposed that K is measured by K_0, the effective stiffness of the conical phase determined by material parameters (for FeGe, $K_0 = 1.7 \times 10^3\,\mathrm{J/m}^3$). Recent experimental results indicate that the skyrmion phase in a FeGe thin film can be significantly extended in the phase diagram, and the value of K/K_0 reaches ~ 1 when the thickness reduces to $5\,\mathrm{nm}$. Larger values of anisotropy are expected if the thickness further decreases. Since the anisotropy energetically prefers the in-plane configuration, it helps the spin transfer torque

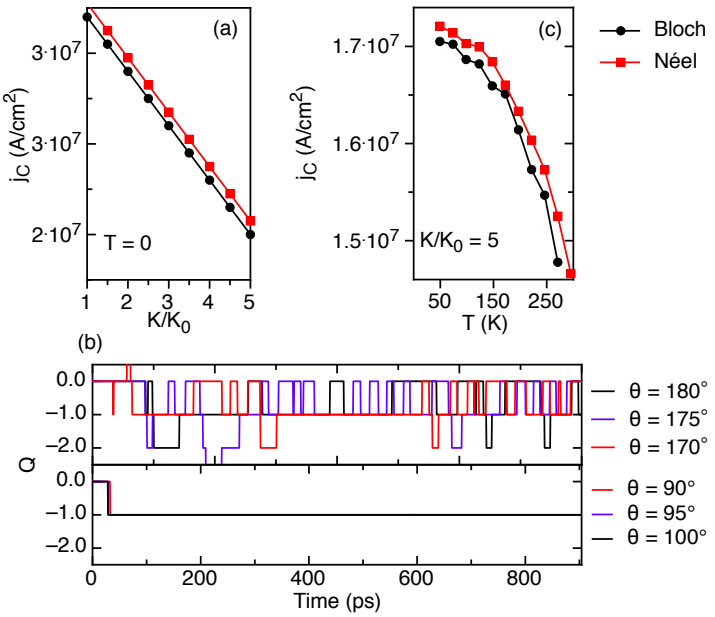

Figure 5.5:
(a) The reduction of j_C at different values of K. (b) The evolution of Q at different polarization angles. (c) The heat assisted skyrmion creation at finite temperatures. Each point is an average over 400 different sampling runs.

to drive the spins to reach the co-plannar switching configuration. The required current density can thus be reduced. Starting from the optimum situation in the phase diagram ($\theta = 110°$, $R = 25.3\,\mathrm{nm}$), the value of K/K_0 is modified from 1 to 5 in our calculation. As shown in Fig. 5.5 (a), the easy-plane anisotropy reduces the switching current density from $\sim 10^8\,\mathrm{A/cm^2}$ to $\sim 4 \times 10^7\,\mathrm{A/cm^2}$ for both types of skyrmions.

The reliability and the dynamical details of the switching process significantly depends on θ, the orientation of the spin polarization. It is well known that the STT can generate an 'anti-damping' effect during the precession of the local magnetic moment when the injected spin is anti-parallel to the precession axis [119]. The anti-damping can either induce a consistent oscillation or even the switching of a single-domain nanomagnet. This is similar to the switching of a single skyrmion in our proposed scheme. In the case of $\theta < 90°$, the excitations first induced by the torque damp away quickly, such that no

topological transition can be detected with a reasonable current density. In the case of $90^\circ < \theta < 180^\circ$, switching is always possible. Since the STT is given by $\mathbf{S} \times (\mathbf{S} \times \boldsymbol{\sigma})$, the maximum value of the torque at $t = 0$ occurs when $\theta = 90^\circ$. The torque becomes zero in the case of $\theta \to 180^\circ$, where the required current density reaches its maximum in the phase diagram. In the case of a large θ, the dynamical effect continues after the skyrmion is created, where the oscillation of the topological charge occurs. The time evolution of the topological charge is presented in Fig. 5.5 (b), in which several different angles are examined close to $\theta = 90^\circ$ and $\theta = 180^\circ$. Within 800 ps, topological charges (sometimes more than 1) quickly switch on and off in the case of $\theta \sim 180^\circ$ due to the constant oscillations driven by the STT. The outcome of the process is sensitive to the duration of the applied current and the details of the geometry, which should be avoided for application purposes. Similar effects are also observed in Fe/Ir thin films where a vertical current is injected from a vertically polarized magnetic STM tip. On the other hand, the topological charge becomes stable after the first creation in the case of the in-plane polarization. The switching can occur in ~ 60 ps, after which no further excitations can be initiated and the created skyrmion is thus stabilized. Small changes in the angle does not strongly affect the switching outcome, indicating the in-plane polarization suits better for device applications.

The stability of the proposed switching scheme is further examined at finite temperatures. In order to include this effect, a stochastic field $\mathbf{L}$ is added onto the effective field in Eq. 5.6 [120]. The dissipation-fluctuation relation $\langle L_\mu(\mathbf{r}, t) L_\nu(\mathbf{r}', t') \rangle = \xi \delta_{\mu\nu} \delta_{\mathbf{r}\mathbf{r}'} \delta_{tt'}$ is satisfied, where $\xi = \alpha k_\mathrm{B} T/\gamma$, and T is the temperature. The average $\langle\,\rangle$ is taken over the realizations of the fluctuation field. The deterministic Heun scheme is employed to integrate out this stochastic LLG equation. Below T_C (270 K in FeGe), the average switching current density based on 400 sampling runs are obtained for both the Neel-type and the Bloch-type skyrmions. The results are demonstrated in Fig. 5.5 (c). Although thermal fluctuations randomize the local spins at each time step, the overall dynamical process of the skyrmion creation is similar to that at the zero temperature. This demonstrates the stability of the skyrmion creation scheme below T_C. The average switching current density decreases due

to the thermal fluctuations, indicating a negligible heat assisted switching effect. Above T_C, although the switching current can be further reduced, the magnetic order start to vanish, where random topological charges can be spontaneously excited by thermal fluctuations. This should be avoided in the proposed switching scheme.

Chapter 6

Impedance perturbation theory of coupled transmission lines

6.1 Introduction

With the fast increase in the computation speed of modern electronic devices, the data rate of high-speed systems has been increased to the level of $\sim 56\,\mathrm{Gb/s}$, where the wave nature of the signal propagation in the interconnects has to be considered [35]. Derived from the Maxwell equations, transmission line models using lumped parameters (RLGC: resistance-inductance-conductance-capacitance) capture the wave effects of signal propagation, and have been widely applied to describe high-speed interconnects [121]. Although the accuracy of these models cannot reach the level of finite-element simulations, the lumped models are numerically more efficient and easy to implement in circuit simulators such as SPICE or ASTAP. More importantly, they can usually provide important insights in the physical nature of the signal propagation, which is exceptionally important in qualitative estimations. Therefore, in the design of high-speed systems and the analysis of signal integrity, the lumped model of transmission lines are widely used.

Although the complexity of the problem has been simplified by using the lumped models, the relation between the lumped parameters and the network matrices is still com-

plicated. Different effects such as delay, reflection, crosstalk and attenuation are usually intricately implied within all the modeling parameters. To further understand the effects of these parameters, neglecting the high-order perturbations given by small modifications is usually useful. This kind of perturbation analysis has been carried out to describe the inhomogeneous effects in transmission lines [122] and the inter-trace couplings in multi-conductor transmission lines [123]. Motivated by the fact that transmission lines are often closely matched to a reference impedance, in this chapter we take the impedance mismatch as a small quantity, and propose a generic impedance perturbation theory based on the lumped parameters. The propagation constants, S-parameters and T-parameters for both the single-ended and coupled transmission lines are investigated at the impedance perturbation limit.

This chapter is arranged as follows: in Sec. II, we introduce the formulation of the perturbation theory for single-ended transmission lines. In Sec. III, the application of the perturbation model in differential transmission lines is described in detail. The numerical accuracy of the perturbation model is also evaluated. In Sec. IV, as another application example, we evaluate the TRL de-embedding fluctuation by applying the perturbation theory and the corresponding measurement verifications. We conclude our results in Sec. V.

6.2 Formulations and calculation details

6.2.1 Impedance Perturbation Model for Single-ended Transmission Lines

The impedance perturbation theory starts with a closed form model for a lossy single-mode transmission line. The ABCD matrix is given as follows:

$$\mathbf{ABCD} = \begin{bmatrix} \cosh(\gamma l) & Z_c \sinh(\gamma l) \\ \frac{\sinh(\gamma l)}{Z_c} & \cosh(\gamma l) \end{bmatrix}, \tag{6.1}$$

where γ is the complex propagation constant, l is the distance between the reference planes and Z_c is the characteristic impedance. These parameters are determined by a causal RLGC model for 2-port uniform transmission lines [36, 124]. According to the conversion between ABCD parameters and S-parameters [125], the scattering matrix of the transmission line can be given as follows:

$$\mathbf{S} = \begin{bmatrix} S_{11} & S_{12} \\ S_{21} & S_{22} \end{bmatrix}, \tag{6.2}$$

where

$$\begin{cases} S_{12} = S_{21} = \frac{2}{2\cosh(\gamma l) + (\frac{Z_c}{Z_0} + \frac{Z_0}{Z_c})\sinh(\gamma l)} \\ S_{11} = S_{22} = \frac{(\frac{Z_c}{Z_0} - \frac{Z_0}{Z_c})\sinh(\gamma l)}{2\cosh(\gamma l) + (\frac{Z_c}{Z_0} + \frac{Z_0}{Z_c})\sinh(\gamma l)} \end{cases}, \tag{6.3}$$

and Z_0 is the reference impedance (usually $50\,\Omega$). Assuming the transmission line is close to the perfect matching condition ($Z_0 \approx Z_c$), we have

$$\frac{Z_0}{Z_c} = 1 - \xi \tag{6.4}$$

where ξ is a dimensionless quantity close to zero that can be taken as a perturbation term. In order to analytically investigate the effects of any small impedance mismatch, here we calculate the first-order influence of ξ in the S-parameter matrix elements. Using the Taylor series of $\frac{1}{1-x} = 1 + x + x^2 + x^3 + \cdots$ for $|x| < 1$, the return-loss and the insertion-loss can be simplified as follows with ξ being kept to the first order:

$$\begin{aligned} S_{11} &= \frac{(1 + \xi + \xi^2 + \cdots - 1 + \xi)\sinh(\gamma l)}{2\cosh(\gamma l) + (2 + \xi^2 + \cdots)\sinh(\gamma l)} \\ &\approx \frac{\xi \sinh(\gamma l)}{e^{\gamma l}} \end{aligned} \tag{6.5}$$

$$\begin{aligned} S_{12} &= \frac{2}{2\cosh(\gamma l) + (2 + \xi^2 + \cdots)\sinh(\gamma l)} \\ &\approx e^{-\gamma l}, \end{aligned} \tag{6.6}$$

such that

$$\mathbf{S} = \begin{bmatrix} \frac{\xi \sinh(\gamma l)}{e^{\gamma l}} & e^{-\gamma l} \\ e^{-\gamma l} & \frac{\xi \sinh(\gamma l)}{e^{\gamma l}} \end{bmatrix}. \tag{6.7}$$

Similarly, the T-parameters can be given from the ABCD matrix [125, 126]. According to (6.1), the T-parameter matrix can be simplified by keeping ξ to the first order:

$$\mathbf{T} = \begin{bmatrix} T_{11} & T_{12} \\ T_{21} & T_{22} \end{bmatrix} \approx \begin{bmatrix} e^{-\gamma l} & \xi \sinh(\gamma l) \\ -\xi \sinh(\gamma l) & e^{\gamma l} \end{bmatrix}. \tag{6.8}$$

Note that the simplified parameters follow the following **S**-**T** conversion relation:

$$\begin{cases} T_{11} = \frac{1}{S_{21}}; & T_{12} = \frac{S_{11}}{S_{21}}; \\ T_{21} = -\frac{S_{22}}{S_{21}}; & T_{22} = \frac{S_{12}S_{21} - S_{11}S_{22}}{S_{21}}; \end{cases} \tag{6.9}$$

Observing (6.7) and (6.8), the impedance mismatch mainly affects the return-loss terms in the S-parameter matrix, while insertion-loss is not affected by the first-order perturbation. In the perfect matching situation, $\xi \to 0$, and the return-loss terms in the S-parameters reduce to zero. In the T-parameter matrix, the perturbation factor introduces small off-diagonal elements. At the perfect matching limit, the T-parameter matrix becomes diagonal.

6.2.2 Impedance Renormalization in The T-parameter Matrix

S-parameters and T-parameters are defined with a given reference impedance, Z_0. Usually the reference impedance is taken as $50\,\Omega$, but discrepancies in Z_0 can occur for many reasons such as a TRL de-embedding [40, 41] or multi-port system measurements [127]. In the case of cascading sub-networks, the reference impedance of each sub-network requires to be normalized to the same value. Methods to renormalize S-parameters have been proposed and widely applied [127, 128]. Here, we use the first-order impedance perturbation theory to analyze the effect of the impedance renormalization in the T-parameters.

At the impedance perturbation limit, a reference impedance renormalization corresponds to a change in the mismatch factor, ξ. For the T-parameters, a non-zero ξ gives small off-diagonal elements in the matrix. Now we try to diagonalize the T-parameter matrix as follows:

$$\mathbf{T}' = \begin{bmatrix} \lambda^- & 0 \\ 0 & \lambda^+ \end{bmatrix} = \mathbf{D}^{-1}\mathbf{T}\mathbf{D} \tag{6.10}$$

where $\lambda^{\pm}$ are the eigenvalues of $\mathbf{T}$ given by (6.8). According to (6.8), the eigenvalues can be obtained analytically:

$$\lambda^{\pm} = \cosh(\gamma l) \pm \sinh(\gamma l)\sqrt{1+\xi^2} \approx e^{\pm\gamma l}. \tag{6.11}$$

Note that the estimation given in (6.11) is equal to the result given by (6.8) in the case of perfect matching. The linear transformation matrix, $\mathbf{D}$, is given as

$$D = C \begin{bmatrix} 1 & \frac{\xi}{2} \\ \frac{\xi}{2} & 1 \end{bmatrix} \tag{6.12}$$

where C is an artificial coefficient. Thus, given the complex propagation coefficient (γ) of a uniform transmission line, the T-parameter matrix can be renormalized to different 'close-to-match' reference impedance using the inverse linear transformation

$$\mathbf{T} = \mathbf{D}\mathbf{T}'\mathbf{D}^{-1}. \tag{6.13}$$

Since the characteristic impedance of a transmission line is usually frequency dependent, the value of ξ and the transformation matrix, $\mathbf{D}$, should also be frequency dependent. However, for many applications in high-speed interconnects, most of the signal loss occurs at high frequencies ($f > 10\,\text{GHz}$), where the frequency-dependent characteristic impedance converges to a static value. Furthermore, the expressions of the perturbation model do not

Figure 6.1: Port numbering for a typical differential pair used in high-speed systems.

change with the frequency dependency of the perturbation factor, ξ. Thus, in this chapter we neglect the frequency dependency of ξ for simplicity.

6.3 Application #1: The perturbation model for differential striplines.

6.3.1 Nodal and modal S(T)-parameters.

Previous discussions in the impedance perturbation theory are based on the single-mode transmission lines. In this section we demonstrate the application of the perturbation theory in the case of differential striplines. According to the generic theory [129], in multi-conductor transmission lines, each fundamental mode propagates independently without coupling to others. These fundamental modes form linearly independent subspaces, such that each mode can be treated as if they were decoupled single-ended lines. The port numbering of the differential stripline is illustrated in Fig. 6.1 with port 1 and port 2 as the input. For such a network, there are two representations to describe the scattering matrix: single-ended (nodal) and mixed-mode (modal). Single-ended representation treats the coupled pair as a regular 4-port network, which directly follows the definition of the

scattering matrix. The S-parameter of a 4-port differential pair can be written as

$$\mathbf{S} = \begin{bmatrix} \begin{bmatrix} S_{11} & S_{12} \\ S_{21} & S_{22} \end{bmatrix} & \begin{bmatrix} S_{13} & S_{14} \\ S_{23} & S_{24} \end{bmatrix} \\ \begin{bmatrix} S_{31} & S_{32} \\ S_{41} & S_{42} \end{bmatrix} & \begin{bmatrix} S_{33} & S_{34} \\ S_{43} & S_{44} \end{bmatrix} \end{bmatrix} = \begin{bmatrix} \mathbf{S}_{11} & \mathbf{S}_{12} \\ \mathbf{S}_{21} & \mathbf{S}_{22} \end{bmatrix}, \tag{6.14}$$

where $\mathbf{S}_{j,k}$ $(j,k = 1,2)$ are 2×2 sub-matrices. This S-parameter matrix inter-transfers with its corresponding generalized transfer matrix, $\mathbf{T}$, as

$$\mathbf{T} = \begin{bmatrix} \mathbf{S}_{12} - \mathbf{S}_{11}\mathbf{S}_{21}^{-1}\mathbf{S}_{22}, & \mathbf{S}_{11}\mathbf{S}_{21}^{-1} \\ -\mathbf{S}_{21}^{-1}\mathbf{S}_{22}, & \mathbf{S}_{21}^{-1} \end{bmatrix}, \tag{6.15}$$

$$\mathbf{S} = \begin{bmatrix} \mathbf{T}_{12}\mathbf{T}_{22}^{-1}, & \mathbf{T}_{11} - \mathbf{T}_{12}\mathbf{T}_{22}^{-1}\mathbf{T}_{21} \\ \mathbf{T}_{22}^{-1} & -\mathbf{T}_{22}^{-1}\mathbf{T}_{21} \end{bmatrix} \tag{6.16}$$

which is a generalization of the well-known 2-port-network **S**-**T** relation given in (6.9) [41, 125, 130, 131].

A mixed-mode S-parameter matrix, however, treats the 4-port network as two independent propagation modes that are de-coupled from each other. In general, the two independent modes are the c mode and the π mode [132]. If the two traces are identical, these two modes reduce to an even mode and an odd mode, respectively. The nodal S-parameters can be given as follows [37, 131, 133]:

$$\mathbf{S}_n = \mathbf{M}_T \mathbf{S}_m \mathbf{M}_T^{-1} \tag{6.17}$$

where the transformation matrix is written as:

$$\mathbf{M}_T = \frac{1}{\sqrt{2}} \begin{bmatrix} -1 & 1 & 0 & 0 \\ 1 & 1 & 0 & 0 \\ 0 & 0 & -1 & 1 \\ 0 & 0 & 1 & 1 \end{bmatrix}. \tag{6.18}$$

Applying the inverse transformation given by (6.17), the modal S-parameter matrix of a differential transmission line is given as

$$\mathbf{S}_m = \begin{bmatrix} S_{11}^e & 0 & S_{13}^e & 0 \\ 0 & S_{22}^o & 0 & S_{24}^o \\ S_{31}^e & 0 & S_{33}^e & 0 \\ 0 & S_{42}^o & 0 & S_{44}^o \end{bmatrix} \tag{6.19}$$

where the de-coupled fundamental modes can be written in 2×2 matrices separately as

$$\mathbf{S}_m^e = \begin{bmatrix} S_{11}^e & S_{13}^e \\ S_{31}^e & S_{33}^e \end{bmatrix} \tag{6.20}$$

and

$$\mathbf{S}_m^o = \begin{bmatrix} S_{22}^o & S_{24}^o \\ S_{42}^o & S_{44}^o \end{bmatrix}. \tag{6.21}$$

Applying the impedance perturbation theory in each mode, the total modal S-parameter matrix is given as:

$$\mathbf{S}_m \approx \begin{bmatrix} \frac{\xi_e \sinh(\gamma_e l)}{e^{\gamma_e l}} & 0 & e^{-\gamma_e l} & 0 \\ 0 & \frac{\xi_o \sinh(\gamma_o l)}{e^{\gamma_e l}} & 0 & e^{-\gamma_o l} \\ e^{-\gamma_e l} & 0 & \frac{\xi_e \sinh(\gamma_e l)}{e^{\gamma_o l}} & 0 \\ 0 & e^{-\gamma_o l} & 0 & \frac{\xi_o \sinh(\gamma_o l)}{e^{\gamma_o l}} \end{bmatrix} \tag{6.22}$$

where

$$\frac{Z_0}{Z_{c,i}} = 1 - \xi_i, \tag{6.23}$$

where $i = e, o$. The corresponding T-parameter matrix can be calculated using (6.15) as

$$\mathbf{T}_m = \begin{bmatrix} e^{-\gamma_e l} & 0 & \xi_e \sinh(\gamma_e l) & 0 \\ 0 & e^{-\gamma_o l} & 0 & \xi_o \sinh(\gamma_o l) \\ -\xi_e \sinh(\gamma_e l) & 0 & e^{\gamma_e l} & 0 \\ 0 & -\xi_o \sinh(\gamma_o l) & 0 & e^{\gamma_o l} \end{bmatrix}. \tag{6.24}$$

Diagonalizing this matrix, we have:

$$\mathbf{T}'_m = \mathbf{D}_m^{-1} \mathbf{T} \mathbf{D}_m, \tag{6.25}$$

where

$$\mathbf{D}_m = \begin{bmatrix} C_e & 0 & C_e \frac{\xi_e}{2} & 0 \\ 0 & C_o & 0 & C_o \frac{\xi_o}{2} \\ C_e \frac{\xi_e}{2} & 0 & C_e & 0 \\ 0 & C_o \frac{\xi_o}{2} & 0 & C_o \end{bmatrix}, \tag{6.26}$$

and C_e and C_o are artificial coefficients. Similar to the single-ended case, the diagonalized T-parameter matrix contains the information of the propagation constant:

$$\mathbf{T}'_m \approx \mathrm{diag}\{e^{-\gamma_e l}, e^{-\gamma_o l}, e^{\gamma_e l}, e^{\gamma_o l}\}, \tag{6.27}$$

which corresponds to the perfect impedance matching situation in each mode. Due to the intra-pair coupling, $\xi_e \neq \xi_o$, and it is required to renormalize the T-parameter matrix to a designated reference impedance. This can be achieved by an inverse linear transformation that is similar to the single-mode case as follows:

$$\mathbf{T}_m = \mathbf{D}_m \mathbf{T}'_m \mathbf{D}_m^{-1}. \tag{6.28}$$

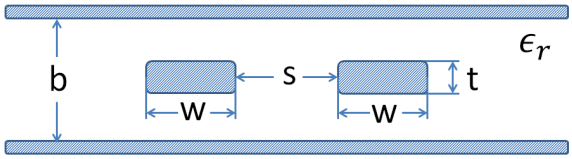

Figure 6.2:
The geometry parameters for a coupled pair of striplines. The parameters demonstrated in the figure are used to determine the characteristic impedance.

6.3.2 Impedance Perturbation Analysis of The Propagation Constants

In this subsection, we apply the impedance perturbation theory to analyze the propagation constant of each mode of a coupled pair of striplines. To quantitatively obtain the perturbation factor, ξ_i, we first calculate the characteristic impedance, $Z_{c,i}$, based on the choice of material and the design geometry. This can be obtained by conformal mapping [134]. The general impedance expressions for symmetrically coupled striplines are listed as follows.

$$\begin{cases} Z_{c,i} = \frac{30\pi(b-t)}{\sqrt{\epsilon_r}\left(W+\frac{bC_f}{2\pi}A_i\right)} \\ A_e = 1 + \frac{\ln[1+\tanh(\theta)]}{\ln 2} \\ A_o = 1 + \frac{\ln\left[1+\frac{1}{\tanh(\theta)}\right]}{\ln 2} \\ \theta = \frac{\pi S}{2b} \\ C_f\left(\frac{t}{b}\right) = 2\ln\left(\frac{2b-t}{b-t}\right) - \frac{t}{b}\ln\left[\frac{t(2b-t)}{(b-t)^2}\right] \end{cases} \tag{6.29}$$

The corresponding design parameters are demonstrated in Fig. 6.2.

The propagation constant is calculated using a causal transmission line model [36,124], where the RLGC values are frequency dependent. For the purpose of completeness, we list the important expressions in this model as follows. In mode i ($i = e, o$), we have $\gamma_i(\omega) = \sqrt{\left(\hat{R}_i + j\omega\hat{L}_i\right)\left(\hat{G}_i + j\omega\hat{C}_i\right)}$. The modified RLGC parameters are given as:

$$\begin{cases} \hat{R}_i = R_{\rm dc} + R_{\rm surf}\sqrt{\omega}; & \hat{G}_i = \omega K C_i \\ \hat{L}_i = L_i + \frac{R_{\rm surf}}{\sqrt{\omega}}; & \hat{C}_i = PC_i \end{cases}, \tag{6.30}$$

where C_i and L_i are obtained from the static (high-frequency) characteristic impedance, $Z_{c,i}$ [from (6.29)].

$$C_i = \frac{\sqrt{\mu_0 \epsilon_0 \epsilon_r}}{Z_{c,i}} \tag{6.31}$$

$$L_i = Z_{c,i} \sqrt{\mu_0 \epsilon_0 \epsilon_r}. \tag{6.32}$$

μ_0 and ϵ_0 are the permeability and permittivity of vacuum, and ϵ_r is relative permittivity of the dielectric material. The metallic loss is introduced by $\hat{R}_i$, where $R_{\text{dc}} = \frac{\rho}{Wt}$ is the DC resistance per unit length determined by the resistance of the material (ρ) and the geometry parameters (W, t). The frequency-dependent surface resistance R_{surf} is introduced by the skin effect.

$$R_{\text{surf}} = \frac{R_{\text{dc}} \cdot G_p}{\sqrt{2\pi f_{\text{surf}}}} \tag{6.33}$$

where $f_{\text{surf}} = \frac{4\rho}{t^2 \pi \mu_0}$ is the skin-effect onset frequency at small thickness limit ($W \gg t$) [135]. G_p in (6.33) is a factor that introduces the conductor loss contributed by the current in the ground plane. The dielectric loss at high frequency is described by the frequency-dependent $\hat{G}_i$ and $\hat{C}_i$ in (6.30), where

$$K = -\frac{\epsilon_r''}{\epsilon_r}; \quad P = \frac{\epsilon_r'}{\epsilon_r} \ , \tag{6.34}$$

in which ϵ_r' and ϵ_r'' are the frequency-dependent parts of the dielectric constant:

$$\begin{cases} \epsilon_r'(\omega) = \epsilon_r + \frac{A}{2} \ln\left[\frac{\tau_2^2\left(1+\omega^2\tau_1^2\right)}{\tau_1^2\left(1+\omega^2\tau_2^2\right)}\right] \\ \epsilon_r''(\omega) = A\left[\arctan(\omega\tau_1) - \arctan(\omega\tau_2)\right]. \end{cases} \tag{6.35}$$

Here, A is the strength of the dielectric loss, and $\tau_{1,2}$ gives the starting and ending points of the relaxation time distribution [136]. Table 6.1 lists all the parameters applied in our numerical simulation. The values of these parameters do not correspond to a particular design, but are randomly chosen based on empirical values for the purpose of our demonstration.

The frequency dependency of the propagation constant (dispersion) is a crucial relation that determines the EM wave behavior of each fundamental mode of a coupled

Table 6.1: Parameters for the toy models used in this chapter.

Parameters	Value
ϵ_r	3.8
ϵ_0	$8.854 \times 10^{-12}\,\mathrm{F/m}$
μ_0	$4\pi \times 10^{-7}\,\mathrm{H/m}$
A	0.019
τ_1	1.6 ps
τ_2	1.6 ms
G_p	1.5
ρ	$1.764 \times 10^{-8}\,\Omega\mathrm{m}$

transmission line. Here, we analytically evaluate the effect of the impedance mismatch perturbation, ξ_i, on the propagation constant of each fundamental mode: $\gamma_i(\omega) = \alpha_i(\omega) + j\beta_i(\omega)$. In general, the attenuation (α) and phase (β) constant of each mode is given as:

$$\begin{cases} \alpha_i^2 - \beta_i^2 = \hat{R}_i\hat{G}_i - \omega^2\hat{L}_i\hat{C}_i \\ 2\alpha_i\beta_i = \omega\left(\hat{L}_i\hat{R}_i + \hat{C}_i\hat{G}_i\right) \end{cases}. \tag{6.36}$$

Considering $\hat{R}_i$ and $\hat{G}_i$ as small quantities, one can get

$$\beta_i^2 \approx \omega^2\hat{L}_i\hat{C}_i \tag{6.37}$$

Using the results given in (6.30), we have

$$\beta_i \approx \pm\omega\sqrt{\frac{\epsilon_r'}{c_0^2} + PC_i\left(\frac{R_{\mathrm{surf}}}{\sqrt{\omega}}\right)} \tag{6.38}$$

where $c_0 = 1/\sqrt{\mu_0\epsilon_0}$ is the vacuum speed of light. Given (6.31) and (6.23), the even and odd phase propagation constant splits due to the coupling:

$$\beta_i = \pm\omega\sqrt{\frac{\epsilon_r'}{c_0^2} + \frac{P\sqrt{\epsilon_r}}{c_0 Z_0}\left(\frac{R_{\mathrm{surf}}}{\sqrt{\omega}}\right)(1-\xi_i)}, \tag{6.39}$$

where $\xi_e \neq \xi_o$ due to the modal impedance splitting. Since the frequency (usually at MHz or GHz) and the speed of light are in the denominator of the second term inside the square root,

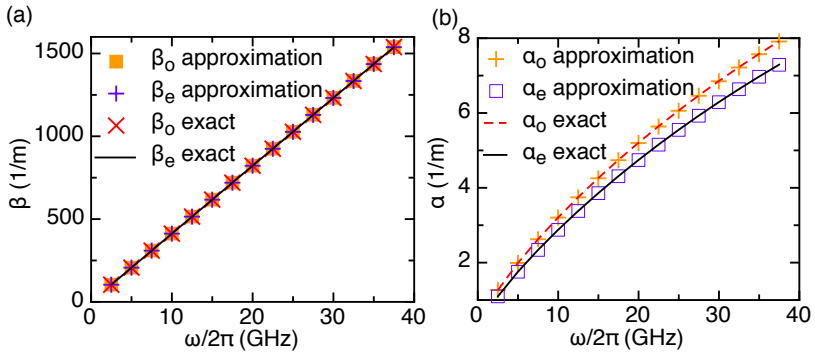

Figure 6.3:
Dispersion of EM wave for a coupled stripline. The design parameters are: $W = 127\,\mu$m, $S = 177.8\,\mu$m, $b = 395.224\,\mu$m, $t = 30.48\,\mu$m.

the splitting given by the intra-pair coupling vanishes: $\beta_e \approx \beta_o \approx \pm\frac{\omega}{c_0}\sqrt{\epsilon_r'}$. Further taking the approximation to neglect the dielectric loss ($A \to 0$), the relation becomes: $\beta_i = \pm\frac{\omega}{c_0}\sqrt{\epsilon_r}$, which is the regular light propagation constant in lossless transparent materials. Since the transmission line materials applied in high speed IC/systems are good conductors, $\frac{R_{\text{surf}}}{c_0}$ is usually close to zero, such that neglecting the second term inside the square root is often a good approximation. Fig. 6.3 (a) demonstrates the dispersion of the imaginary part of the propagation constant, in which the splitting of each fundamental mode is not significant. The approximation curve uses the relation $\beta_e = \beta_o = \pm\frac{\omega}{c_0}\sqrt{\epsilon_r'}$, while the exact β_i is obtained from imaginary part of γ_i from the causal RLGC model.

To evaluate the attenuation of a coupled transmission line, solving (6.36), we have

$$\alpha^2 = \frac{RG - \omega^2 LC}{2} \pm \frac{1}{2}\sqrt{\left(RG - \omega^2 LC\right)^2 + \omega^2\left(LG + RC\right)^2} \tag{6.40}$$

$$\alpha \approx \pm\frac{1}{2}\left(LG + RC\right)\sqrt{\frac{1}{LC}}. \tag{6.41}$$

Substituting (6.30) in (6.41), the attenuation of each mode is simplified as:

$$\alpha_i \approx \pm \left[\frac{|\epsilon_r''|\,\omega}{2c_0\sqrt{\epsilon'}} + \sqrt{\frac{\epsilon_r'}{\epsilon_r}} \frac{\sqrt{\omega}R_{\text{surf}} + R_{\text{dc}}}{2Z_0} (1 - \xi_i) \right]. \tag{6.42}$$

As denoted in (6.42), the EM wave attenuation is contributed by two parts. The first term is proportional to ω and the imaginary part of the complex dielectric constant, ϵ''. This part comes from the EM absorption of the dielectric material, which dominates the attenuation at high frequencies. The second term, on the other hand, is proportional to $(\sqrt{\omega}R_{\text{surf}} + R_{\text{dc}})$, which contains the information of the conductor loss and the skin effect. Thus, the attenuation of the two modes splits due to the modal impedance splitting ($\xi_e \neq \xi_o$), and the splitting is proportional to $\sqrt{\omega}$. The comparison between the exact attenuation and the result given by the perturbation model is presented in Fig. 6.3 (b).

6.3.3 Numerical Verification of the Differential Stripline Model Based on the Perturbation Theory

To evaluate the validity of the impedance perturbation theory in the S-parameters, we compare the exact uniform transmission line model given by (6.3) to the perturbation model defined in (6.22). Without loss of generality, different levels of the impedance mismatch are tested. As demonstrated in Fig. 6.4, when the impedance is ~35 Ω, the error of the perturbation theory is within several dBs in the return-loss magnitude, while the errors in the insertion-loss magnitude is less than 1 dB.

The oscillation features in the S-parameter magnitude can be explicitly explained by the perturbation model. Keeping the perturbation correction in (6.23) to the second order, we have

$$S_{31}^i = S_{42}^i = \frac{2}{2e^{\gamma_i l} + \xi_i^2 \sinh(\gamma_i l)} \approx e^{-\gamma_i l} - \frac{\xi_i^2 \sinh(\gamma_i l)}{2e^{2\gamma_i l}}. \tag{6.43}$$

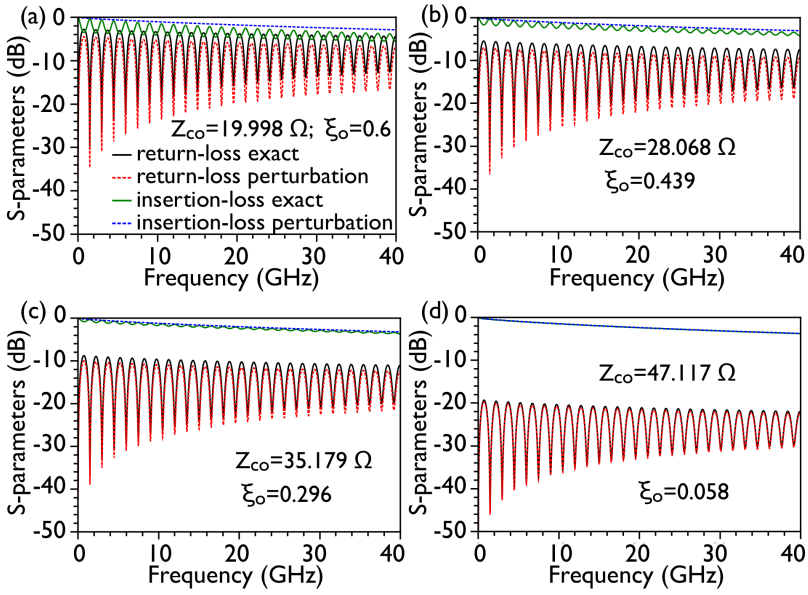

Figure 6.4:
Accuracy analysis of the perturbation theory. In this calculation, a coupled stripline is simulated. The design parameters are: $l = 50.8\,\text{mm}$, $S = 165.1\,\mu\text{m}$, $b = 395.224\,\mu\text{m}$, $\epsilon_r = 3.8$ and $t = 30.48\,\mu\text{m}$. From (a) to (d), W is modified accordingly as $W = 635\,\mu\text{m}$, $W = 381\,\mu\text{m}$, $W = 254\,\mu\text{m}$ and $W = 127\,\mu\text{m}$. The corresponding impedance Z_{co} and the perturbation term ξ_o are included in the figures.

Splitting the real and the imaginary parts of the propagation constant as $\gamma_i(f) = \alpha_i(f) + j\beta_i(f)$, the insertion-loss for each mode can be simplified as

$$20\log_{10}\left|S_{31}^{i}\right| \approx \frac{10}{\ln(10)}\left\{\frac{\xi_i^2}{2e^{2\alpha(f)_i l}}\cos\left[2l\beta_i(f)\right] - \frac{\xi_i^2}{2}\right\}. \\ -\frac{20\alpha_i(f)l}{\ln(10)} \tag{6.44}$$

Due to the linear-like relation between α_i and f at high frequencies, the last term in (6.44) gives a linear-like feature of the insertion-loss, which is reflected in the attenuation of the EM wave propagation. The first term in (6.44), on the other hand, introduces the oscillation feature whose amplitude exponentially decays with the attenuation, α_i. Thus, the magnitude of this oscillation decreases with frequency (Fig. 6.4). The maxima of this oscillation occur at $\beta_i = {}^{n\pi}/_{l_i}$ $(n = 0, 1, 2, \cdots)$. Given the phase velocity of the electromagnetic wave in the material as $v_p = \frac{c_0}{\sqrt{\epsilon_r}} = \frac{2\pi f}{\beta_i}$, where c_0 is the speed of light in vacuum, the maxima of the insertion-loss occur at $f_n = \frac{nc_0}{2l_i\sqrt{\epsilon_r}}$ $(n = 0, 1, 2, \cdots)$. Observing (6.44), the oscillating feature of the insertion-loss magnitude is determined by ξ_i to the second order. Thus, this oscillation is only important when severe mismatch occurs, which is usually avoided. As demonstrated in Fig. 6.4 the accuracy of this approximation is within 1 dB for a mismatch factor up to $\xi_i = 0.3$.

The return-loss given by the perturbation model, on the other hand, captures the oscillation features of the exact model by the first-order perturbation. Here, we take dB of the return-loss analytically as follows.

$$20\log_{10}\left|S_{11}^{i}\right| \approx \frac{10\ln\frac{\xi_i^2}{4}}{\ln(10)} \\ +\frac{10}{\ln(10)}\ln\left\{1 - e^{-2\alpha_i(f)l}2\cos\left[2l\beta_i(f)\right] + e^{-4\alpha_i(f)l}\right\} \tag{6.45}$$

At low frequencies, $\alpha_i \to 0$, and (6.45) is simplified as

$$20\log_{10}\left|S_{11}^{i}\right| \approx \frac{10\ln\frac{\xi_i^2}{4}}{\ln(10)} + \frac{10}{\ln(10)}\ln\left\{2 - 2\cos\left[2l\beta_i(f)\right]\right\}. \tag{6.46}$$

The second term describes the oscillation of the return-loss at low frequency. When $\beta_i = {}^{n\pi}/_{l_i}$ $(n = 0, 1, 2, \cdots)$, the return-loss approaches to $-\infty$. The resonance frequency occurs at $f_n = \frac{nc_0}{2l_i\sqrt{\epsilon_r}}$. At high frequencies ($> 40\,\mathrm{GHz}$) where the dielectric loss gives significant attenuation ($\alpha_i \to \infty$), the second term in (6.45) reduces, and the return-loss oscillation magnitude reduces as well.

$$20\log_{10}|\tau_i(f)| \approx \frac{20\ln\frac{|\xi_i|}{2}}{\ln(10)}, \tag{6.47}$$

which is dominated by the impedance mismatch factor.

6.4 Application #2: The Impedance Perturbation in TRL De-embedding

In order to characterize transmission line networks, S-parameter measurements using vector network analyzers (VNAs) are usually applied. Conventionally, for a 2-port VNA measurement result, one needs to follow the standard TRL (through, reflect, line) calibration procedure to de-embed the device under test (DUT) from error boxes (usually access/transition structures including contact pads and vias) [39, 121, 137, 138]. The 2-port TRL method is later generalized for the de-embedding of multimode networks [139]. The detailed analytical derivations of this method is systematically reported recently [40,41,139]. Usually, for a 2-port network calibration, the TRL procedure requires multiple line standards of quarter wavelengths to cover a wide band of frequencies [140]. A trade-off to reduce the required number of the line standards is to use the characteristic impedance of the *line* standard as the reference impedance [137]. In this case, the de-embedded results should be renormalized to a designated unified reference impedance after the TRL procedure [40]. This renormalization takes the characteristic impedance of the *line* standard as an input, which is usually calculated from numerical tools or closed form models. Thus, the accuracy of the impedance interpretation becomes important. Although the values of the reference impedances are usually carefully calculated, discrepancies between the real impedance and

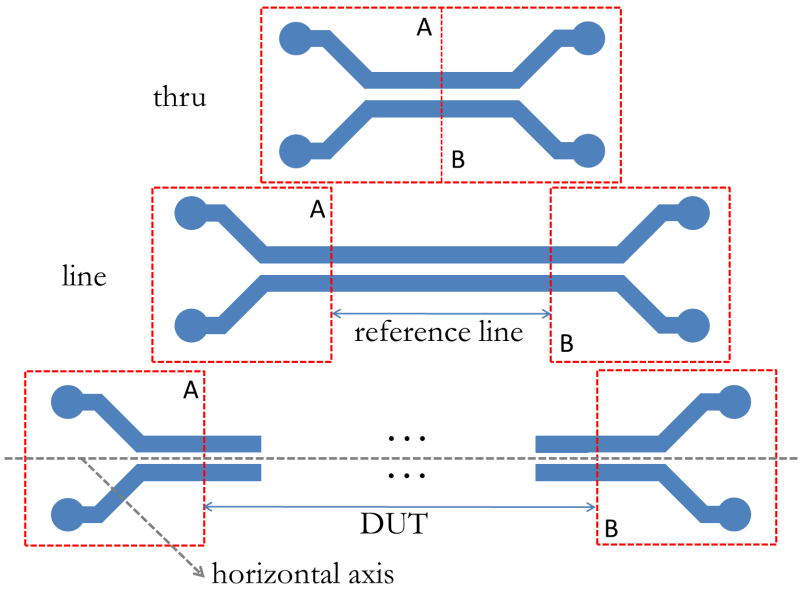

Figure 6.5:
A sketch of a typical differential pair calibration standards. The error boxes **A** and **B** are supposed to have left-right mirror-image symmetry, while the DUT is supposed to have mirror-image symmetry about the horizontal axis.

the interpreted values do exist. In order to evaluate the de-embedding sensitivity due to these discrepancies, we perform an impedance perturbation analysis in the characteristic impedances of the *line* standard.

6.4.1 Theoretical Perturbation Analysis

The layout of a multimode TRL de-embedding procedure is demonstrated in Fig. 6.5. Two error boxes **A** and **B** with mirror-image symmetry are access structures. In the *line* standard, a uniform coupled transmission line of length l is connected between the error boxes. Assuming a perfect mirror-image symmetry of the DUT along the horizontal axis, the *reflection* calibration standard is not required. The in-depth discussions of the mathematical proof of the multimode TRL calibration method can be found in reference [41].

The error boxes are cascaded with each measurement standard using the corresponding T-parameter matrices as follows:

$$\begin{cases} \mathbf{M}_x = \mathbf{A}\mathbf{N}_x\bar{\mathbf{B}} \\ \mathbf{M}_t = \mathbf{A}\overline{\mathbf{B}} \\ \mathbf{M}_l = \mathbf{A}\mathbf{N}_l\overline{\mathbf{B}} \end{cases} \tag{6.48}$$

where $\mathbf{M}_x$, $\mathbf{M}_t$ and $\mathbf{M}_l$ are the known T-parameter matrices converted from the S-parameters measured by the VNA measurements. $\mathbf{N}_l$ corresponds to the uniformly coupled transmission line in the *line* standard, and $\mathbf{N}_x^{\mathrm{DUT}}$ is the unknown transfer matrix of the DUT to be de-embedded.

In (6.48), $\overline{\mathbf{B}}$ is defined as the reverse transfer matrix of $\mathbf{B}$,

$$\overline{\mathbf{B}} = \widetilde{\mathbf{B}^{-1}} = \mathbf{P}_P\mathbf{B}^{-1}\mathbf{P}_P \tag{6.49}$$

where

$$\mathbf{P}_P = \begin{bmatrix} \mathbf{0} & \mathbf{I} \\ \mathbf{I} & \mathbf{0} \end{bmatrix}. \tag{6.50}$$

The permutation transformation $\mathbf{P}_P$ changes the direction of the corresponding T-parameter matrix. Thus, when the mirror-image symmetry of the error boxes is satisfied, we have $\mathbf{A} = \mathbf{B}$. Properties of operation $\widetilde{\mathbf{O}}$ and $\overline{\mathbf{O}}$ for an artificial 4×4 matrix are listed as follows (the corresponding proof can be found in reference [41]).

$$\begin{cases} \overline{\overline{\mathbf{O}}} = \widetilde{\widetilde{\mathbf{O}}} = \mathbf{O} \\ \widetilde{\mathbf{O}_1\mathbf{O}_2} = \widetilde{\mathbf{O}}_1\widetilde{\mathbf{O}}_2 \\ \overline{\mathbf{O}_1\mathbf{O}_2} = \overline{\mathbf{O}}_2\overline{\mathbf{O}}_1 \\ \widetilde{\mathbf{O}} = \overline{\mathbf{O}^{-1}} = \overline{\mathbf{O}}^{-1} \end{cases} \tag{6.51}$$

Assuming that each mode of the *line* standard is matched to their characteristic impedances, the T-parameter matrix becomes a diagonal matrix: $\mathbf{N}_l = \mathbf{N}_l^{\mathrm{diag}}$ as given in (6.27). In this condition, the multi-mode TRL de-embedding solves the T-parameters of the DUT using

the VNA measurement results as inputs:

$$\mathbf{N}_x = f_{\mathrm{TRL}}\left(\mathbf{M}_x, \mathbf{M}_t, \mathbf{M}_l\right)\big|_{\mathbf{N}_l = \mathbf{N}_l^{\mathrm{diag}}}. \tag{6.52}$$

Now we add a small perturbation factor in the T-parameters of the *line* standard.

$$\mathbf{N}_l = \begin{bmatrix} e^{-\gamma_e^l l} & 0 & \xi_e^l \sinh(\gamma_e^l l) & 0 \\ 0 & e^{-\gamma_o^l l} & 0 & \xi_o^l \sinh(\gamma_o^l l) \\ -\xi_e^l \sinh(\gamma_e^l l) & 0 & e^{\gamma_e^l l} & 0 \\ 0 & -\xi_o^l \sinh(\gamma_o^l l) & 0 & e^{\gamma_o^l l} \end{bmatrix}. \tag{6.53}$$

Since $\mathbf{N}_l$ is no longer diagonal, a diagonalization is required to meet the requirement of the TRL procedure:

$$\mathcal{N}_l = \mathbf{D}^{-1}\mathbf{N}_l\mathbf{D}. \tag{6.54}$$

where the transformation matrix, $\mathbf{D}$, is given by (6.26). Note that $\mathbf{D}$ is invariant for the permutation operation defined in (6.49) and (6.50):

$$\mathbf{D} = \widetilde{\mathbf{D}}. \tag{6.55}$$

Thus, the impedance perturbation of the *line* standard can be included using the linear transformation given by $\mathbf{D}$. In the *thru* standard, we have

$$\begin{aligned} \mathcal{M}_t &= \mathbf{M}_t = \mathbf{A}\overline{\mathbf{B}} = \mathbf{A}\mathbf{D}\mathbf{D}^{-1}\overline{\mathbf{B}} = \mathbf{A}\mathbf{D}\widetilde{\mathbf{D}}^{-1}\overline{\mathbf{B}} && (6.56) \\ &= \mathbf{A}\mathbf{D}\overline{\mathbf{D}\mathbf{B}} = \mathbf{A}\mathbf{D}\overline{\mathbf{B}}\overline{\mathbf{D}} = \mathcal{A}\mathcal{B}, && (6.57) \end{aligned}$$

where

$$\begin{cases} \mathcal{A} = \mathbf{A}\mathbf{D} \\ \mathcal{B} = \mathbf{B}\mathbf{D} \end{cases}. \tag{6.58}$$

$\mathcal{A}$ and $\mathcal{B}$ are defined as 'effective error boxes' that include the impedance perturbations of the *line* standard. Note that when identical error boxes ($\mathbf{A} = \mathbf{B}$) are assumed, effective error boxes are also identical ($\mathcal{A} = \mathcal{B}$). In (6.56), properties listed in (6.51) and (6.55) are used. Similarly,

$$\begin{aligned} \mathcal{M}_l &= \mathbf{M}_l = \mathbf{A}\mathbf{N}_l\overline{\mathbf{B}} = \mathbf{A}\mathbf{D}\mathbf{D}^{-1}\mathbf{N}_l\mathbf{D}\mathbf{D}^{-1}\overline{\mathbf{B}} \\ &= (\mathbf{A}\mathbf{D})(\mathbf{D}^{-1}\mathbf{N}_l\mathbf{D})(\overline{\mathbf{B}\mathbf{D}}) = \mathcal{A}\mathcal{N}_l\overline{\mathcal{B}} \end{aligned} \tag{6.59}$$

and

$$\begin{aligned} \mathcal{M}_x &= \mathbf{M}_x = \mathbf{A}\mathbf{N}_x\overline{\mathbf{B}} \\ &= (\mathbf{A}\mathbf{D})(\mathbf{D}^{-1}\mathbf{N}_x\mathbf{D})(\overline{\mathbf{B}\mathbf{D}}) = \mathcal{A}\mathcal{N}_x\overline{\mathcal{B}}. \end{aligned} \tag{6.60}$$

Observing (6.56), (6.59) and (6.60), since $\mathcal{N}_l$ is diagonal, the TRL de-embedding can be carried out:

$$\mathcal{N}_x = f_{\mathrm{TRL}}\left(\mathcal{M}_x, \mathcal{M}_t, \mathcal{M}_l\right). \tag{6.61}$$

Thus, the relation between the exact de-embedding result and the perturbed result is

$$\mathbf{N}_x = \mathbf{D}\mathcal{N}_x\mathbf{D}^{-1}. \tag{6.62}$$

Comparing (6.62) to (6.28), the transformation is effectively a renormalization of the reference impedance in the de-embedded T-parameters based on the mismatch of the *line* standard. Similar discussions can be found in reference [40]. The perturbation analysis based on (6.62) can be applied to evaluate the accuracy of the de-embedded result given by the reference-impedance mis-interpretation, if any, in the final renormalization procedure. For example, if the DUT is a differential transmission line within the perturbation limit,

the T-parameter matrix can be written as

$$\mathcal{N}_x = \begin{bmatrix} e^{-\gamma_e^x l_x} & 0 & \xi_e^x \sinh(\gamma_e^x l_x) & 0 \\ 0 & e^{-\gamma_o^x l_x} & 0 & \xi_o^x \sinh(\gamma_o^x l_x) \\ -\xi_e^x \sinh(\gamma_e^x l_x) & 0 & e^{\gamma_e^x l_x} & 0 \\ 0 & -\xi_o^x \sinh(\gamma_o^x l_x) & 0 & e^{\gamma_o^x l_x} \end{bmatrix}, \tag{6.63}$$

where the propagation constant γ_i^x and the mismatching factor ξ_x^i are calculated from the TRL procedure f_{TRL}. The renormalization matrix $\mathbf{D}$ can be given in the form of (6.26) where ξ_e^l and ξ_o^l are input values given by some numerical interpretation of the reference line's impedances. Thus, small errors in this numerical interpretation can be included as $\xi_i^l \pm \Delta$. Given by the transformation in (6.62) and the S-T relation in (6.16), the final S-parameters of the DUT can be given as

$$S_{13}^i = S_{31}^i \approx e^{-\gamma_i^x l_x} + \left(\xi_i^l \pm \Delta\right) \xi_i^x \sinh\left(\gamma_i^x l_x\right) \tag{6.64}$$

and

$$S_{11}^i = S_{33}^i \approx \frac{(\xi_i^l + \xi_i^x \pm \Delta) \sinh(\gamma_e^{\mathrm{TRL}} l_x)}{\exp\left(\gamma_e^{\mathrm{TRL}} l_x\right)}. \tag{6.65}$$

Since the DUT is assumed to be at the near-matching limit, the de-embedding sensitivity in the insertion-loss terms is a second-order small quantity, while the return-loss elements are sensitive to the first order.

6.4.2 Experimental Verification

To verify the sensitivity interpretation given in (6.64) and (6.65), we design a set of uniformly coupled striplines on a test board and carry out the TRL de-embedding method. We use two different *line* standards in the TRL procedure and compare the two sets of de-embedding results to evaluate the accuracy sensitivity due to the change in the *line* standards. The device setup follows the design shown in Fig. 6.6. In this layout, the distance

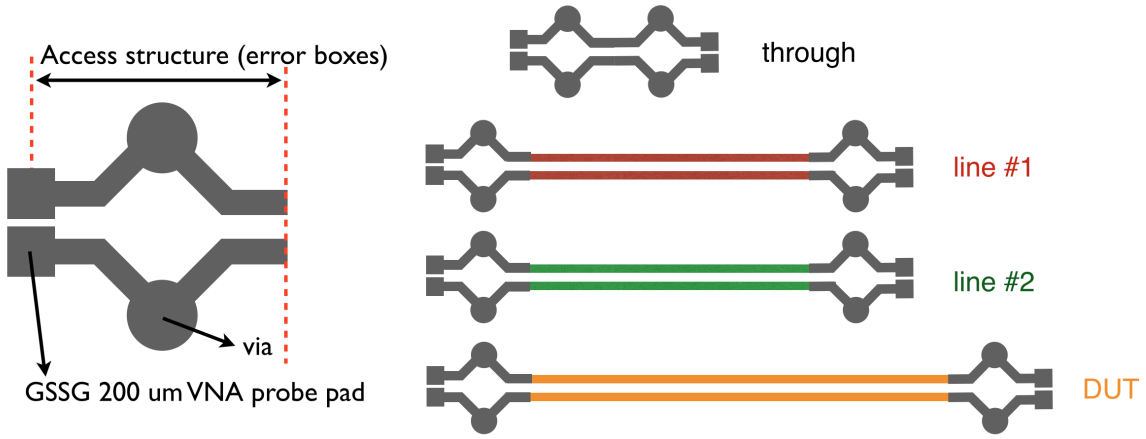

Figure 6.6:
(Color online) Schematic experimental setup and the details of the access structure. A set of uniform differential transmission lines are applied as the *through* standard, the *line* standard and the DUT. Two different *line* standards (#1 and #2) are applied to check the de-embedding sensitivity.

between the ground planes is $b = 398.78\,\mu$m, and the copper foil thickness is $t = 25.4\,\mu$m. The error boxes (access structures) of these measurements are identical: a pair of GSSG 200 μm VNA probe pads connected to the stripline-layer by two symmetrical vias. In the *line* standard #1, $S = 127\,\mu$m and $W = 215.9\,\mu$m, while parameters for the *line* standard #2 is $S = W = 127\,\mu$m. These two line standards are of the same length ($l = 76.2\,$mm). The dielectric material between the ground planes is Panasonic Megtron 6 whose static dielectric constant is around 3.64 and the corresponding loss tangent is approximately 0.011 in the interested frequency range. Utilizing these parameters in (6.29), by design, the characteristic impedances for *line* standard #1 is $Z_{ce} = 49.71\,\Omega$, $Z_{co} = 38.23\,\Omega$, while for the #2 *line* the impedance values are $Z_{ce} = 65.39\,\Omega$, $Z_{co} = 46.87\,\Omega$. The DUT is also designed as a uniformly coupled stripline, whose geometry parameters are $S = 225.552\,\mu$m, $W = 155.575\,\mu$m and $l = 177.8\,$mm.

The two sets of de-embedded S-parameters are compared in Fig. 6.7. The corresponding S-parameters of the DUT predicted by the RLGC model is also plotted in the same figure for comparison. Due to the difference in the reference lines, the insertion-loss

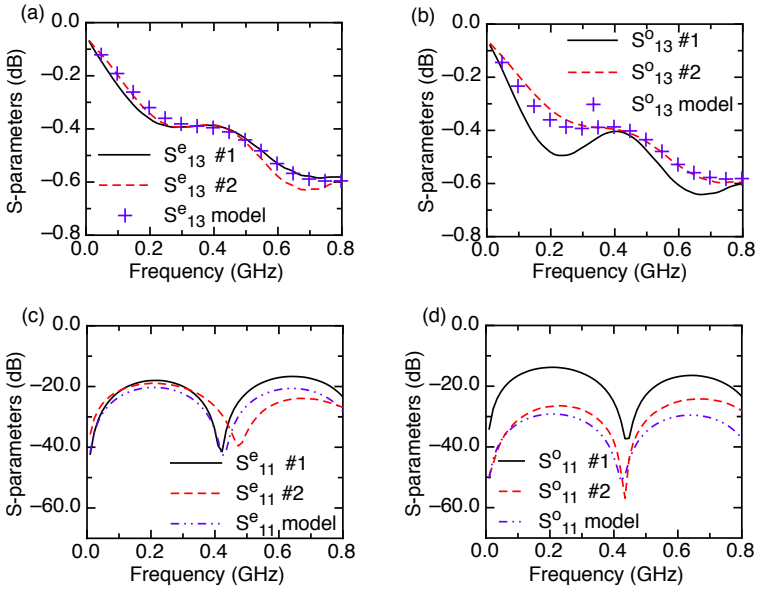

Figure 6.7:
Measurement results after the TRL procedure. The S-parameters of the DUT using reference line #1 and #2 are compared. (a) and (b) presents the insertion-loss terms for the even mode and the odd mode, while the return-loss terms are given in (c) and (d). The DUT S-parameters given by the frequency-dependent RLGC model are plotted in all sub figures for comparison.

terms (S^i_{13}) change by $\sim 0.2\,\mathrm{dB}$, while the return-loss terms (S^i_{11}) change by $10 \sim 20\,\mathrm{dB}$. This result follows the same trend given by (6.64) and (6.65). According to these two equations, assuming the RLGC prediction is accurate ($\Delta = 0$), the de-embedded result should be equal to the predicted value when the *line* standard is perfectly matched ($\xi^l_i = 0$, $i = e, o$). In the experimental setup, we designed reference line #1 to match its even mode, while line #2 matches its odd mode. Thus, as demonstrated in Fig. 6.7 (a) and (c), the #1 de-embedding result matches the RLGC model better in the even mode. While in Fig. 6.7 (b) and (d), the results given by line #2 match better to the odd mode. The difference in the TRL results comes from the different impedances in the two *line* standards. As pointed out in reference [40], it is necessary to renormalize the results based on accurately calculated impedances of the *line* standard.

The two sets of S-parameters after renormalization are demonstrated in Fig. 6.8. Here we utilize the relation given by (6.62) to confirm the validity of the impedance perturbation theory. If the renormalization is accurate, the de-embedded results given by line #1 and line #2 should converge to the RLGC model. The renormalized results are presented in Fig. 6.8. Comparing it to Fig. 6.7, the discrepancies of the two de-embedding results become smaller. Both of the two results approach closer to the exact RLGC model. The insertion-loss errors are controlled within $\sim 0.1\,\mathrm{dB}$, while the return-loss terms in the odd mode present errors of $\sim 5\,\mathrm{dB}$. These errors might come from the differences between the actual impedances in the reference lines and the values given by the closed form model. Another origin for these errors might be the asymmetry of the error boxes due to the product tolerances. To quantify the de-embedding errors, we apply the recently introduced point-to-point "global difference measure (GDM)" [141, 142] to compare the measured results to the RLGC model. The GDM of the return-loss is ~ 0.3 while the insertion-loss is ~ 0.02, indicating the insertion-loss is an order of magnitude more accurate than the return-loss. This agrees with the accuracy analysis given by (6.64) and (6.65).

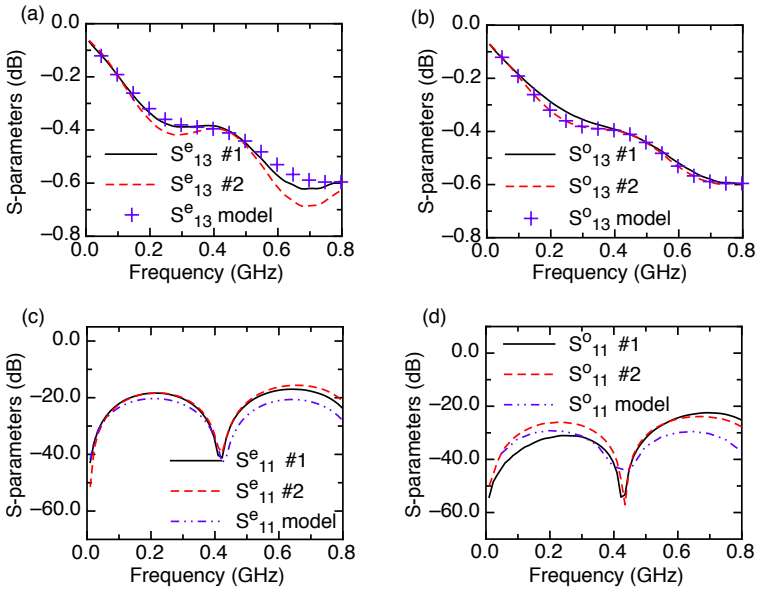

Figure 6.8:
Normalized de-embedded results. The S-parameter matrix elements given by two different reference lines are compared after an impedance renormalization. (a) and (b) presents the insertion-loss terms for the even mode and the odd mode. The return-loss terms are given in (c) and (d).

Chapter 7

Notes and derivations

7.1 Normalized effective field

The LLG equation is written as

$$\dot{\mathbf{M}} = -\gamma \left(\mathbf{M} \times \mathbf{H}_{\text{eff}} \right) + \frac{\alpha}{M_s} \mathbf{M} \times \dot{\mathbf{M}} \tag{7.1}$$

where M_s is the saturation magnetization, $\mathbf{M} = M_s \mathbf{m}\left(\mathbf{r}\right)$ is the spin texture field in units of A/m, and γ is the gyromagnetic ratio. If the effective field is in the unit of Tesla, the gyromagnetic ration is 28GHz/T. In numerical simulations, it is more convenient to use the H field, where $\mathbf{H}_{\text{eff}} = \mathbf{B}_{\text{eff}}/\mu_0$. Thus, the gyromagnetic ratio should be $2.21 \times 10^5\,\text{A}\cdot\text{m}^{-1}\text{s}^{-1}$. The definition of $\mathbf{H}_{\text{eff}}$ is

$$\mathbf{H}_{\text{eff}} = -\frac{1}{\mu_0 M_s} \cdot \frac{d\epsilon}{d\mathbf{m}} \tag{7.2}$$

where ϵ is the free energy density of the spin texture.

$$\epsilon = A \left(\nabla \mathbf{m} \right)^2 + f_{\text{an}} - \mu_0 M_s \mathbf{m} \cdot \mathbf{H}_a \tag{7.3}$$

where A is the exchange stiffness. The value is usually material determined. One can derive this term from Heisenberg model. The relation between A and the Heisenberg exchange,

J is determined by the atomic structure and the symmetry. For cubical lattice, $A = \frac{J_0}{a_0}$, where J_0 is the exchange energy between nearest unit cells, and a_0 is the lattice constant.

f_{an} is the anisotropy energy density. Its form is determined by the type of anisotropy taken into account. Usually there are two origins of this term: the lattice structure and the shape aspect ratio. For simple cubic materials (B20 compounds), the anisotropy from the lattice is usually very weak, which is thus neglected in Bloch-type skyrmion simulations. For polycrystalline simulations, the anisotropy is mainly induced from the shape. In devices with interfaces, the detail of the interface could give rise to strain or proximity effects, which might induce extra anisotropy. This type of anisotropy is difficult to predict theoretically. The shape anisotropy is induced from the demagnetization field from the dipolar interactions. For a uniformly magnetized body its form is

$$f_{\text{dmag}}^{\text{an}} = \frac{1}{2}\mu_0 \mathbf{M}^2 \left(\alpha_1 N_a + \alpha_2 N_b + \alpha_3 N_c\right) \tag{7.4}$$

where

$$\mathbf{N} = \begin{bmatrix} N_a & 0 & 0 \\ 0 & N_b & 0 \\ 0 & 0 & N_c \end{bmatrix} \tag{7.5}$$

is the demagnetization tensor determined by the shape of the body. α_i is the axial cosine. For an infinitely large thin film, $N_a = N_b = 0$, while $N_c = 1$. Thus,

$$f_{\text{an}} = \frac{1}{2}\mu_0 M_s^2 m^2 \cos^2\theta_z = \frac{1}{2}\mu_0 M_s^2 \mathbf{m}_z^2 = \frac{1}{2} K_u m_z^2. \tag{7.6}$$

From Eq. 7.2, $\mathbf{H}_{\text{eff}}$ can be written as

$$\mathbf{H}_{\text{eff}} = \frac{2A}{\mu_0 M_s}\nabla^2 \mathbf{m} - \frac{K_u}{\mu_0 M_s} m_z + \mathbf{H}_a. \tag{7.7}$$

In order to numerically solve the LLG equation, discretization of $\mathbf{H}_{\text{eff}}$ is necessary. In a 2D square grid, the magnetization on each site is $\mathbf{m}_{i,j}$, and the distance between

neighboring sites is a. The effective field is thus written as

$$\mathbf{H}_{\text{eff}}^{i,j} = \frac{2A}{\mu_0 M_s}\left[\frac{\mathbf{m}_{i+1,j} - 2\mathbf{m}_{i,j} + \mathbf{m}_{i-1,j}}{a^2} + \frac{\mathbf{m}_{i,j+1} - 2\mathbf{m}_{i,j} + \mathbf{m}_{i,j-1}}{a^2}\right] - \frac{K_u m_z^{i,j}}{\mu_0 M_s} + H_a^{i,j} \quad (7.8)$$

From Eq. 7.8, the LLG equation is written as

$$\dot{\mathbf{m}} = -\gamma\left(\mathbf{m} \times \mathbf{H}_{\text{eff}}\right) + \alpha \mathbf{m} \times \dot{\mathbf{m}} \quad (7.9)$$

and then

$$\frac{a^2 \mu_0 M_s}{2A\gamma}\dot{\mathbf{m}} = \mathbf{m} \times \left(\mathbf{P} - \frac{K_u a^2}{2A} m_z + \frac{\mathbf{H}_a a^2 \mu_0 M_s}{2A}\right) + \alpha \frac{a^2 \mu_0 M_s}{2A\gamma}\mathbf{m} \times \dot{\mathbf{m}}. \quad (7.10)$$

where $\mathbf{P} = \mathbf{m}_{i+1,j} + \mathbf{m}_{i-1,j} + \mathbf{m}_{i,j+1} + \mathbf{m}_{i,j-1}$. Note that $m_{i,j}$ is removed because its contribution is zero due to the cross product with itself. Define $\mathbf{S}_{i,j}\left(t'\right) = \mathbf{m}_{i,j}\left(t\right)$, and $t = \frac{a^2 \mu_0 M_s}{2A\gamma} t'$, the LLG equation can be simplified as

$$\dot{\mathbf{S}}_{i,j} = -\mathbf{S}_{i,j} \times \mathbf{h}_{\text{eff}} + \alpha \mathbf{S}_{i,j} \times \dot{\mathbf{S}}_{i,j} \quad (7.11)$$

where $\dot{\mathbf{S}}_{i,j} = \frac{d\mathbf{S}_{i,j}}{dt'}$ and

$$\mathbf{h}_{\text{eff}} = \mathbf{S}_{i+1,j} + \mathbf{S}_{i-1,j} + \mathbf{S}_{i,j+1} + \mathbf{S}_{i,j-1} - \xi_{es} S_{i,j}^z + \xi_a \mathbf{h}_a \quad (7.12)$$

which is implemented in the method SpinSystem.CalculateEffectiveField in the case of $J = 1$. The definition of a dimensionless physical second is given by

$$t = \frac{a^2 \mu_0 M_s}{2A\gamma} t'$$

to relate to the actual time in the unit of seconds. Real values of parameters can be included by

$$\xi_{es} = \frac{K_u a^2}{2A}$$

and

$$\xi_a = \frac{H_a a^2 \mu_0 M_s}{2A}$$

7.2 Slonczewski torque

Slonczewski torque is define as

$$\tilde{\tau} = \frac{\gamma \hbar j P}{2eM_s \mu_0 t} \mathbf{m} \times (\boldsymbol{\sigma} \times \mathbf{m}) \tag{7.13}$$

where j is the vertically injected current density; P is the injected spin polarization; $\boldsymbol{\sigma}$ is the injected dimensionless spin. Eq. 7.13 should be added to the right side of Eq. 7.9. After renormalization, the dimensionless torque added to the right side of Eq. 7.11 should be

$$\tau = \frac{\hbar j P a^2}{4e^2 A} \mathbf{m} \times (\boldsymbol{\sigma} \times \mathbf{m}) = \xi_{\mathrm{STT}} \mathbf{m} \times (\boldsymbol{\sigma} \times \mathbf{m}) \,. \tag{7.14}$$

Take FeGe thin film of 1nm for example, the Oersted field given by a vertical, cylindrical electrode is given by

$$\oint_C \mathbf{B} \cdot d\mathbf{l} = \mu_0 I \tag{7.15}$$

$$B \cdot 2\pi R = \mu_0 \pi R^2 j. \tag{7.16}$$

Thus, at the edge of the electrode, the ratio between the Oersted field and the torque induced effective field is

$$\frac{\xi_{\mathrm{STT}}}{\xi_a} = \frac{\hbar P}{etR\mu_0 M_s}. \tag{7.17}$$

Using the parameters for FeGe thin film of 1nm ($M_s = 10^5\,\mathrm{Am}^{-1}$, $R = 5\,\mathrm{nm}$), this ratio is 176.876, indicating the STT is two orders of magnitudes larger than the Oersted field torque.

7.3 Spin current

The total current operator at a terminal m is given as

$$\{\mathbf{I}_m\} = \frac{i}{2\pi\hbar}\left[\mathbf{G}^n\mathbf{\Sigma}_m^\dagger - \mathbf{\Sigma}_m\mathbf{G}^n + \mathbf{G}^r_{mm}\mathbf{\Sigma}_m^{\text{in}} - \mathbf{\Sigma}_m^{\text{in}}\mathbf{G}^a_{mm}\right] \tag{7.18}$$

where

$$\mathbf{G}^n = \mathbf{G}_0^n + \delta\mathbf{G}^n$$

$$\mathbf{G}_0^n = \sum_m \mathbf{A}_m f_0$$

$$\delta\mathbf{G}^n = \left(-\frac{\partial f_0}{\partial\epsilon}\right)\sum_m \mathbf{A}_m\delta\mu_m$$

and

$$\mathbf{\Sigma}_m^{\text{in}} = \mathbf{\Sigma}_m^{\text{in},0} + \delta\mathbf{\Sigma}_m^{\text{in}}$$

$$\Sigma_m^{\text{in}} = \sum_m \mathbf{\Gamma}_m f_0$$

$$\delta\mathbf{\Sigma}_m^{\text{in}} = \left(-\frac{\partial f_0}{\partial\epsilon}\right)\sum_m \mathbf{\Gamma}_m\delta\mu_m$$

$\delta\mu_m = \mu_m - \epsilon_F$, which comes from the linear response limit:

$$f_m = \left(-\frac{\partial f_0}{\partial\epsilon}\right)(\mu_m - \epsilon_F) + f_0.$$

The current operator can be written as the sum of the non-equilibrium part and the equilibrium part:

$$\{\mathbf{I}_m\} = \{\mathbf{I}_m^{\text{eq}} + \mathbf{I}_m^{\text{neq}}\}$$

where

$$\{\mathbf{I}_m^{\text{neq}}\} = \frac{i}{2\pi\hbar}\left[\delta\mathbf{G}^n\mathbf{\Sigma}_m^\dagger - \mathbf{\Sigma}_m\delta\mathbf{G}^n + \mathbf{G}^r_{mm}\delta\mathbf{\Sigma}_m^{\text{in}} - \delta\mathbf{\Sigma}_m^{\text{in}}\mathbf{G}^a_{mm}\right].$$

The non-equilibrium spin current at zero temperature is then given as

$$J_m^{\tilde{\mathbf{s}},\mathrm{neq}} = \frac{i}{4\pi}\mathrm{Tr}\left[\vec{\sigma}\mathbf{I}_m^{\mathrm{neq}}\left(\epsilon_F\right)\right]$$

where

$$\tilde{\sigma} = \mathcal{I}_{m\times m}\otimes\hat{\sigma}$$

is the extended Pauli matrix.

7.4 Spin transfer torque (STT)

Starting from

$$\frac{\partial\mathbf{G}^n}{\partial t} = \frac{i}{2\pi\hbar}\left\{\delta\mathbf{G}^n\mathbf{H} - \mathbf{H}\delta\mathbf{G}^n + \sum_m\left[\delta\mathbf{G}^n\mathbf{\Sigma}_m^{\dagger} - \mathbf{\Sigma}_m\delta\mathbf{G}^n + \mathbf{G}_{mm}^r\delta\mathbf{\Sigma}_{mm}^{\mathrm{in}} - \mathbf{G}_{mm}^a\delta\mathbf{\Sigma}_{mm}^{\mathrm{in}}\right]\right\}$$

$$\frac{\partial\left\langle\hat{\sigma}\right\rangle}{\partial t} = \sum_m I_m^{\sigma} + \left\langle\hat{\tau}\right\rangle$$

where

$$\left\langle\hat{\tau}\right\rangle = \frac{i}{2\pi\hbar}\mathrm{Tr}\left\{\hat{\sigma}\left[\delta\mathbf{G}^n\mathbf{H} - \mathbf{H}\delta\mathbf{G}^n\right]\right\}.$$

On each site, at linear response limit, all terms of $\mathbf{H}$ that do not contain spin are canceled. Only $H_{\sigma S}^L = -J_{\mathrm{H}}\hat{\sigma}\cdot\mathbf{S}_L$ has a non-zero contribution:

$$\left\langle\hat{\tau}_L\right\rangle = \frac{-iJ_{\mathrm{H}}}{2\pi\hbar}\mathrm{Tr}\left[\hat{\sigma}\delta\mathbf{G}_L^n\left(\hat{\sigma}\cdot\vec{S}_L\right) - \hat{\sigma}\left(\hat{\sigma}\cdot\vec{S}_L\right)\delta\mathbf{G}_L^n\right]$$

$$\left\langle\tau_L^x\right\rangle = \frac{-iJ_{\mathrm{H}}}{2\pi\hbar}\mathrm{Tr}\left[\delta\mathbf{G}^n\left(\sigma_xS_x + \sigma_yS_y + \sigma_zS_z\right)\sigma_x - \sigma_x\left(\sigma_xS_x + \sigma_yS_y + \sigma_zS_z\right)\delta\mathbf{G}^n\right]$$

$$\left\langle\tau_L^x\right\rangle = \frac{-iJ_{\mathrm{H}}}{2\pi\hbar}\mathrm{Tr}\left[\delta\mathbf{G}^n\left(-i\sigma_zS_y + i\sigma_yS_z\right) - \left(i\sigma_zS_y - i\sigma_yS_z\right)\delta\mathbf{G}^n\right]$$

$$\left\langle\tau_L^x\right\rangle = \frac{J_{\mathrm{H}}}{2\pi\hbar}\mathrm{Tr}\left[\delta\mathbf{G}^n\left(\sigma_yS_z - \sigma_zS_y\right) - \left(\sigma_zS_y - \sigma_yS_z\right)\delta\mathbf{G}^n\right]$$

$$\left\langle\tau_L^x\right\rangle = \frac{J_{\mathrm{H}}}{\pi\hbar}\mathrm{Tr}\left[\left(\sigma_yS_z - \sigma_zS_y\right)\delta\mathbf{G}^n\right]$$

$$\langle \tau_L^x \rangle = \frac{2J_{\mathrm{H}}}{\hbar} \mathrm{Tr} \left(\langle \sigma_y \rangle S_z - \langle \sigma_z \rangle S_y \right)$$

$$\langle \hat{\tau}_L \rangle = \frac{2J_{\mathrm{H}}}{\hbar} \langle \hat{\sigma} \rangle \times \mathbf{S}_L$$

where

$$\langle \hat{\sigma} \rangle = \frac{1}{2\pi} \mathrm{Tr} \left[\hat{\sigma} \delta \mathbf{G}^n \right].$$

Thus, the total spin current is not conserved. The torque felt by the itinerant spin is:

$$2J_{\mathrm{H}} \langle \hat{\sigma} \rangle \times \mathbf{S}_L$$

whose unit is changed to $\left[\frac{J}{\hbar}\right]$. J is the nearest neighbor exchange in the magnetic system. The torque exerted on the magnetization is thus:

$$-2J_{\mathrm{H}} \langle \hat{\sigma} \rangle \times \mathbf{S}_L$$

For LLG equation:

$$\begin{aligned}
\frac{\partial \mathbf{S}}{\partial t} &= -\mathbf{S} \times \mathbf{H}_{\mathrm{eff}} + \alpha \mathbf{S} \times \frac{\partial \mathbf{S}}{\partial t} + 2J_{\mathrm{H}} \mathbf{S} \times \langle \boldsymbol{\sigma} \rangle \\
\frac{\partial \mathbf{S}}{\partial t} &= -\mathbf{S} \times \mathbf{H}_{\mathrm{eff}} + \alpha \mathbf{S} \times \left\{ -\mathbf{S} \times \mathbf{H}_{\mathrm{eff}} + \alpha \mathbf{S} \times \frac{\partial \mathbf{S}}{\partial t} + 2J_{\mathrm{H}} \mathbf{S} \times \langle \boldsymbol{\sigma} \rangle \right\} + 2J_{\mathrm{H}} \mathbf{S} \times \langle \boldsymbol{\sigma} \rangle \\
\frac{\partial \mathbf{S}}{\partial t} &= -\mathbf{S} \times \mathbf{H}_{\mathrm{eff}} - \alpha \mathbf{S} \times (\mathbf{S} \times \mathbf{H}_{\mathrm{eff}}) + \alpha^2 \mathbf{S} \times \left(\mathbf{S} \times \frac{\partial \mathbf{S}}{\partial t} \right) + \alpha 2J_{\mathrm{H}} \mathbf{S} \times (\mathbf{S} \times \langle \boldsymbol{\sigma} \rangle) + 2J_{\mathrm{H}} \mathbf{S} \times \langle \boldsymbol{\sigma} \rangle \\
\frac{\partial \mathbf{S}}{\partial t} &= -\mathbf{S} \times \mathbf{H}_{\mathrm{eff}} - \alpha \mathbf{S} \times (\mathbf{S} \times \mathbf{H}_{\mathrm{eff}}) - \alpha^2 \frac{\partial \mathbf{S}}{\partial t} + \alpha 2J_{\mathrm{H}} \mathbf{S} \times (\mathbf{S} \times \langle \boldsymbol{\sigma} \rangle) + 2J_{\mathrm{H}} \mathbf{S} \times \langle \boldsymbol{\sigma} \rangle \\
\left(1 + \alpha^2\right) \frac{\partial \mathbf{S}}{\partial t} &= -\mathbf{S} \times (\mathbf{H}_{\mathrm{eff}} - 2J_{\mathrm{H}} \langle \boldsymbol{\sigma} \rangle) - \alpha \mathbf{S} \times [\mathbf{S} \times (\mathbf{H}_{\mathrm{eff}} - 2J_{\mathrm{H}} \langle \boldsymbol{\sigma} \rangle)] \\
\frac{\partial \mathbf{S}}{\partial t} &= -\frac{1}{1 + \alpha^2} \mathbf{S} \times \boldsymbol{\mathcal{H}}_{\mathrm{eff}} - \frac{\alpha}{1 + \alpha^2} \mathbf{S} \times (\mathbf{S} \times \boldsymbol{\mathcal{H}}_{\mathrm{eff}})
\end{aligned}$$

where

$$\boldsymbol{\mathcal{H}}_{\mathrm{eff}} = \mathbf{H}_{\mathrm{eff}} - 2J_{\mathrm{H}} \langle \boldsymbol{\sigma} \rangle$$

7.5 Coulomb Scattering

The screened Coulomb potential centered at the center of the universe is

$$v(\mathbf{r}) = \frac{e^2}{4\pi\epsilon\mathbf{r}}.$$

Using the slow potential approximation, it becomes

$$v(\mathbf{r}) = v(z, \mathbf{R}).$$

For any periodic system with localized atomic orbitals, the basis set is $\chi_i^{\mathbf{R}}(\mathbf{r})$. It is centered at cite $\mathbf{R}$, and i labels the atom number inside the unit cell located at $\mathbf{R}$. If we have orthonormal basis set, then

$$\left\langle \chi_i^{\mathbf{R}} | \chi_j^{\mathbf{R}'} \right\rangle = \delta_{ij}\delta(\mathbf{R} - \mathbf{R}').$$

A state in the periodic material is written as

$$|\mathbf{k}, \mathbf{r}\rangle = \sum_i^{4N} c_i(\mathbf{k})\phi_i(\mathbf{k}, \mathbf{r})$$

The Bloch basis is

$$\phi_i = \sum_{\mathbf{R}} e^{i\mathbf{k}\cdot\mathbf{R}} \left|\chi_i^{\mathbf{R}}\right\rangle = \frac{1}{\sqrt{A}} \int_{\mathbf{R}} e^{i\mathbf{k}\cdot\mathbf{R}} \left|\chi_i^{\mathbf{R}}\right\rangle d\mathbf{R}.$$

The matrix element of a Coulomb scattering source located at layer j is:

$$H^{(j)}_{\mathbf{k}'\mathbf{k}} = \frac{1}{A} \sum_i^{4N} c_i^*(\mathbf{k}') \int_{\mathbf{R}'} \left\langle \chi_i^{\mathbf{R}'} \right| e^{-i\mathbf{k}'\cdot\mathbf{R}'} v(z, \mathbf{R}) \sum_j^{4N} c_j(\mathbf{k}) \int_R \left|\chi_j^{\mathbf{R}}\right\rangle e^{i\mathbf{k}\cdot\mathbf{R}} d\mathbf{R}' d\mathbf{R}.$$

Applying the orthonormal condition, one can have:

$$H^{(j)}_{\mathbf{k'k}} = \frac{1}{A}\sum_i^{4N} c_i^*(\mathbf{k'})c_i(\mathbf{k})\int_{\mathbf{R}} e^{-i(\mathbf{k'}-\mathbf{k})\cdot\mathbf{R}} v(z,\mathbf{R})d\mathbf{R} = \frac{1}{A}\sum_i^{4N} c_i^*(\mathbf{k'})c_i(\mathbf{k})\frac{e^2}{2\epsilon}\frac{e^{-\sqrt{q_0^2+\beta^2}|z|}}{\sqrt{q_0^2+\beta^2}}$$

where $z = |L_i - L_j|\Delta$ and $\beta = \mathbf{k'} - \mathbf{k}$. The total scattering rate is

$$\frac{1}{\tau} = \sum_j AN_j \frac{2\pi}{\hbar}\sum_{\mathbf{k'}} |H^{(j)}_{\mathbf{k'k}}|^2 \times \left|1 - \frac{\mathbf{v}(\mathbf{k'})\cdot\mathbf{v}(\mathbf{k})}{v^2(\mathbf{k})}\right| \times \delta(\epsilon' - \epsilon),$$

where AN_j is the total number of scattering sorces at layer j.

$$\delta(\epsilon' - \epsilon) = \frac{\delta(k' - k_1)}{\frac{\partial\epsilon'}{\partial k'}|_{k_1}} + \frac{\delta(k' - k_2)}{\frac{\partial\epsilon'}{\partial k'}|_{k_2}} = 2\pi[D(\epsilon_1)\frac{\delta(k' - k_1)}{k_1} + D(\epsilon_2)\frac{\delta(k' - k_2)}{k_2}].$$

$$\frac{1}{\tau(k)} = \frac{1}{\tau_1} + \frac{1}{\tau_2}$$

$$\frac{1}{\tau_\alpha} = \frac{1}{\hbar}\frac{e^4}{4\epsilon^2}\int_0^{2\pi}\{\left|\sum_j N_j \sum_1^{4N} c_i^*(\mathbf{k}_\alpha)c_i(\mathbf{k})\frac{e^{-\sqrt{q_0^2+\beta^2}|z|}}{\sqrt{q_0^2+\beta^2}}\right|^2 D(\epsilon_\alpha) \times \left|1 - \frac{\mathbf{v}(\mathbf{k}_\alpha)\cdot\mathbf{v}(\mathbf{k})}{v^2(\mathbf{k})}\right|\}d\theta$$

$\alpha = 1, 2$, which labels the inter-band and intra-band scattering mechanisms.

7.6 Mobility

To calculate mobility μ, we start from Boltzmann equation at relaxation time approximation.

$$f_A^{(i)}(\mathbf{k}) = -\tau_i(\mathbf{k})e\mathcal{E}_x\frac{1}{\hbar}\frac{\partial f_0 \partial\epsilon_i}{\partial\epsilon_i \partial k}\cos\theta$$

The mobility is given by:

$$\mu = \frac{\langle v_x\rangle}{\mathcal{E}_x} = \frac{\sum_{\mathbf{k},i} v_x^{(i)}(\mathbf{k})f_A^{(i)}(\mathbf{k})}{\mathcal{E}_x\sum_{\mathbf{k},i} f_0^{(i)}(\mathbf{k})} = \frac{-e\sum_i\int_0^\infty kdkd\theta\tau_i(\mathbf{k})\frac{\partial f_0}{\partial\epsilon_i}(\frac{\partial\epsilon_i}{\partial k})^2\cos^2\theta}{2\pi\hbar^2\sum_i\int_0^\infty kdkf_0[\epsilon_i(k)]}$$

Chapter 8

Conclusions

8.1 Interfacial and in-plane charge transport in 3D TI thin films

Due to the selection rule of the interfacial coupling in 3D TI thin films, the vertical tunneling current presents unique features. The momentum-spin locking of the surface states and the opposite chirality of opposite surfaces cause the inter-surface tunneling transmission spectrum to be strongly peaked at the band edges for both the intrinsic and the Rashba-like split case. As a result, the low-bias tunnel conductance is a strong function of temperature and Fermi level. A unique signature of the surface-state tunneling is that the temperature dependence of the tunneling conductance changes sign as ϵ_F scans through the band edges of the gapped Dirac cones. Tunneling transmission is a minimum when the two opposite surfaces are at the same potential, and the Dirac cones of the two surfaces are perfectly aligned. As the inter-surface potential increases, the tunneling transmission increases. The potential dependence of the the transmission can give rise to a non-linear current-voltage response. With a built-in Rashba-like splitting, forward biasing the surface-surface p-n junction generates an I-V response showing negative differential resistance. The temperature, Fermi-level, and bias dependencies of the inter-surface tunneling current in

thin-film topological insulators show unique, identifying signatures of the surface states and their opposite chiralities.

In the case of in-plane transport, the inter-surface coupling of TI thin films can reduce the surface state mobility by an order of magnitude in the low-temperature transport regime where the carrier transport is dominated by Coulomb impurity scattering. Hybridization of the surface states introduces a band gap and an s_z component to the spin. The presence of a band gap reduces the average group velocity, and the s_z component of the spin reduces the protection against large angle scattering. Increasing the temperature or shifting the Fermi level away from the band edges can increase the mobility back to the level of an isolated bulk surface state. An inter surface potential resulting in a Rashba-like splitting reduces the inter-surface mixing and the associated s_z component of the spin and restores the protection against large angle scattering. The Rashba-like splitting also creates a ring shaped band edge which increases the average momentum transfer required for a backscattering event.

8.2 Topological spin Hall effect and STT induced single skyrmion creation

The intrinsic spin Hall effect (SHE) originates from the topology of the Bloch bands in momentum space. The duality between real space and momentum space calls for a spin Hall effect induced from a real space topology in analogy to the topological Hall effect (THE) of skyrmions. This work theoretically demonstrates the topological spin Hall effect (TSHE) in which a pure transverse spin current is generated from a skyrmion spin texture. The type of Hall effects that dominates the transport is determined by the type-of-carrier and spin compositions of the Fermi surface. This work has also demonstrated the critical spin texture of a locally triggered topological transition based on a topological charge analysis. It is identified that the topological protection in each magnetic skyrmion lies in the symmetric Heisenberg exchange energy. The required energy density to create a

single skyrmion is estimated to be $\sim J/a^2$. Based on this analysis, a scheme is proposed to individually create both of the Neel-type and the Bloch-type skyrmions in helimagnetic thin films, utilizing the dynamical excitations induced by the STT from a vertically injected spin-polarized current. The critical switching current density is $\sim 10^7\,\mathrm{A/cm^2}$, which decreases with the easy-plane type uni-axial anisotropy and heating effects. The in-plane polarization performs better than the out-of-plane case, providing an ultrafast switching rate ($\sim 40\,\mathrm{ps}$) and reliable switching outcomes.

8.3 Impedance perturbation theory of multi-conductor transmission lines

This work establishes an impedance perturbation theory to simplify the RLGC model for single-ended and coupled uniform transmission lines. The S-parameters, T-parameters and the propagation constants are directly constructed using an impedance perturbation factor. Comparing to the exact model, the simplified model provides better understanding in how the lumped parameters impact the transmission line performance. Based on our simulations, when the mismatch is small ($Z_0 \pm 15\,\Omega$), the perturbation theory captures the major properties of the exact model, and it explains the oscillating features in the S-parameter magnitudes. In the case of uniformly coupled striplines, the perturbation analysis reveals that the modal splitting of the propagation constant is caused by the splitting in the mismatch factor, $\xi_{e,o}$. In another application example, the perturbation theory is utilized to evaluate the measurement accuracy of the TRL de-embedding method. This result confirms that any small change in the impedance of the reference lines is effectively an impedance renormalization. When the DUT is a differential stripline, it is further confirmed theoretically and experimentally that the de-embedded return-loss is sensitive to any mis-interpretation of the *line*-standard impedance to the first order, while the error of the insertion-loss is smaller than that of the return-loss by an order of magnitude.

Bibliography

[1] Gen Yin, Darshana Wickramaratne, and Roger K. Lake. Tunneling spectroscopy of chiral states in ultra-thin topological insulators. *Journal of Applied Physics*, 113(6):063707, February 2013.

[2] Gen Yin, Darshana Wickramaratne, Yuanyuan Zhao, and Roger K. Lake. Coulomb impurity scattering in topological insulator thin films. *Applied Physics Letters*, 105(3), 2014.

[3] Gen Yin, Xiao-Ding Cai, D. Secker, M. Ortiz, J. Cline, and A. Vaidyanath. Impedance perturbation theory for coupled uniform transmission lines. *Electromagnetic Compatibility, IEEE Transactions on*, 57(2):299–308, April 2015.

[4] Gen Yin, Yizhou Liu, Yafis Barlas, Jiadong Zang, and Roger K. Lake. Topological spin hall effect resulting from magnetic skyrmions. *Phys. Rev. B*, 92:024411, Jul 2015.

[5] D. J. Thouless, M. Kohmoto, M. P. Nightingale, and M. den Nijs. Quantized hall conductance in a two-dimensional periodic potential. *Phys. Rev. Lett.*, 49:405–408, Aug 1982.

[6] B. Andrei Bernevig, Taylor L. Hughes, and Shou-Cheng Zhang. Quantum Spin Hall Effect and Topological Phase Transition in HgTe Quantum Wells. *Science*, 314(5806):1757 –1761, December 2006.

[7] Liang Fu and C. L. Kane. Topological insulators with inversion symmetry. *Phys. Rev. B*, 76(4):045302, July 2007.

[8] C. L. Kane and E. J. Mele. Z_2 Topological Order and the Quantum Spin Hall Effect. *Phys. Rev. Lett.*, 95(14):146802, 2005.

[9] Xiao-Liang Qi and Shou-Cheng Zhang. Topological insulators and superconductors. *Rev. Mod. Phys.*, 83(4):1057–1110, October 2011.

[10] M. Z. Hasan and C. L. Kane. *Colloquium* : Topological insulators. *Rev. Mod. Phys.*, 82:3045–3067, Nov 2010.

[11] Markus BÃŒttiker. Edge-State Physics Without Magnetic Fields. *Science*, 325(5938):278–279, July 2009.

[12] Naoto Nagaosa, Jairo Sinova, Shigeki Onoda, A. H. MacDonald, and N. P. Ong. Anomalous Hall effect. *Rev. Mod. Phys.*, 82(2):1539–1592, May 2010.

[13] Shiing shen Chern. Characteristic classes of hermitian manifolds. *Annals of Mathematics*, 47(1):85–121, 1946.

[14] D. Hsieh, Y. Xia, D. Qian, L. Wray, J. H. Dil, F. Meier, J. Osterwalder, L. Patthey, J. G. Checkelsky, N. P. Ong, A. V. Fedorov, H. Lin, A. Bansil, D. Grauer, Y. S. Hor, R. J. Cava, and M. Z. Hasan. A tunable topological insulator in the spin helical Dirac transport regime. *Nature*, 460(7259):1101–1105, 2009.

[15] Wei Zhang, Rui Yu, Hai-Jun Zhang, Xi Dai, and Zhong Fang. First-principles studies of the three-dimensional strong topological insulators Bi 2 Te 3 , Bi 2 Se 3 and Sb 2 Te 3. *New J. Phys.*, 12:065013, June 2010.

[16] Haijun Zhang, Chao-Xing Liu, Xiao-Liang Qi, Xi Dai, Zhong Fang, and Shou-Cheng Zhang. Topological insulators in Bi2se3, Bi2te3 and Sb2te3 with a single Dirac cone on the surface. *Nat. Phys.*, 5(6):438–442, June 2009.

[17] Xiao-Liang Qi, Rundong Li, Jiadong Zang, and Shou-Cheng Zhang. Inducing a Magnetic Monopole with Topological Surface States. *Science*, 323(5918):1184–1187, February 2009.

[18] Viktor Krueckl and Klaus Richter. Switching Spin and Charge between Edge States in Topological Insulator Constrictions. *Phys. Rev. Lett.*, 107:086803, August 2011.

[19] Naoto Nagaosa and Yoshinori Tokura. Topological properties and dynamics of magnetic skyrmions. *Nat Nano*, 8(12):899–911, 2013.

[20] T.H.R. Skyrme. A unified field theory of mesons and baryons. *Nuclear Physics*, 31:556–569, March 1962.

[21] T. H. R. Skyrme. A non-linear field theory. *Proceedings of the Royal Society of London. Series A. Mathematical and Physical Sciences*, 260(1300):127–138, February 1961.

[22] I. Dzyaloshinsky. A thermodynamic theory of "weak" ferromagnetism of antiferromagnetics. *Journal of Physics and Chemistry of Solids*, 4(4):241–255, 1958.

[23] Albert Fert, Vincent Cros, and João Sampaio. Skyrmions on the track. *Nat Nano*, 8(3):152–156, March 2013.

[24] X. Z. Yu, N. K. anazawa, Y. Onose, K. Kimoto, W. Z. Zhang, S. Ishiwata, Y. Matsui, and Y. Tokura. Near room-temperature formation of a skyrmion crystal in thin-films of the helimagnet FeGe. *Nat Mater*, 10(2):106 – 109, 2011.

[25] Jiadong Zang, Maxim Mostovoy, Jung Hoon Han, and Naoto Nagaosa. Dynamics of skyrmion crystals in metallic thin films. *Physical Review Letters*, 107(13):136804, September 2011.

[26] N. Kanazawa, Y. Onose, T. Arima, D. Okuyama, K. Ohoyama, S. Wakimoto, K. Kakurai, S. Ishiwata, and Y. Tokura. Large Topological Hall Effect in a Short-Period Helimagnet MnGe. *Phys. Rev. Lett.*, 106(15):156603, April 2011.

[27] P. Bruno, V. K. Dugaev, and M. Taillefumier. Topological Hall Effect and Berry Phase in Magnetic Nanostructures. *Phys. Rev. Lett.*, 93(9):096806, August 2004.

[28] S. X. Huang and C. L. Chien. Extended skyrmion phase in epitaxial FeGe(111) thin films. *Physical Review Letters*, 108(26):267201, June 2012.

[29] N. Kanazawa, J.-H. Kim, D. S. Inosov, J. S. White, N. Egetenmeyer, J. L. Gavilano, S. Ishiwata, Y. Onose, T. Arima, B. Keimer, and Y. Tokura. Possible skyrmion-lattice ground state in the b20 chiral-lattice magnet MnGe as seen via small-angle neutron scattering. *Physical Review B*, 86(13):134425, October 2012.

[30] Yufan Li, N. Kanazawa, X. Z. Yu, A. Tsukazaki, M. Kawasaki, M. Ichikawa, X. F. Jin, F. Kagawa, and Y. Tokura. Robust Formation of Skyrmions and Topological Hall Effect Anomaly in Epitaxial Thin Films of MnSi. *Phys. Rev. Lett.*, 110(11):117202, March 2013.

[31] X. Z. Yu, Y. Onose, N. Kanazawa, J. H. Park, J. H. Han, Y. Matsui, N. Nagaosa, and Y. Tokura. Real-space observation of a two-dimensional skyrmion crystal. *Nature*, 465(7300):901–904, June 2010.

[32] Junichi Iwasaki, Masahito Mochizuki, and Naoto Nagaosa. Current-induced skyrmion dynamics in constricted geometries. *Nat Nano*, 8(10):742–747, October 2013.

[33] Junichi Iwasaki, Masahito Mochizuki, and Naoto Nagaosa. Universal current-velocity relation of skyrmion motion in chiral magnets. *Nature Communications*, 4:1463, February 2013.

[34] Claude Chappert, Albert Fert, and Frédéric Nguyen Van Dau. The emergence of spin electronics in data storage. *Nature materials*, 6(11):813–823, 2007.

[35] Tom Granberg. *Handbook of Digital Techniques for High-Speed Design: Design Examples, Signaling and Memory Technologies, Fiber Optics, Modeling, and Simulation to Ensure Signal Integrity*. Prentice Hall, Upper Saddle River, NJ, June 2004.

[36] C. Svensson and G.E. Dermer. Time domain modeling of lossy interconnects. *IEEE Trans. Adv. Packag.*, 24(2):191–196, 2001.

[37] Ka Mun Ho, K. Vaz, and M. Caggiano. Scattering parameter characterization of differential four-port networks using a two-port vector network analyzer. In *Electronic Components and Technology Conf., 2005. Proc. 55th*, pages 1846–1853 Vol. 2, 2005.

[38] G. Flynn and W. Blood. A de-embedding technique for interconnects. In *Electrical Performance of Electronic Packaging, 2001*, pages 129–132, 2001.

[39] Jiming Song, Feng Ling, G. Flynn, W. Blood, and E. Demircan. A de-embedding technique for interconnects. In *Electrical Performance of Electronic Packaging, 2001*, pages 129–132, 2001.

[40] M. Wojnowski, V. Issakov, G. Sommer, and R. Weigel. Multimode TRL technique for de-embedding of differential devices. In *Microwave Measurements Conference (ARFTG), 2010 75th ARFTG*, pages 1–10, 2010.

[41] M. Wojnowski, V. Issakov, G. Sommer, and R. Weigel. Multimode TRL calibration technique for characterization of differential devices. *IEEE Trans. Microw. Theory Techn.*, 60(7):2220–2247, 2012.

[42] Jiadong Zang and Naoto Nagaosa. Monopole current and unconventional Hall response on a topological insulator. *Phys. Rev. B*, 81(24):245125, June 2010.

[43] Liang Fu and C. L. Kane. Superconducting Proximity Effect and Majorana Fermions at the Surface of a Topological Insulator. *Phys. Rev. Lett.*, 100(9):096407, March 2008.

[44] Ching-Kai Chiu, Matthew J. Gilbert, and Taylor L. Hughes. Vortex lines in topological insulator-superconductor heterostructures. *Phys. Rev. B*, 84(14):144507, October 2011.

[45] Oleg V. Yazyev, Joel E. Moore, and Steven G. Louie. Spin Polarization and Transport of Surface States in the Topological Insulators Bi_2se_3 and Bi_2te_3 from First Principles. *Phys. Rev. Lett.*, 105(26):266806, December 2010.

[46] Joseph Maciejko, Eun-Ah Kim, and Xiao-Liang Qi. Spin Aharonov-Bohm effect and topological spin transistor. *Phys. Rev. B*, 82(19):195409, November 2010.

[47] D. Hsieh, Y. Xia, L. Wray, D. Qian, A. Pal, J. H. Dil, J. Osterwalder, F. Meier, G. Bihlmayer, C. L. Kane, Y. S. Hor, R. J. Cava, and M. Z. Hasan. Observation of Unconventional Quantum Spin Textures in Topological Insulators. *Science*, 323(5916):919 –922, February 2009.

[48] D. Hsieh, D. Qian, L. Wray, Y. Xia, Y. S. Hor, R. J. Cava, and M. Z. Hasan. A topological Dirac insulator in a quantum spin Hall phase. *Nature*, 452:970–974, April 2008.

[49] Liang Fu, C. L. Kane, and E. J. Mele. Topological Insulators in Three Dimensions. *Phys. Rev. Lett.*, 98(10):106803, March 2007.

[50] Y. Xia, D. Qian, D. Hsieh, L. Wray, A. Pal, H. Lin, A. Bansil, D. Grauer, Y. S. Hor, R. J. Cava, and M. Z. Hasan. Observation of a large-gap topological-insulator class with a single Dirac cone on the surface. *Nat. Phys.*, 5(6):398–402, June 2009.

[51] Zhanybek Alpichshev, J. G. Analytis, J.-H. Chu, I. R. Fisher, Y. L. Chen, Z. X. Shen, A. Fang, and A. Kapitulnik. STM Imaging of Electronic Waves on the Surface of Bi_2te_3: Topologically Protected Surface States and Hexagonal Warping Effects. *Phys. Rev. Lett.*, 104(1):016401, January 2010.

[52] A. A. Taskin, Zhi Ren, Satoshi Sasaki, Kouji Segawa, and Yoichi Ando. Observation of Dirac Holes and Electrons in a Topological Insulator. *Phys. Rev. Lett.*, 107(1):016801, June 2011.

[53] Zhi Ren, A. A. Taskin, Satoshi Sasaki, Kouji Segawa, and Yoichi Ando. Large bulk resistivity and surface quantum oscillations in the topological insulator Bi_2te_2se. *Phys. Rev. B*, 82(24):241306, December 2010.

[54] L. Andrew Wray, Su-Yang Xu, Yuqi Xia, David Hsieh, Alexei V. Fedorov, Yew San Hor, Robert J. Cava, Arun Bansil, Hsin Lin, and M. Zahid Hasan. A topological insulator surface under strong Coulomb, magnetic and disorder perturbations. *Nat. Phys.*, 7(1):32–37, January 2011.

[55] Peng Wei, Zhiyong Wang, Xinfei Liu, Vivek Aji, and Jing Shi. Field-effect mobility enhanced by tuning the Fermi level into the band gap of Bi_2se_3. *Phys. Rev. B*, 85(20):201402, May 2012.

[56] Yi Zhang, Ke He, Cui-Zu Chang, Can-Li Song, Li-Li Wang, Xi Chen, Jin-Feng Jia, Zhong Fang, Xi Dai, Wen-Yu Shan, Shun-Qing Shen, Qian Niu, Xiao-Liang Qi, Shou-Cheng Zhang, Xu-Cun Ma, and Qi-Kun Xue. Crossover of the three-dimensional topological insulator Bi2se3 to the two-dimensional limit. *Nat. Phys.*, 6(8):584–588, 2010.

[57] Guanhua Zhang, Huajun Qin, Jing Teng, Jiandong Guo, Qinlin Guo, Xi Dai, Zhong Fang, and Kehui Wu. Quintuple-layer epitaxy of thin films of topological insulator Bi2se3. *Appl. Phys. Lett.*, 95(5):053114–053114–3, August 2009.

[58] H. W. Liu, H. T. Yuan, N. Fukui, L. Zhang, J. F. Jia, Y. Iwasa, M. W. Chen, T. Hashizume, T. Sakurai, and Q. K. Xue. Growth of Topological Insulator Bi2te3 Ultrathin Films on Si(111) Investigated by Low-Energy Electron Microscopy. *Cryst. Growth Des.*, 10(10):4491–4493, 2010.

[59] Hailin Peng, Keji Lai, Desheng Kong, Stefan Meister, Yulin Chen, Xiao-Liang Qi, Shou-Cheng Zhang, Zhi-Xun Shen, and Yi Cui. Aharonov-Bohm interference in topological insulator nanoribbons. *Nat Mater*, 9(3):225–229, March 2010.

[60] Hadar Steinberg, Dillon R. Gardner, Young S. Lee, and Pablo Jarillo-Herrero. Surface State Transport and Ambipolar Electric Field Effect in Bi2se3 Nanodevices. *Nano Lett.*, 10(12):5032–5036, 2010.

[61] Liang He, Faxian Xiu, Xinxin Yu, Marcus Teague, Wanjun Jiang, Yabin Fan, Xufeng Kou, Murong Lang, Yong Wang, Guan Huang, Nai-Chang Yeh, and Kang L. Wang. Surface-Dominated Conduction in a 6 nm thick Bi2se3 Thin Film. *Nano Lett.*, 12(3):1486–1490, 2012.

[62] Chao-Xing Liu, HaiJun Zhang, Binghai Yan, Xiao-Liang Qi, Thomas Frauenheim, Xi Dai, Zhong Fang, and Shou-Cheng Zhang. Oscillatory crossover from two-dimensional to three-dimensional topological insulators. *Phys. Rev. B*, 81(4):041307, January 2010.

[63] Hai-Zhou Lu, Wen-Yu Shan, Wang Yao, Qian Niu, and Shun-Qing Shen. Massive Dirac fermions and spin physics in an ultrathin film of topological insulator. *Phys. Rev. B*, 81(11):115407, March 2010.

[64] Wen-Yu Shan, Hai-Zhou Lu, and Shun-Qing Shen. Effective continuous model for surface states and thin films of three-dimensional topological insulators. *New J. Phys.*, 12(4):043048, April 2010.

[65] Jungpil Seo, Pedram Roushan, Haim Beidenkopf, Y. S. Hor, R. J. Cava, and Ali Yazdani. Transmission of topological surface states through surface barriers. *Nature*, 466(7304):343–346, July 2010.

[66] Qin Liu, Chao-Xing Liu, Cenke Xu, Xiao-Liang Qi, and Shou-Cheng Zhang. Magnetic Impurities on the Surface of a Topological Insulator. *Phys. Rev. Lett.*, 102(15):156603, April 2009.

[67] M. Abul Khayer and Roger K Lake. Modeling and performance analysis of GaN nanowire field-effect transistors and band-to-band tunneling field-effect transistors. *J. Appl. Phys.*, 108(10):104503–104503–7, November 2010.

[68] Datta Supriyo. Nanoscale device modeling: the Green's function method. *Superlattices Microstruct.*, 28(4):253–278, October 2000.

[69] Chao-Xing Liu, Xiao-Liang Qi, HaiJun Zhang, Xi Dai, Zhong Fang, and Shou-Cheng Zhang. Model Hamiltonian for topological insulators. *Phys. Rev. B*, 82(4):045122, July 2010.

[70] N. P. Butch, K. Kirshenbaum, P. Syers, A. B. Sushkov, G. S. Jenkins, H. D. Drew, and J. Paglione. Strong surface scattering in ultrahigh-mobility bi_{2}se_{3} topological insulator crystals. *Phys. Rev. B*, 81(24):241301, June 2010.

[71] Dohun Kim, Sungjae Cho, Nicholas P. Butch, Paul Syers, Kevin Kirshenbaum, Shaffique Adam, Johnpierre Paglione, and Michael S. Fuhrer. Surface conduction of topological dirac electrons in bulk insulating Bi2Se3. *Nat Phys*, 8(6):459–463, June 2012.

[72] Haim Beidenkopf, Pedram Roushan, Jungpil Seo, Lindsay Gorman, Ilya Drozdov, Yew San Hor, R. J. Cava, and Ali Yazdani. Spatial fluctuations of helical Dirac fermions on the surface of topological insulators. *Nat. Phys.*, 7(12):939–943, October 2011.

[73] Zhiyong Wang, Tao Lin, Peng Wei, Xinfei Liu, Randy Dumas, Kai Liu, and Jing Shi. Tuning carrier type and density in Bi2Se3 by ca-doping. *Applied Physics Letters*, 97(4):042112, July 2010.

[74] Qiuzi Li, E. Rossi, and S. Das Sarma. Two-dimensional electronic transport on the surface of three-dimensional topological insulators. *Phys. Rev. B*, 86(23):235443, December 2012.

[75] S. Adam, E. H. Hwang, and S. Das Sarma. Two-dimensional transport and screening in topological insulator surface states. *Phys. Rev. B*, 85(23):235413, June 2012.

[76] N. P. Butch, K. Kirshenbaum, P. Syers, A. B. Sushkov, G. S. Jenkins, H. D. Drew, and J. Paglione. Strong surface scattering in ultrahigh-mobility Bi_2Se_3 topological insulator crystals. 81(24):241301, 2010.

[77] Tsuneya Ando, Alan B. Fowler, and Frank Stern. Electronic properties of two-dimensional systems. *Rev. Mod. Phys.*, 54(2):437–672, April 1982.

[78] Tong Zhang, Jeonghoon Ha, Niv Levy, Young Kuk, and Joseph Stroscio. Electric-field tuning of the surface band structure of topological insulator Sb2Te3 thin films. *Phys. Rev. Lett.*, 111(5):056803, July 2013.

[79] M. I. Dyakonov and V. I. Perel. Current-induced spin orientation of electrons in semiconductors. *Physics Letters A*, 35(6):459–460, July 1971.

[80] M. I. Dyakonov and V. I. Perel. Possibility of Orienting Electron Spins with Current. *Sov. Phys. JETP Lett.*, 13:467, June 1971.

[81] A. A. Bakun, B. P. Zakharchenya, A. A. Rogachev, M. N. Tkachuk, and V. G. Fleisher. Observation of a surface photocurrent caused by optical orientation of electrons in a semiconductor. *Sov. Phys. JETP Lett.*, December 1984.

[82] M. N. Tkachuk, B. P. Zakharchenya, and V. G. Fleisher. Resonant photovoltaic effect in the NMR of nuclei in a semiconductor lattice. *Sov. Phys. JETP Lett.*, July 1986.

[83] J. E. Hirsch. Spin Hall Effect. *Phys. Rev. Lett.*, 83(9):1834–1837, August 1999.

[84] Shuichi Murakami, Naoto Nagaosa, and Shou-Cheng Zhang. Dissipationless Quantum Spin Current at Room Temperature. *Science*, 301(5638):1348–1351, September 2003.

[85] Jairo Sinova, Dimitrie Culcer, Q. Niu, N. A. Sinitsyn, T. Jungwirth, and A. H. MacDonald. Universal Intrinsic Spin Hall Effect. *Phys. Rev. Lett.*, 92(12):126603, March 2004.

[86] Branislav K. Nikolić, Satofumi Souma, Liviu P. Zârbo, and Jairo Sinova. Nonequilibrium Spin Hall Accumulation in Ballistic Semiconductor Nanostructures. *Phys. Rev. Lett.*, 95(4):046601, July 2005.

[87] J. Wunderlich, B. Kaestner, J. Sinova, and T. Jungwirth. Experimental Observation of the Spin-Hall Effect in a Two-Dimensional Spin-Orbit Coupled Semiconductor System. *Phys. Rev. Lett.*, 94(4):047204, February 2005.

[88] Y. K. Kato, R. C. Myers, A. C. Gossard, and D. D. Awschalom. Observation of the Spin Hall Effect in Semiconductors. *Science*, 306(5703):1910–1913, December 2004.

[89] J. Smit. The spontaneous hall effect in ferromagnetics I. *Physica*, 21(6–10):877–887, 1955.

[90] L. Berger. Side-Jump Mechanism for the Hall Effect of Ferromagnets. *Phys. Rev. B*, 2(11):4559–4566, December 1970.

[91] Masaru Onoda and Naoto Nagaosa. Topological Nature of Anomalous Hall Effect in Ferromagnets. *J. Phys. Soc. Jpn.*, 71(1):19–22, January 2002.

[92] F. D. M. Haldane. Berry Curvature on the Fermi Surface: Anomalous Hall Effect as a Topological Fermi-Liquid Property. *Phys. Rev. Lett.*, 93(20):206602, November 2004.

[93] G. E. Volovik. Fractional statistics and analogs of quantum Hall effect in superfluid 3he films. In *AIP Conference Proceedings*, volume 194, pages 136–146. AIP Publishing, October 1989.

[94] Y. Taguchi, Y. Oohara, H. Yoshizawa, N. Nagaosa, and Y. Tokura. Spin Chirality, Berry Phase, and Anomalous Hall Effect in a Frustrated Ferromagnet. *Science*, 291(5513):2573–2576, March 2001.

[95] S. Mühlbauer, B. Binz, F. Jonietz, C. Pfleiderer, A. Rosch, A. Neubauer, R. Georgii, and P. Böni. Skyrmion Lattice in a Chiral Magnet. *Science*, 323(5916):915–919, February 2009.

[96] T. Schulz, R. Ritz, A. Bauer, M. Halder, M. Wagner, C. Franz, C. Pfleiderer, K. Everschor, M. Garst, and A. Rosch. Emergent electrodynamics of skyrmions in a chiral magnet. *Nat Phys*, 8(4):301–304, April 2012.

[97] A. Neubauer, C. Pfleiderer, B. Binz, A. Rosch, R. Ritz, P. G. Niklowitz, and P. Böni. Topological Hall Effect in the A Phase of MnSi. *Phys. Rev. Lett.*, 102(18):186602, May 2009.

[98] S. X. Huang and C. L. Chien. Extended Skyrmion Phase in Epitaxial $\mathrm{FeGe}(111)$ Thin Films. *Phys. Rev. Lett.*, 108(26):267201, June 2012.

[99] Supriyo Datta. *Quantum Transport: Atom to Transistor*. Cambridge University Press, Cambridge, UK; New York, 2nd edition edition, July 2005.

[100] Gen Yin, Yufan Li, Lingyao Kong, Roger K. Lake, C. L. Chien, and Jiadong Zang. Topological Charge Analysis of Single Skyrmion Creation with a Nanosecond Current Pulse. *arXiv:1411.7762 [cond-mat]*, November 2014. arXiv: 1411.7762.

[101] Luqiao Liu, Takahiro Moriyama, D. C. Ralph, and R. A. Buhrman. Spin-Torque Ferromagnetic Resonance Induced by the Spin Hall Effect. *Phys. Rev. Lett.*, 106(3):036601, January 2011.

[102] U. K. Rößler, A. N. Bogdanov, and C. Pfleiderer. Spontaneous skyrmion ground states in magnetic metals. *Nature*, 442(7104):797–801, August 2006.

[103] Tôru Moriya. Anisotropic superexchange interaction and weak ferromagnetism. *Physical Review*, 120(1):91–98, October 1960.

[104] N. Kanazawa, Y. Onose, T. Arima, D. Okuyama, K. Ohoyama, S. Wakimoto, K. Kakurai, S. Ishiwata, and Y. Tokura. Large topological hall effect in a short-period helimagnet MnGe. *Physical Review Letters*, 106(15):156603, April 2011.

[105] Jung Hoon Han, Jiadong Zang, Zhihua Yang, Jin-Hong Park, and Naoto Nagaosa. Skyrmion lattice in a two-dimensional chiral magnet. *Physical Review B*, 82(9):094429, September 2010.

[106] W. Munzer, A. Neubauer, T. Adams, S. Muhlbauer, C. Franz, F. Jonietz, R. Georgii, P. Boni, B. Pedersen, M. Schmidt, A. Rosch, and C. Pfleiderer. Skyrmion lattice in the doped semiconductor Fe1xCoxSi. *Phys. Rev. B*, 81(4):041203, January 2010.

[107] S. Seki, X. Z. Yu, S. Ishiwata, and Y. Tokura. Observation of skyrmions in a multiferroic material. *Science*, 336(6078):198 – 201, 2012.

[108] X. Z. Yu, N. Kanazawa, W. Z. Zhang, T. Nagai, T. Hara, K. Kimoto, Y. Matsui, Y. Onose, and Y. Tokura. Skyrmion flow near room temperature in an ultralow current density. *Nature Communications*, 3:988, August 2012.

[109] Stefan Heinze, Kirsten von Bergmann, Matthias Menzel, Jens Brede, André Kubetzka, Roland Wiesendanger, Gustav Bihlmayer, and Stefan Blügel. Spontaneous atomic-scale magnetic skyrmion lattice in two dimensions. *Nature Physics*, 7(9):713–718, September 2011.

[110] F. Jonietz, S. Mühlbauer, C. Pfleiderer, A. Neubauer, W. Münzer, A. Bauer, T. Adams, R. Georgii, P. Böni, R. A. Duine, K. Everschor, M. Garst, and A. Rosch. Spin transfer torques in MnSi at ultralow current densities. *Science*, 330(6011):1648–1651, December 2010. PMID: 21164010.

[111] J. Sampaio, V. Cros, S. Rohart, A. Thiaville, and A. Fert. Nucleation, stability and current-induced motion of isolated magnetic skyrmions in nanostructures. *Nature Nanotechnology*, 8:839, October 2013.

[112] Niklas Romming, Christian Hanneken, Matthias Menzel, Jessica E. Bickel, Boris Wolter, Kirsten von Bergmann, André Kubetzka, and Roland Wiesendanger. Writing and Deleting Single Magnetic Skyrmions. *Science*, 341(6146):636–639, August 2013.

[113] Youngbin Tchoe and Jung Hoon Han. Skyrmion generation by current. *Physical Review B*, 85(17):174416, May 2012.

[114] M. Finazzi, M. Savoini, A. R. Khorsand, A. Tsukamoto, A. Itoh, L. Duò, A. Kirilyuk, Th. Rasing, and M. Ezawa. Laser-induced magnetic nanostructures with tunable topological properties. *Physical Review Letters*, 110(17):177205, April 2013.

[115] R Rajaraman. *Solitons and Instantons*. North-Holland, Amsterdam, 1987.

[116] B. Berg and M. Lüscher. Definition and statistical distributions of a topological number in the lattice o(3) σ-model. *Nuclear Physics B*, 190(2):412–424, August 1981.

[117] J.C. Slonczewski. Current-driven excitation of magnetic multilayers. *Journal of Magnetism and Magnetic Materials*, 159(1–2):L1–L7, June 1996.

[118] Behtash Behin-Aein, Deepanjan Datta, Sayeef Salahuddin, and Supriyo Datta. Proposal for an all-spin logic device with built-in memory. *Nat Nano*, 5(4):266–270, April 2010.

[119] Arne Brataas, Andrew D. Kent, and Hideo Ohno. Current-induced torques in magnetic materials. *Nat Mater*, 11(5):372–381, May 2012.

[120] José Luis García-Palacios and Francisco J. Lázaro. Langevin-dynamics study of the dynamical properties of small magnetic particles. *Physical Review B*, 58(22):14937–14958, December 1998.

[121] David M Pozar. *Microwave engineering*. Wiley, Hoboken, NJ, 2012.

[122] F. Wenger, T. Gustafsson, and L.J. Svensson. Perturbation theory for inhomogeneous transmission lines. *IEEE Trans. Circuits Syst. I, Fundam. Theory and Appl.*, 49(3):289–297, March 2002.

[123] J. A. Brandao Faria. *Multiconductor Transmission-Line Structures: Modal Analysis Techniques*. John Wiley & Sons, 1993.

[124] Jianmin Zhang, J.L. Drewniak, D.J. Pommerenke, M.Y. Koledintseva, R.E. DuBroff, W. Cheng, Zhiping Yang, Q.B. Chen, and A. Orlandi. Causal RLGC(f) models for transmission lines from measured -parameters. *IEEE Trans. Electromagn. Compat.*, 52(1):189–198, 2010.

[125] D.A. Frickey. Conversions between s, z, y, h, ABCD, and t parameters which are valid for complex source and load impedances. *IEEE Trans. Microw. Theory Techn.*, 42(2):205–211, 1994.

[126] Roger B. Marks and Dylan F. Williams. Comments on "conversions between s, z, y, h, abcd and t parameters which are valid for complex source and load impedances". *IEEE Trans. Microw. Theory Techn.*, 43(4):914–915, April 1995.

[127] John C. Tippet and Ross A. Speciale. A rigorous technique for measuring the scattering matrix of a multiport device with a 2-port network analyzer. *IEEE Trans. Microw. Theory Techn.*, 30(5):661–666, May 1982.

[128] E. Van Lil. Comments on "a rigorous technique for measuring the scattering matrix of a multiport device with a two-port network analyzer". *IEEE Trans. Microw. Theory Techn.*, 33(3):286–287, March 1985.

[129] Jose A. Brandao Faria. A new modal analysis theory for multiconductor nonuniform transmission-line structures: Application to the analysis of line junctions". *IEEE Trans. Power Syst.*, 19(3):1380–1386, AUGUST 2004.

[130] J. Frei, Xiao-Ding Cai, and S. Muller. Multiport s-parameter and t-parameter conversion with symmetry extension. *IEEE Trans. Microw. Theory Techn.*, 56(11):2493–2504, 2008.

[131] Allan Huynh, Magnus Karlsson, and Shaofang Gong. Mixed-mode s-parameters and conversion techniques. In Vitaliy Zhurbenko, editor, *Advanced Microwave Circuits and Systems*. InTech, April 2010.

[132] V.K. Tripathi. Asymmetric coupled transmission lines in an inhomogeneous medium. *IEEE Trans. Microw. Theory Techn.*, 23(9):734–739, 1975.

[133] Xiao-Ding Cai and Robert J. Drost. Method and apparatus for representing high speed interconnects in closed forms, October 2011.

[134] K. C. Gupta, Ramesh Garg, and Rakesh Chadha. *Computer-Aided Design of Microwave Circuits*. Artech, 1981.

[135] Howard W Johnson and Martin Graham. *High-speed signal propagation: advanced black magic*. Prentice Hall/PTR, Upper Saddle River, NJ, 2003.

[136] Anthony J. Bur. Dielectric properties of polymers at microwave frequencies: a review. *Polymer*, 26(7):963–977, July 1985.

[137] Glenn F. Engen and Cletus A. Hoer. Thru-reflect-line: An improved technique for calibrating the dual six-port automatic network analyzer. *IEEE Trans. Microw. Theory Techn.*, 27(12):987–993, 1979.

[138] Lin Li, Ke Wu, and Peter Russer. On the thru-reflect-line (TRL) numerical calibration and error analysis for parameter extraction of circuit model. *Int. J. RF Microw. C. E.*, 16(5):470–482, 2006.

[139] C. Seguinot, P. Kennis, J.-F. Legier, F. Huret, E. Paleczny, and L. Hayden. Multimode TRL. a new concept in microwave measurements: theory and experimental verification. 46(5):536–542, 1998.

[140] Roger B. Marks. A multiline method of network analyzer calibration. *IEEE Trans. Microw. Theory Techn.*, 39(7):1205–1215, 1991.

[141] A.P. Duffy, A.J.M. Martin, A. Orlandi, G. Antonini, T.M. Benson, and Malcolm S. Woolfson. Feature selective validation (FSV) for validation of computational electromagnetics (CEM). part i-the FSV method. *IEEE Transactions on Electromagnetic Compatibility*, 48(3):449–459, August 2006.

[142] A. Orlandi, A.P. Duffy, B. Archambeault, G. Antonini, D.E. Coleby, and S. Connor. Feature selective validation (FSV) for validation of computational electromagnetics (CEM). part II- assessment of FSV performance. *IEEE Transactions on Electromagnetic Compatibility*, 48(3):460–467, August 2006.